EFFECT OF PRE-SINTERING PROCESSES AND ADDITIONS ON DENSIFICATION IN LLZO SOLID ELECTROLYTES

Furkan GÜLBEYAZ

Master's Thesis

Department of Advanced Technologies

Programme in Nanotechnology

Supervisor: Prof. Dr. Servet TURAN

Eskişehir

Eskişehir Technical University

Institute of Graduate Programs

December 2021

ABSTRACT

EFFECT OF PRE-SİNTERİNG PROCESSES AND ADDİTİONS ON DENSİFİCATİON İN LLZO SOLİD ELECTROLYTES

Furkan GÜLBEYAZ

Department of Advanced Technologies

Programme in Nanotechnology

Eskişehir Technical University, Institute of Graduate Programs, December 2021

Supervisor: Prof. Dr. Servet TURAN

In this thesis, it is aimed to increase the density of the solid electrolyte material $Li_7La_3Zr_2O_{12}$ (LLZO), which has a high potential for use in solid state batteries, and to increase its ionic conductivity depending on the density increase. In this context, it was tried to get LLZO solid electrolyte with a dense microstructure by examining the effects of pre-sintering processes and additions on densification in LLZO solid electrolytes. LLZO solid electrolyte materials were produced by conventional solid-state reaction, which offers advantages such as simple preparation process, high yield and low cost. Microstructure investigations were carried out with scanning electron microscope in SE (Seconder electron) and BSE (Back scatter electron) modes. Phase analyzes were performed by XRD method. The ionic conductivity values were measured by the electrochemical impedance spectrum method and were calculated considering the geometrical factors. In this study, it was determined that the sample with suitable grain growth, dense structure and high ionic conductivity was the T-LLZO sample, which was calcined in powder form, sintered at 1100 ºC, powder bed was used during sintering and 10% RMD-LLZO added (5.6×10^{-4} S/cm).

Keywords: Energy Storage, Solid Electrolyte, Li7La3Zr2O12 (LLZO), Densification, Ionic Conductivity

ÖZET

LLZO KATI ELEKTROLITLERDE SINTERLEME ÖNCESI İŞLEMLERIN VE İLAVELERIN YOĞUNLAŞMAYA ETKISI

Furkan GÜLBEYAZ

İleri Teknolojiler Anabilim Dalı

Nanoteknoloji Bilim Dalı

Eskişehir Teknik Üniversitesi, Lisansüstü Eğitim Enstitüsü, Aralık 2021

Danışman: Prof. Dr. Servet TURAN

Bu tez çalışmasında, katıhal pillerinde yüksek kullanım potansiyeline sahip $Li_7La_3Zr_2O_{12}$ (LLZO) katı elektrolit malzemesinin yoğunluğunun ve yoğunluk artışına bağlı olarak iyonik iletkenliğinin arttırılması amaçlanmıştır. Bu bağlamda, LLZO katı elektrolitlerde sinterlemeden önceki işlemlerin ve ilavelerin yoğunlaşmaya etkisi incelenerek yoğun bir mikro yapıya sahip LLZO katı elektroliti elde edilmeye çalışılmıştır. LLZO katı elektrolit malzemeleri, basit hazırlama süreci, yüksek verim ve düşük maliyet gibi avantajlar sunan geleneksel katı hal reaksiyonu ile üretilmiştir. Mikroyapı incelemeleri taramalı elektron mikroskobuyla SE (Seconder elektron) ve BSE (Back scatter elektron) modlarında yapılmıştır. Faz analizleri XRD yöntemiyle yapılmıştır. İyonik iletkenlik değerleri elektrokimyasal empedans spektrumu yöntemiyle ölçülmüştür ve geometrik faktörler göz önüne alınarak hesaplanmıştır. Bu çalışmada, uygun tane büyümesinin görüldüğü ve yoğun bir yapıya sahip aynı zamanda da yüksek iyonik iletkenliğe sahip olan numunenin, toz formunda kalsine edilen, 1100 ºC'de sinterlenen, sinterleme sırasında toz yatağı kullanılan ve %10 RMD-LLZO katkılı T-LLZO numunesi olduğu tespit edilmiştir ($5{,}6 \times 10^{-4}$ S/cm).

Anahtar Sözcükler: Enerji Depolama, Katı Elektrolit, Li7La3Zr2O12 (LLZO), Uoğunlaşma, İyonik İletkenlik

ACKNOWLEDGEMENTS

First of all, I would like to thank Prof.Dr.Servet TURAN for agreeing to be my advisor during my thesis work.

I would like to thank Ahmet Furkan BULUC for his support, who guided me with his knowledge and experience, spared his time, contributed to every step of my work and helped me tirelessly.

I would like to thank Dr.Kamil Burak DERMENCI for sharing his ideas and opinions, conveying all his knowledge and always taking time to help.

Finally, I would like to thank the personnel of the Department of Materials Science and Engineering of Eskişehir Technical University, who provided technical support to ensure that my experiments were carried out smoothly.

Furkan GÜLBEYAZ

29/12/2021

STATEMENT OF COMPLIANCE WITH ETHICAL PRINCIPLES AND RULES

I hereby truthfully declare that this thesis is an original work prepared by me; that I have behaved in accordance with the scientific ethical principles and rules throughout the stages of preparation, data collection, analysis and presentation of my work; that I have cited the sources of all the data and information that could be obtained within the scope of this study, and included these sources in the references section; and that this study has been scanned for plagiarism with "scientific plagiarism detection program" used by Eskişehir Technical University, and that "it does not have any plagiarism" whatsoever. I also declare that, if a case contrary to my declaration is detected in my work at any time, I hereby express my consent to all the ethical and legal consequences that are involved.

Furkan GÜLBEYAZ

CONTENTS

Page

LIST OF TABLES

Page

LIST OF FIGURES

Page

GLOSSARY OF SYMBOLS AND ABBREVIATIONS

Å	:	Angstrom
AC	:	Alternative Current
α	:	Alpha
β	:	Beta
BSE	:	Back Scatter Electron
DC	:	Direct Current
E_a	:	Activation Energy
eV	:	Electron-Volt
EV	:	Electrical Vehicle
kW	:	Kilowatt
LLZO	:	$Li_7La_3Zr_2O_{12}$
SE	:	Seconder Electron
SEI	:	Solid-Electrolyte Interphase
SEM	:	Scannig Electron Microscopy
S/cm	:	Siemens/centimeter
T	:	Temperature
V	:	Volt
XRD	:	X- Ray Diffraction
$mAh.g^{-1}$	:	Miliamper hour/gram
NASICON	:	Na Super Ionic Conductor
2D	:	Two Dimensions
RMD- LLZO	:	Red Mud Doped $Li_7La_3Zr_2O_{12}$
T-LLZO	:	Tetragonal $Li_7La_3Zr_2O_{12}$
LLTO	:	$Li_{0.34}La_{0.51}TiO_{2.94}$

1. INTRODUCTION

The increasing energy demand since the industrial revolution is largely met by fossil fuels. Fossil fuels are composed of organic remains of plants and animals over the years and contain high levels of carbon and hydrocarbons. Fossil fuels, which meet this increasing energy need due to population growth and changing needs, are rapidly depleted and at the same time cause serious damage to the environment. The increase in the amount of gases such as CO_x, SO_x and NO_x, which are the combustion products of fossil fuels, in the atmosphere causes the greenhouse effect, acid rain and damage to the ozone layer. Until a massive movement for renewable energy instead of fossil fuels is successful, the effects of damage caused by fossil fuels will continue. Solar and wind energy, which are among the renewable energy sources, are accepted as one of the most effective and efficient solutions for the depletion of resources and environmental pollution that we encounter during the use of fossil fuels. However, solar and wind energy is intermittent and variable as it depends on weather conditions. Battery energy storage systems can be used to get rid of the effects of weather conditions. When the weather conditions are suitable, the stored energy can be used when the weather conditions are not suitable. Battery energy storage systems are also promising in terms of portable devices due to the increase in people's mobility.

In addition to meeting the needs of industry, heating and lighting, the energy needs of cars with internal combustion engines, which we use as transportation vehicles, are also provided by fossil fuels. However, due to the exhaustion of fossil fuels and the damage they cause to the environment, interest in hybrid electric vehicles (EV) and electric vehicle technologies has increased today.

Today, lithium-ion batteries can be preferred in many areas where high energy density is needed. Batteries are electrochemical energy storage systems that store electrical energy as chemical energy during charging and convert this chemical energy into electrical energy during discharge. In these systems, there is a liquid electrolyte that provides the transmission of ions from the anode to the cathode during discharge. With the use of electrical energy during charging, lithium ions are moved in the opposite direction and transmitted to the anode. Liquid electrolytes prepared by dissolving some salts in organic solvents can cause dangerous situations such as flammability, corrosion, evaporation and leakage. Solid electrolytes have been developed as a solution to these

problems that may occur. In batteries using solid electrolyte, direct contact of the anode and cathode electrodes is prevented, and negative situations such as flammability or explosion, which are seen in batteries using liquid electrolyte, are not observed. Batteries produced using solid electrolyte are considered to be safer and longer lasting than batteries produced using liquid electrolyte.

The use of solid-state lithium batteries as a power source for electric vehicles, which are on the rise with the abandonment of fossil fuels, promises a great future, so solid electrolyte systems are an important research topic in battery technology studies today. The development of various solid electrolytes for solid-state lithium batteries has become the focus of many researchers. However, although solid electrolytes are safe and long-lasting, early studies have shown that they have lower ionic conductivity than liquid electrolytes (10^{-7}- 10^{-6} S/cm). The low ionic conductivity of solid electrolytes prevents their use in portable devices and vehicles. Today, thanks to various doping and production techniques, solid electrolytes with an ionic conductivity value of 10^{-4}- 10^{-3} S/cm can be obtained, which can compete with liquid electrolytes.

In this study, garnet type LLZO solid electrolyte with high ionic conductivity and dense microstructure was tried to be produced. Different methods have been used to produce the solid electrolyte with the desired properties. In the study, the effect of multielement doping, the effect of grinding time, the effect of precalcination processes and the effect of one-step densification process were investigated.

This study includes 6 chapters. In the 1st chapter, energy storage systems and their properties, in the 2nd chapter, comprehensive information about lithium-ion batteries and their components, in the 3rd chapter the purpose of the thesis, in the 4th chapter, the experimental techniques used during the experiments and the experimental processes applied to characterize the solid electrolytes, in the 5th chapter, the findings obtained in the thesis study are given in detail. Finally, conclusions and recommendations are given in 6th Chapter.

1. ENERGY STORAGE SYSTEMS

The history of human civilization is the history of discovering energy and mineral resources. Mankind has existed to the extent that it has transformed its environment and nature. He progressed by taking advantage of the muscle power of the living creatures around him and then natural resources such as water and wind, and after realizing the power of fuels, he carried his civilization to today. Our civilization has been shaped by our ability to control and access energy resources. We obtain and use energy widely as heat and electricity. Regardless of its type, energy headings for human beings are gathered in four main topics. These are;

- Produce
- Transmit
- Distribute
- Storage

The first three titles contain the necessary steps to produce the energy and deliver it to the user. The last one, storage, provides us with the opportunity to use it in a sustainable and efficient way. Energy, defined as the ability to do useful work, is the most fundamental and vital phenomenon that activates the welfare and security of human civilization. The future of sustainable societies depends on the ability to use and store energy [1].

1.1. Importance of Energy Storage

In our world, the energy need that arises from the continuous increase in population and the increase in industrialization cannot be met due to regionally limited resources, and the gap between energy production and consumption is rapidly widening. This situation causes us to follow policies to utilize existing energy resources more effectively and to conserve energy resources. To meet the need for the rapid increase in energy demand, the efficient storage of the energy we obtain from renewable energy sources is required.

Today, the big portion of the world's need for energy is provided by fossil fuels, and besides, the energy need is increasing day by day, which causes the limited reserves of fossil fuels in the world to decrease regularly. In addition to the production/consumption balance, the consumption of fossil fuels increases greenhouse

gas emissions and causes important problems such as global warming that would deeply affect the whole world. The storage of secondary forms of energy such as heat and electricity helps to reduce the amount of primary energy forms (fossil fuels) consumed to produce them. That does not only reduce emissions of CO_2 and greenhouse gases that cause global warming, but also helps to conserve fossil fuels that are believed to be exhaustible [4]. First of all, alternative and renewable energy systems, especially systems based on solar and wind, are important for the future of humans. However, these alternative energy sources depend on natural conditions. These resources vary greatly regionally and may even change seasonally, daily and abruptly. This situation can lead to problems by causing differences between the produced energy and the demand for the energy. Therefore, energy storage units are of great importance in order to meet this need when energy is needed. Excess energy produced from alternative sources is transferred to energy storage units, and the stored energy is used to meet the need when there is no or insufficient access to the main sources [2,3].

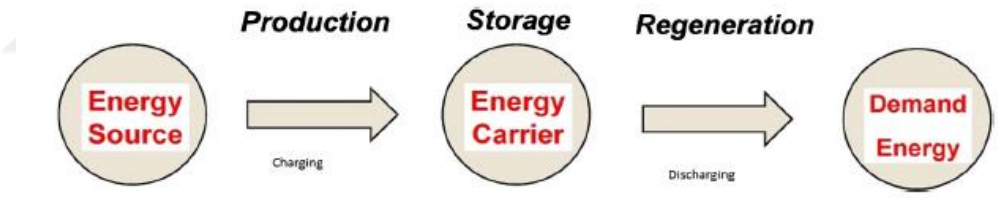

Figure 1.1. *Energy Storage Concept [3]*

1.2. Purpose of Energy Storage

Energy storage aims to eliminate the possible difference between the supply and demand of the needed energy. It plays an important role in the storage and use of energy obtained from alternative energy sources, and in the elimination of the damage caused by fossil fuels used for energy production [2,3].

1.3. Energy Storage Techniques

Storing energy to use it at any time is called storage. Various energy storage methods have been developed because it is desired to have energy ready for use when and where it is needed. Essential properties in an energy storage system are high storage

capacity, high charge/discharge efficiency, low capacity losses, cheapness, long life, ability to store energy in minimum volume and weight. Today, there are various energy storage methods, which are mechanical, thermal, electrochemical and electrical energy storage [3].

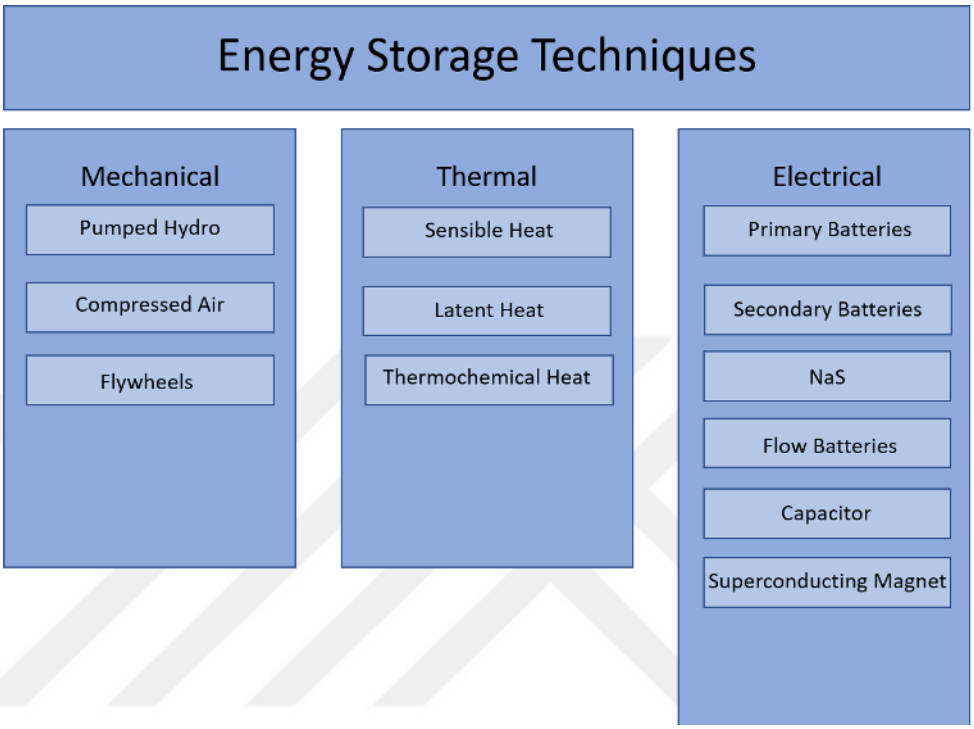

Figure 1.2. *Energy Storage Techniques*

1.3.1. Mechanical energy storage

There are basically two systems to store the energy generated by applying force to a system. These are related with the change in potential energy and the kinetic energy generated by the movement of mass. These types of energy can both be converted to each other and converted to work in different ways [5].

1.3.1.1. Flywheels

When it was first applied, it stored mechanical energy and gave it back as kinetic energy when needed, but with today's technology, its usage areas have been increasing thanks to the applications in which electrical-mechanical conversions are made. [2]. It stores electrical energy in the form of rotational kinetic energy [6]. Flywheel energy accumulators consist of a motor generator and composite flywheel combined with brackets and they have a low pressure casing that helps to reduce self-discharge losses.

The flywheel operates in charge and discharge mode. In the energy storage mode, also known as the charging stage, electrical energy is used to accelerate the motor, which is connected to the rotor via a shaft. The rotation of the shaft transfers an angular momentum to the rotor. Rotary rotates in the discharge phase using the generator connected to the same shaft, and it transfers the kinetic energy back to electrical energy while decelerating. While the device acts as a motor during the charging phase, it acts as a generator during the discharge phase [3].

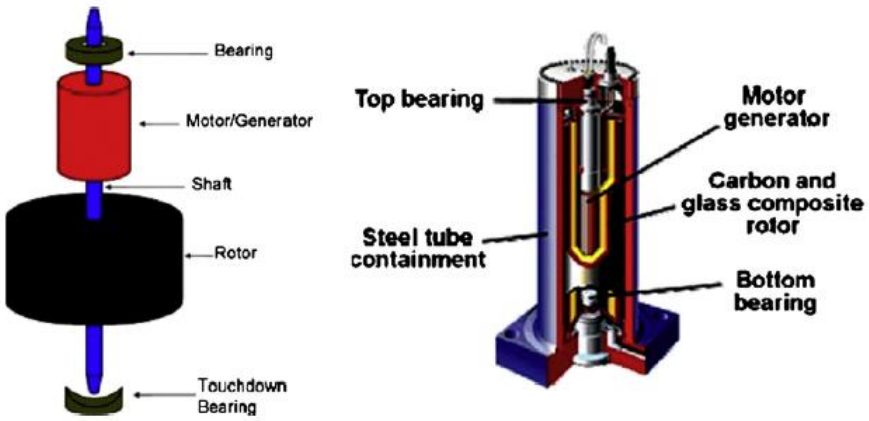

Figure 1.3. *Flywheels [3].*

1.3.1.2. Pumped hydroelectric energy storage

One of the oldest and most mature storage technologies, pumped hydroelectric energy storage technology uses gravity to store energy [3]. In these type of systems, there are two water reservoirs located vertically. Here, energy is stored by extracting it from the low reservoir to the high reservoir and then withdrawing energy from the low reservoir depending on the need. The stored energy transforms into potential energy, which is one of the important principles of physics. Although these systems are referred as mechanical storage technology, they are mostly used to generate electricity.

When electricity is not used, water is pumped from a low level to a high level to store energy, and electricity can be produced again when needed [4].

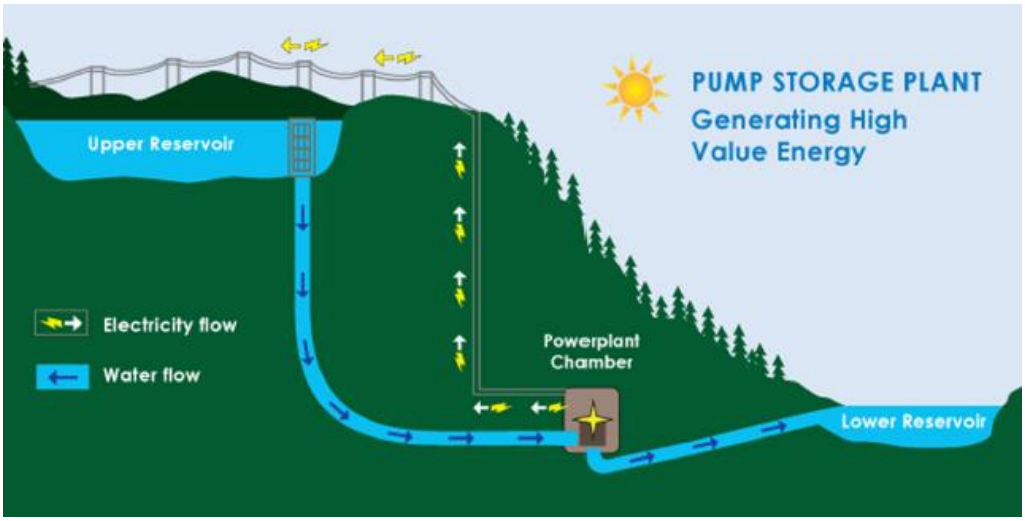

Figure 1.4. *Pumped hydroelectric energy storage [3].*

1.3.1.3. Compressed air energy storage

In these systems, when intensive use of energy is not required, energy is stored in an air storage tank with the help of a compressor. In compressed air systems, electrical energy is used to move the compressors, which transmit the air to the containers under high pressure and then the compressed air in the piston or turbine in the case of need for energy [7]. Commercially, it comes after pumped hydroelectric energy storage. Underground caves or salt caves are used as reservoirs [3].

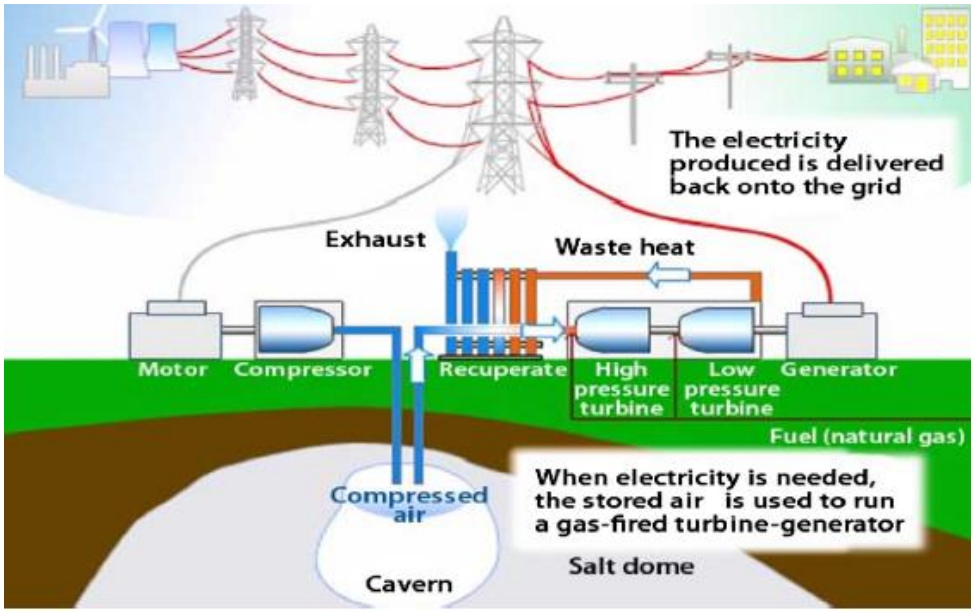

Figure 1.5. *Process diagram of Compressed Air Energy Storage [3].*

1.3.2. Thermal energy storage

The energy transmitted to increase the temperature of a substance, which is the energy exchanged and transferred between substances with different temperatures, is called heat energy. This type of energy consists of all of the kinetic and potential energies of the atoms or molecules that make up a substance. It is formed as a result of vibrations at the atomic or molecular level [8]. Thermal energy storage is one of the most commonly used methods. Thermal energy storage systems consist of devices used to store electricity or other heat sources in the form of thermal energy [10].

Heat energy storage applications are divided into two groups depending on the usage time of them. These are short-term and long-term storage methods. According to the determined targets, the heat can be stored for a short time, which is as day and night, or the heat stored for a long time in the summer can be used in the winter and the heat stored in the winter can be used in summer. Thermal energy storage method significantly helps to increase energy efficiency by saving industry, agriculture, electrical energy and fossil fuels. Heat source systems such as waste heat from power plants, solar energy and geothermal energy could be the sources needed for thermal storage [2].

Heat energy is stored as the change in the internal energy of the substance, the latent, heat of reaction, or the sum of all these. In the application of sensible heat storage, the sensible heat resulting from the change in the temperature of the storage material is utilized [9]. In latent heat storage, the use of the materials that show phase change helps to determine the latent heat that emerges as a result of the phase change of the storage material at a suitable temperature for storage. In thermochemical heat storage application, heat energy can be stored as bond energy in compounds and the same energy can be released by reversible reactions [8].

1.3.2.1. Sensible heat storage

In these energy storage systems, the used storage material does not show any phase change in the temperature range that is required for the storage application. The materials most commonly used in high temperature thermal energy storage application are molten salts, concrete and cast ceramics. Molten salts are used in solar energy applications [3].

1.3.2.2. Latent heat storage

In the latent heat storage method, there is stored the latent heat generated as a result of the phase change of the materials in the storage environment. The materials used in this method are known as phase change materials. They are divided as organic and inorganic. The best example of organic phase change materials is paraffin [11]. Inorganic phase change materials are salts, salt hydrates, metals and their alloys. Examples: sodium sulfate decahydrate, sodium thiosulfate, calcium chloride hexahydrate [3].

1.3.2.3. Thermochemical heat storage

This energy storage method consists of a reversible reaction in which heat is stored during the endothermic reaction and released during the exothermic reaction. During charging, thermal energy is used to separate a chemical reactant into products by an endothermic reaction, and the products are stored separately depending on the energy requirement. During discharge, the separately stored products are mixed together and react to form the reactant in an exothermic reaction, and the heat generated during this reaction is stored and used as an energy source. The materials used in this method have been investigated for a long time due to their high efficiency. Some of the currently researched thermochemical heat storage materials are: MgH_2, $PbCO_3$, $Mg(OH)_2$, BaO_2, NH_4HSO_4 [11].

The energy density obtained by this method is 5-10 times higher than the energy density obtained in sensible and latent heat storage. In this storage method, since the products can be stored at ambient temperature, no heat loss occurs during the storage phase and storage periods are unlimited since there is no heat loss [3].

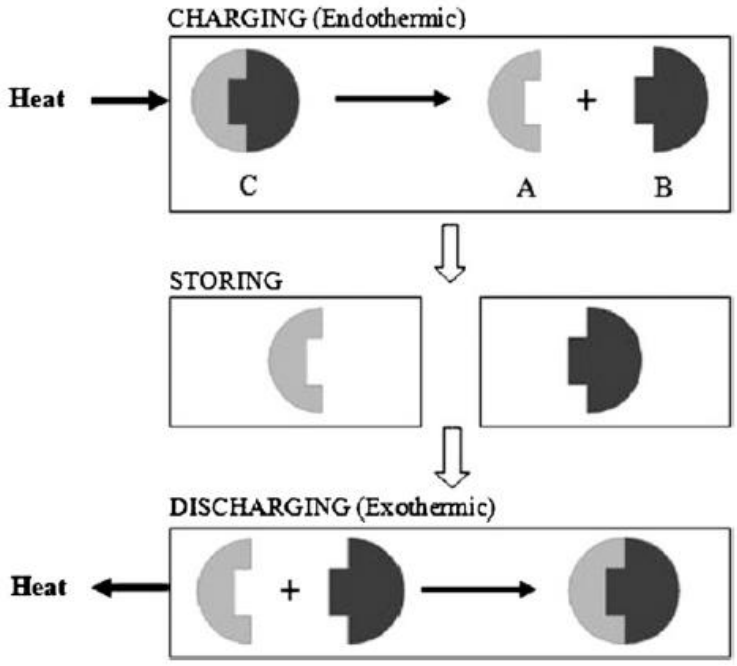

Figure 1.6. *Process of thermochemical heat storage [3].*

1.3.3. Electrical energy storage

1.3.3.1. Lead acid (PbO_2) battery

These batteries have old technology. When we examine these batteries; they contain a lead plate and a lead dioxide plate, which are the anode and the cathode. Diluted sulfuric acid provides sulfate ions for discharge.

These batteries are generally used as batteries in vehicles to give the engine the first movement and to meet the electricity need when the vehicle is stationary [12]. It is also used in motorcycles, boats, base stations, uninterruptible power supplies and for lighting purposes. Their advantages are high performance at low and high temperatures, easy maintenance and low cost. The disadvantages are short lifetime, self-discharge and poor storage during discharge [2].

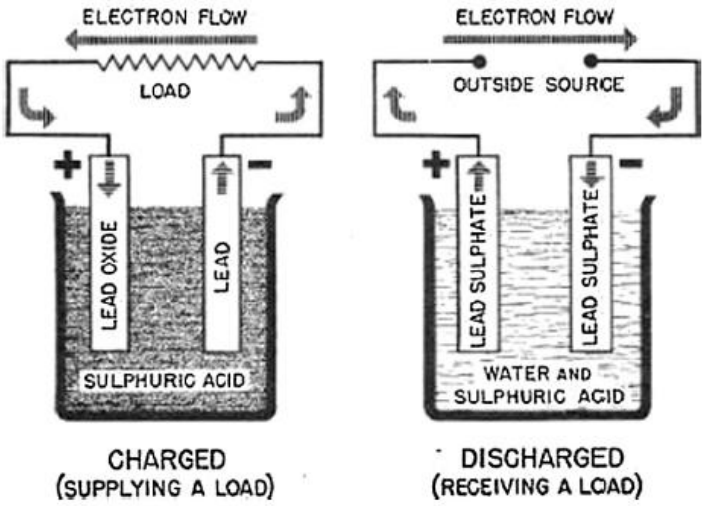

Figure 1.7. *Schmetatic represantive of Lead Acid Battery System [3].*

1.3.3.2. Nickel cadmium battery

These batteries are not widely used. They contain cadmium metal at the anode and $Ni(OH)_2$ at the cathode. These batteries are used in applications where long service life and high current are required. They are known for their long cycle life, fast charging and deep charging rates without loss of capacity. They can achieve 3000 cycles [13]. Nickel cadmium batteries can safely supply very high currents, but if they are used continuously and are not fully discharged and charged, they must be fully discharged at certain intervals. Ottherwise, crystallization occurs in the plates in the cells and this is called memory effect. Due to the memory effect, the efficiency of the battery decreases over time. It is used in aviation, emergency lighting and telecommunication systems [2].

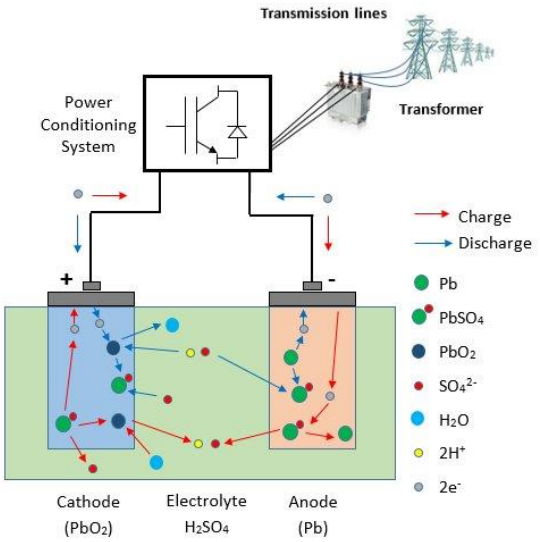

Figure 1.8. *Schematic diagram of Ni-Cd battery energy storage system [14].*

1.3.3.3. Nickel metal hydride battery

In these batteries, metal hydride, which has hydrogen absorption feature, is used as the anode and $Ni(OH)_2$ is used as the cathode. The most important feature of these batteries is their high energy density and their environmentally friendly composition and metals. They have the advantages to achieve higher energy density than nickel cadmium batteries, to be less prone to memory effects than nickel cadmium batteries, require fewer periodic charge-discharge cycles and to be easily recyclable [2].

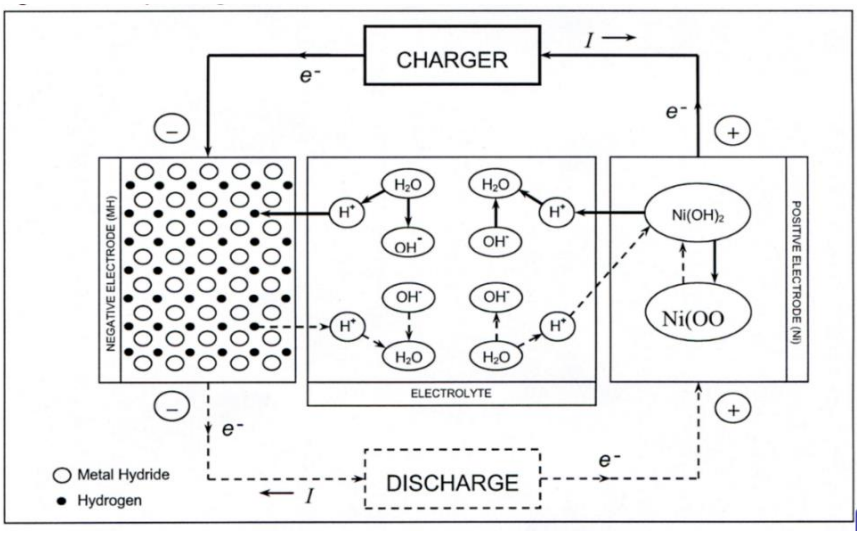

Figure 1.9. *Transport diagram of Nickel metal hydride battery [15]*

1.3.3.4. Flow battery

Flow batteries, commonly known as redox flow batteries, are a new technology. In these batteries, the battery is charged and discharged by a chemical reaction between two liquid electrolytes. Unlike other conventional batteries, liquid electrolytes are stored in separate tanks in flow batteries. During operation, these electrolytes are pumped into the electrochemical reactor, where electricity is produced and a chemical redox reaction takes place. Since electrolytes are stored outside the reactor, the power and energy content of the system can be specified separately. Unlike other batteries, it is very easy to replace or increase the amount of electrolyte. Flow batteries are distinguished from fuel cells in which the chemical reactions involved are reversible. Flow batteries can continuously release energy at a high discharge rate lasting up to 10 hours [11].

One of the biggest advantages of these batteries is that they are easily scalable since their energy capacity dependens on the amount of the stored electrolyte. Another great advantage is that since electrolytes are stored in separate tanks, they can be discharged completely without any damage and the risk of self-discharge is very low. Because of these features, flow batteries are known as low-maintenance and long-lasting systems [16]. In the past years, three types of flow batteries have come to the stage of commercialization [17]. These types are; Vanadium Redox Battery (VRB), Polysulphide Bromide Batteries (PSB), Iron Zinc bromine (ZnBr). The operation of VRB batteries is based on the redox reaction of different ionic forms of vanadium. ZnBr type batteries consist of two electrode surfaces separated by a microporous film and two electrolyte flow currents. The electrolytes used in these batteries are aqueous solutions of zinc bromine, and the positive electrolyte is called the catholyte and the negative electrolyte is called the anolyte [3].

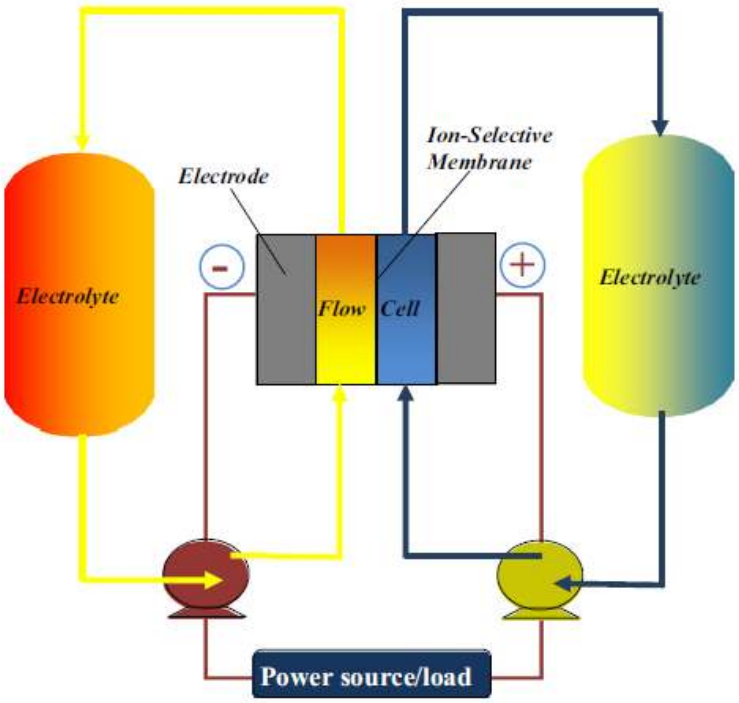

Figure 1.10. *Schematic representation of the redox flow cell energy storage system [16].*

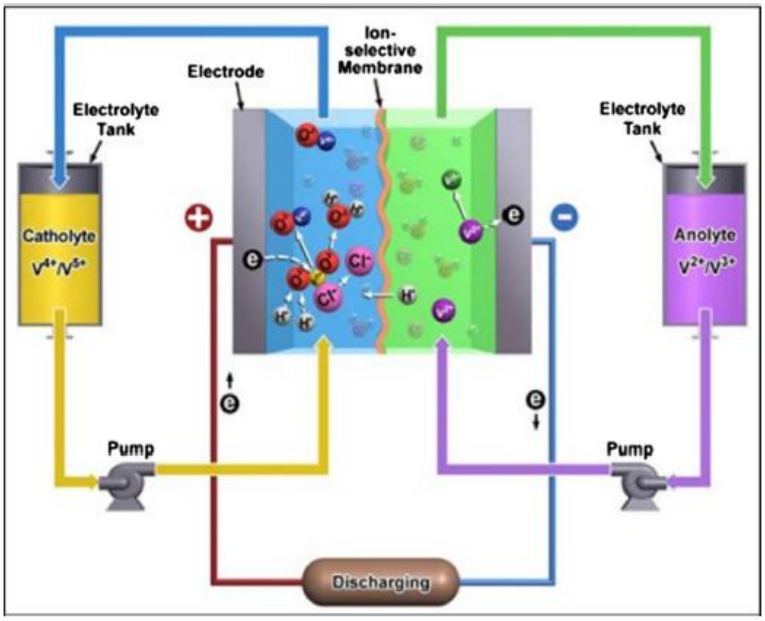

Figure 1.11. *Schematic representation of a vanadium redox battery [17].*

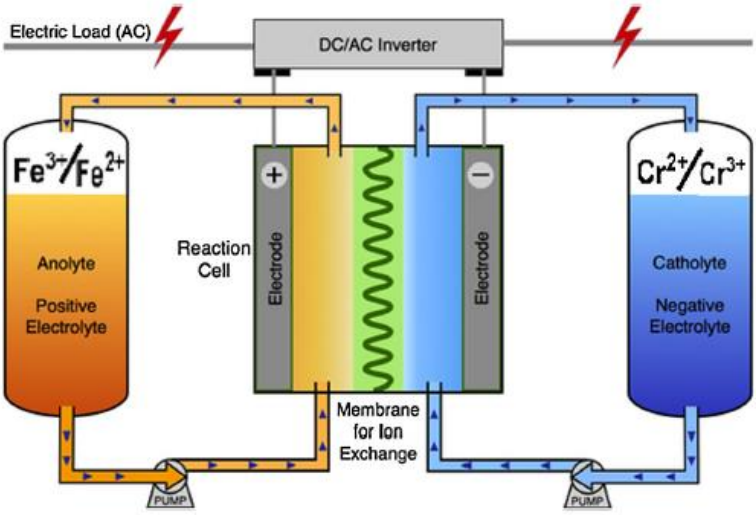

Figure 1.12. *Schematic representation of FeCr battery [2].*

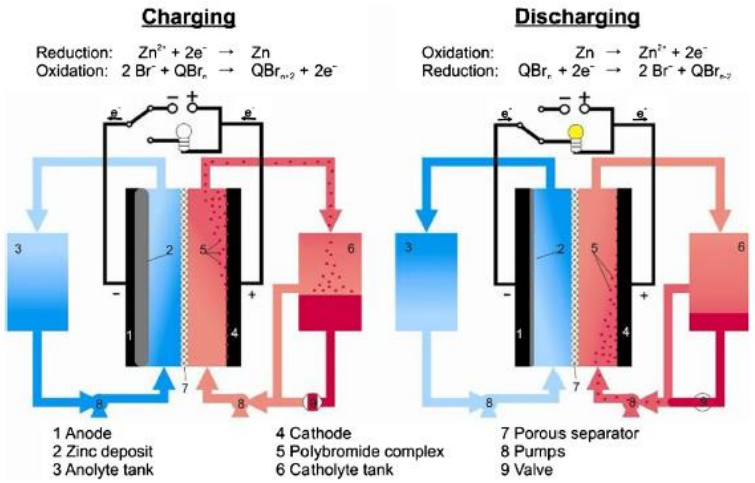

Figure 1.13. *Schematic representation of ZnBr battery [2].*

Table 1.1. *Comparison between different technologies of flow battery [11].*

Technology	VRB	PSB	ZnBr
Efficiency (%)	85	75	75
Cycle life charge/discharge	13,000(12,000þ)	-	2500(2000þ)
Capacity (MW)	0.5–100()	1–15	0.05–1 (0.05–2)
Operation temp. (°C)	0–40 ()	50()	50()
Energy density (Wh/kg)	30(10–30)	-	50 (20–50)
Self-discharge	Small	Small	Small

1.3.3.5. Sodium-sulfur battery (NaS)

NaS batteries, consisting of liquid sulfur in the positive electrode and liquid sodium in the negative electrode, are used commercially in wind energy integration, electricity distribution networks and high-value grid services. The electrodes are separated by a solid alumina ceramic electrolyte. It is an economical system with low maintenance cost. Its potential comes from high energy density (151–170 kW h/m^3), long cycle capacity (2500 cycles, 90% discharge depth), energy efficiency (>85%), long discharge period. Material of construction is affordable and also recyclable. The disadvantage of the NaS battery is the operational hazard due to the use of metallic sodium when exposed to water.

In the discharge phase, it oxidizes at the negative electrode, that is sodium alumina interface, to form Na^+, and these ions move in the electrolyte and combine with the reduced sulfur at the positive electrode to form Na_2S_5. This leads to a two-phase liquid mixture. After all the free sulfur is consumed, Na_2S_5 gradually transforms into single-phase Na_2S_{5-x}.

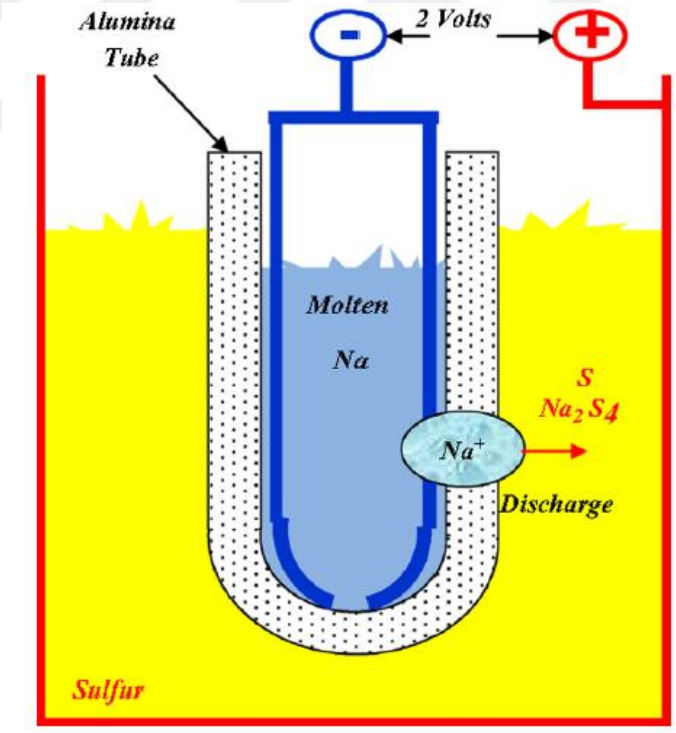

Figure 1.14. *NaS Battery [2].*

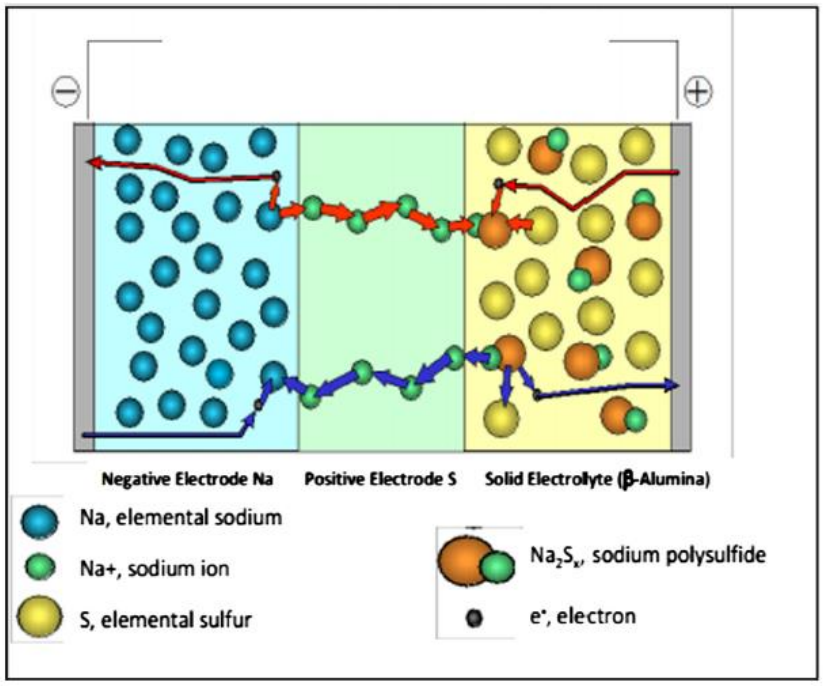

Figure 1.15. *NaS Operation [2].*

1.3.3.6. Superconducting magnetic energy storage

The superconducting magnetic energy storage (SMES) system uses a magnetic field to store energy that is cryogenically cooled at a temperature below the superconductor critical temperature without converting electrical energy into chemical or mechanical forms. In these systems, niobium titanium (NbTi) is used, which has almost zero resistance. SMES is obtained by inducing DC current into the coil made of NbTi filaments [18]. These systems consist of three parts. These are superconducting coil or magnet, cryogenically cooled refrigeration and power conditioning system [3]. The current increases during charging and decreases during discharge. For the application of AC and DC voltage, the current needs to be converted. Considering the overall system, a significant amount of energy is required to reach the cryogenic state, and although current must flow through non-superconducting materials causing losses, it is very efficient in commercial applications [11].

1.3.3.7. Capacitor and supercapacitor energy storage

Capacitors store energy as electrical charge between two metal plates separated by a dielectric material when a voltage difference is applied across the capacitor. The size of the plate, the distance between the plates and the dielectric material used determine the

capacitance [11]. Until recently, capacitors received less attention, but their long cycle life and immediate rechargeability were found to be a substitute for lithium-ion batteries in some applications [3]. Despite these characteristics of capacitors, they provide low energy density. A larger dielectric area is required to increase their energy density, making them uneconomical.

Supercapacitors, which use electrolyte solution instead of dielectric material, give higher capacitance, energy density and compactness compared to capacitors. Supercapacitors can store a large energy density and respond to power demand in milliseconds. The biggest problem faced by supercapacitors is reducing cost and increasing energy density to> 10 Wh/kg and thus moving them closer to batteries [19].

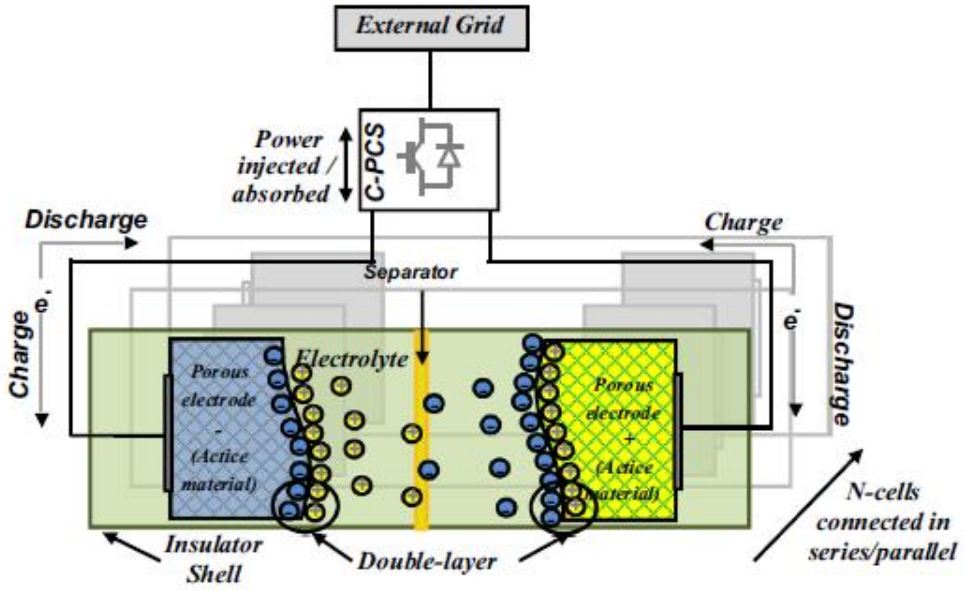

Fig. 8. The capacitor storage system.

Figure 1.16. *The Capacitor Storage system [11].*

1.3.3.8. Lithium-ion batteries

These batteries are used in almost all electronic devices we use today. Lithium-ion batteries are widely used due to their low internal resistance, high energy storage capacity and high efficiency. Their efficiency depends on their operation with attention to temperature and maximum capacity. Due to their high energy density and efficiency, these batteries are suitable for use in distribution systems and automotive fields.

While the battery is charging, the lithium atoms in the cathode ionize and combine with electrons, and the carbons, which are stored between the carbon layers as lithium atoms, move through the electrolyte towards the anode. This process reverses during the discharge time.

Lithium batteries have several advantages. These are long cycle life, working in a wide temperature range, no maintenance, fast charging capacity, no memory effect, high energy density and long life. The disadvantages are circuit elements need to be protected, capacity loss due to overcharge, possible explosion risk, degradation at high temperatures, high installation cost and decreasing of their lifetimes. Since the subject of my thesis is on solid electrolytes used in lithium-ion batteries, we will focus on the subject of lithium-ion batteries.

2. LITHIUM ION BATTERIES

In the last century, researchers have experimented on battery systems by testing various electrodes and electrolytes. For many years, nickel cadmium was the only usable battery, from wireless communications to various portable devices. Lithium-ion and nickel metal hydride batteries have developed competitively since the early 1990s. Lithium-ion batteries are the most developing and promising batteries today. Since lithium-ion batteries have high energy storage capacity in small volume and low weight, they have completely taken over the market, especially in mobile applications. In addition, since the memory effect that occurs in some battery types is negligible in lithium-ion batteries, we have the advantage of being able to charge these batteries whenever we want [20]. Compared to other rechargeable battery systems such as nickel-cadmium, lead acid and nickel metal hydride; lithium-ion batteries provide higher volumetric and gravimetric energy than other batteries. The operating voltage of these batteries is 3.7 V, which is about 3 times more than other batteries such as nickel metal hydride and nickel cadmium [22].

Lithium, which is the smallest element with atomic diameter after hydrogen and helium, is in the 1A group of alkali metals and its atomic number is 3. Elements of group 1A show electron-donating and positive charging properties. In addition to these properties, Lithium is the most suitable element for batteries, as it has the largest electrochemical potential among all metal elements and has a high energy density per weight.

Lithium-ion batteries consist of one or more compartments called cells. Each cell consists of 4 parts. These are positive electrode (cathode), negative electrode (anode), electrolyte and separator. The positive electrode is made of metal oxides, eg; lithium cobalt oxide ($LiCoO_2$), lithium nickel oxide ($LiNiO_2$) or lithium iron phosphate ($LiFePO_4$), and the negative electrode can be made of carbon (graphite) or titanate ($Li_4Ti_5O_{12}$).

Since the use of metallic lithium in lithium batteries that were previously used in mobile phones caused gas compression and sudden explosions, graphite-like anode active materials began to be used instead of metallic lithium [20].

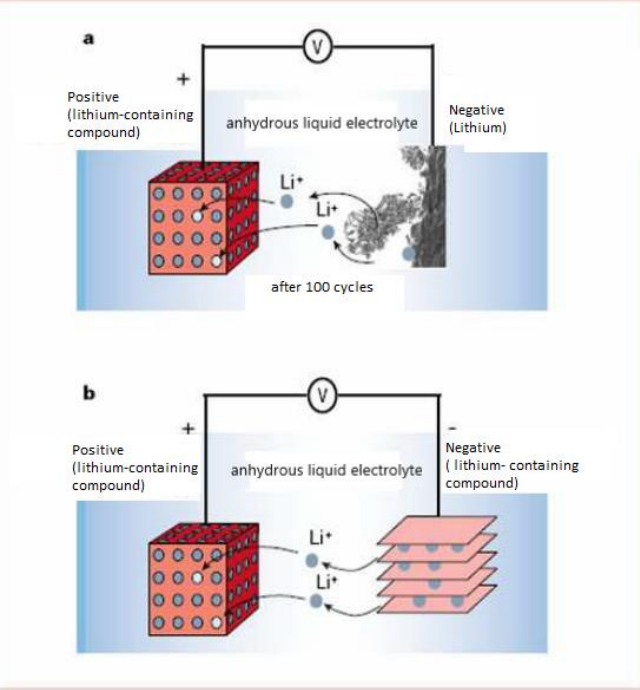

Figure 2.1. *Change in anode structure after 100 cycles of rechargeable batteries using (a) metallic lithium and (b) graphite or an inclusion compound as the anode [21].*

Liquid organic solutions, solid polymer electrolytes, polymer gel electrolytes, ceramic electrolytes or ionic liquids are used to provide ion movement in the electrolyte located between the two electrodes. A separator is used to separate the positive and negative electrodes from each other.

In lithium-ion batteries, lithium ions and electrons move from the cathode to the anode during charging and from the anode to the cathode during discharge. During this movement, electrons move in the external circuit and lithium ions move in the electrolyte. Lithium ions, which are located in the appropriate spaces of the crystal lattice of the cathode active substance during charging, move towards the anode after passing through the electrolyte, while the opposite occurs during discharge. During charging and discharging, an amount of current passes through the external circuit to meet the lithium ion transition. In the charging state, the anode is reduced by taking electrons, while the cathode is oxidized by losing electrons [23].

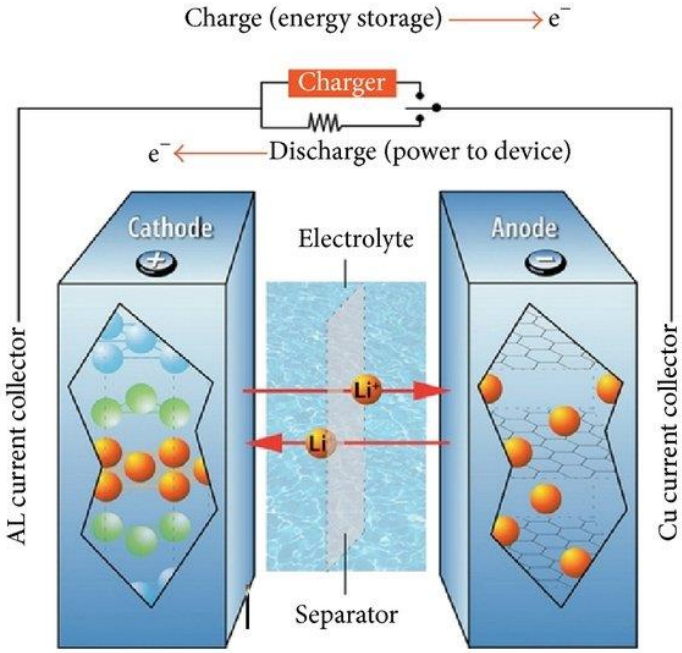

Figure 2.2. *Schematic representation of the charge-discharge event in rechargeable lithium-ion batteries [23].*

2.1. Cathode Active Substances Used In Lithium-Ion Batteries

The performance of lithium-ion batteries is highly dependent on the cathode active materials used. The cathode electrodes used in lithium-ion batteries have a solid network structure that can store guest ions. Guest ions can be added or removed reversibly within this network structure. In lithium-ion batteries, the chemical potential and the amount of lithium ion determine the voltage and charge capacity of the battery. In these batteries, the number of cycles of the battery is determined by the chemical and mechanical stability of the cathode active substance. In order for a compound to be used as a cathode active substance, it must provide the following properties [24];

- Its specific capacity should be high.
- The crystal lattice should contain gaps of appropriate size to allow lithium ions to settle.
- The reactions to occur must be fast enough to allow ion movement.
- The electrode potential should change little with the amount of lithium.
- In order for the battery to have a long life, the cathode material must have electrochemical reversibility.

- For high capacity, the amount of lithium doped per formula unit should be large.
- The cathode material must be inert to other cell components over the entire potential range.
- There should be no gaps in the crystal lattice large enough for solvents to settle.
- For the charge and discharge rate to be high, the diffusion rate of lithium must be high.
- The cathode should have a high potential for lithium.
- It should be stable in the electrolyte.
- It should be environmentally friendly and non-toxic.
- It should be easy to process.
- The material should be cheap and easily available.
- It should be able to charge and discharge 500-1000 with minimum capacity loss.
- It should have a long shelf life.
- Size increases should not negatively affect performance.

The structures suitable for cathode electrodes in lithium-ion batteries are generally metal halogenides, polyanion compounds and transition metal oxides. These compounds can be of various structures. These are layered crystal structures such as spinel, olivine and tavorite. Cathode materials with a layered structure such as $LiCoO_2$ are among the first commercially studied cathode compounds due to their easy synthesis, long cycle life and high capacity. Among the halogenite based cathode electrodes, $LiTiS_2$ has a long cycle life, so it has been researched and commercialized by Exxon. In addition to these, the most investigated cathode materials are transition metal oxides and polyanion compounds because of their high operating voltage and high energy storage capacity [25,26].

Table 2.1. *Characteristic properties of various cathode compounds [27].*

Crystal Structure	Compound	Capacity (mAh g^{-1}) Theoretical/Experimental	Volumetric Capacity (mAh.cm^{-3}) Theoretical/Experimental	Average potential (V)

	$LiTiS_2$	225/210	697	1,9
	$LiCoO_2$	274/148	1363/550	3,8
	$LiNiO_2$	275/150	1280	3,8
Layered	$LiMnO_2$	285/140	1148	3,3
	$LiNi_{0,33}Mn_{0,33}\ Co_{0,332}$	280/160	1333/600	3,7
	$LiNi_{0,8}Co_{0,15}Al_{0,05}O_2$	279/199	1284/700	3,7
	$LiMnO_3$	458/180	1708	2,8
Spinel	$LiMn_2O_4$	148/120	596	4,1
	$LiCo_2O_4$	142/84	704	4
	$LiFePO_4$	170/165	589	3,4
Olivin	$LiMnPO_4$	171/168	567	3,8
	$LiCoPO_4$	167/125	510	4,2
Tavorit	$LiFeSO_4F$	151/120	487	3,7
	$LiVSO_4F$	156/129	484	4,2

2.2. Anode Active Materials Used In Lithium-Ion Batteries

Metallic lithium has been preferred as an anode material in the past due to its high specific capacity, low electrode potential, and low atomic weight. However, despite these properties, it is costly to store for a long time due to being extremely reactive in humid environments, and it causes branching in the lithium metal during long-term charging/discharging, causing the battery to burn and explode. Due to safety problems, researchers have started to search for new anode materials. As a result, carbonaceous materials, which are safer than lithium metal, have been used as anode material in lithium-ion batteries. Although its capacity is lower than that of lithium metal, it has taken the place of lithium because it allows safe and reversible operation. However, due to its low capacity, scientists started researching to find new anode materials. The parameters considered during the research of these new anode materials are; capacity, availability on earth, reliability during the life of the battery, environmental impact, cost and manufacturability.

As a result of the researches, it was observed that lithium alloyed with various metals and the production of lithium alloy anodes was carried out. Metals that lithium alloys; Mg, Ca, Ali Si, Ge, Sn, Pb, As, Sb, Bi, Pt, Ag, Au, Zn, Cd, et al. It was observed

that carbon-based anodes reached a capacity value of 372 $mAhg^{-1}$, while metals such as Sn, Si, Pb, As, Sb, Al reached higher capacity values.

Alloy type anode electrodes used in lithium-ion batteries have high volumetric and gravimetric capacity. However, the commercial use of these electrodes is restricted since the volumetric changes that occur after the litation and the delitation cause the active particles to break up and the electrical connection to break through the current collector. This volume change at the anodes results in electrolyte separation, loss of lithium, and increased cell impedance. Alloy anodes therefore have short cycle life at high mass loadings, loss of active substance and increased cell impedance.

Si (specific capacity 4200 $mAhg^{-1}$ in the first cycle) and Sn (specific capacity 996 $mAhg^{-1}$ in the first cycle) based anode materials provide maximum lithium inflow without deteriorating the structure, but the efficiency decreases rapidly due to the crack formed as a result of the expansion of the structure up to 400% during the reaction with lithium seen. Today, in order to benefit from the superior properties of Si and Sn, some groups work on composite electrodes containing Si or Sn, while some groups work on anode material with the highest level of mechanical stability that can tolerate volumetric changes during charge/discharge. Especially Si anode alloy electrodes are one of the most remarkable materials because of their low distillation potential, high gravimetric and volumetric capacity values, abundant presence in the earth's crust, low cost, chemical stability and non-toxicity.

Today, work continues on new and effective electrode materials to push the limits of energy density, power density, cycle life, cost and safety. Although there are various promising anode and cathode materials, many of them have many problems such as limited electrical conductivity, low ionic conductivity, low thermal stability, high volumetric expansion, dissolution in the electrolyte and mechanical fragility. To overcome these problems, methods such as size reduction, synthesis in composite form, doping, and coating have been developed. In the last 10 years, researches and projects on electrode materials have been carried out. New material types and strategies show that lithium-ion batteries will have a huge impact on our lives in the future.

Table 2.2. *Some anode materials and performance review [28].*

Anode Material	Average Potential (V)	Specific Capacity (mAh/g)	Irreversible Capacity(mAh/g)	Specific Energy (Wh/kg)
Li metal		3700		
Coke-Based		200	55	
Graphite (LiC_6)	0,1-0,3	350	50	30-70
Hard Carbon (LiC_6)		600-100	200	
MCMB		305	9	
Titanate (Li_4TiO_{12})	1,0-2,0	160		160-320
Si ($Li_{4,4}Si$)	0,5-1,0	4212		210-420
Ge ($Li_{4,4}Ge$)	0,7-1,2	1624		110-190
Sb (Li_3Sb)	1,0	665		
Sn ($Li_{4,4}Sn$)	0,5	990		

2.3. Separators

In lithium-ion batteries, the separator prevents the anode and cathode from touching each other and short-circuiting, and ensures the desired mass transfer. It is located between the anode and cathode electrode. The properties are the important components in batteries containing liquid electrolytes and allow free ion passage.

The characteristics of the separators should be evaluated according to the needs and the separator that meets best this need should be selected. The separators must provide some features, these are [29];

- It must be electronically insulating.
- It must be electrochemically and chemically stable to electrolyte and electrode materials.
- The battery must be strong enough to withstand high pressure during installation.

- Its thickness should be the same all over.
- In order to provide high ionic conductivity, it must be able to absorb liquid electrolyte and have sufficient porosity for this.

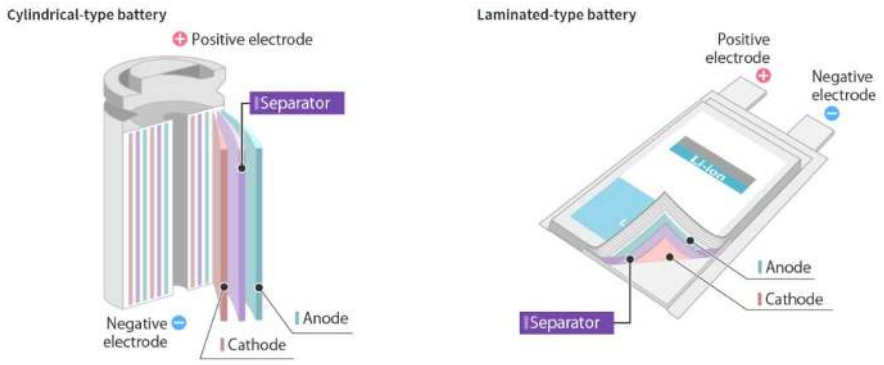

Figure 2.3. *Separators and their positions in cylindrical and laminated batteries [30].*

2.4. Electrolytes

Electrolytes provide charge transport between two electrodes. Most of the electrolytes used in lithium-ion batteries consist of a lithium salt dissolved in two or more organic solvents. Usually two solvents are used. The reason why these solvents are used as a mixture is to take advantage of their different chemical and physical properties. In the operation of lithium-ion batteries, the electrolyte standing between the positive and negative electrodes is of vital importance. Due to its importance, electrolytes are expected to have various properties. These are;

- Solvents must have a low melting point and a high boiling point.
- It must dissolve the salts sufficiently, and for this, the dielectric constant must be high.
- It must be in an electrochemically stable state.
- It should be fluid enough to allow ion transfer.
- It must be inert to all components of the battery.
- It should be safe and economical. It should not be toxic [31].

Four types of electrolytes are used in lithium-ion batteries. They are liquid electrolytes, polymer electrolytes, gel electrolytes and solid electrolytes. Liquid electrolytes refer to a solution of lithium salt in organic solvents consisting of carbonates such as ethylene carbonate and propylene carbonate. The most commonly used solvents

in liquid electrolytes are organic esters and ethers. Polymer electrolyte is a solvent-free liquid with an ionic conductive phase, which is formed as a result of the dissolution of salt in high molecular weight polymers. The biggest advantage of polymer electrolytes is their safety feature due to low volatility and high viscosity as they do not contain flammable and volatile solvents. Gel electrolyte is the ionic material obtained when salt and solvent are mixed with a high molecular weight polymer. Solid electrolytes consist of inorganic ceramics/glasses. These electrolytes are a type of material that conducts electricity by allowing ions to move in their solid phase.

2.5. Solid Electrolytes

Most of the lithium-ion batteries that we use extensively today have organic polymer-based electrolytes that have poor chemical and electrochemical stability and cause safety problems such as flammability. These disadvantages hinder the development of lithium-ion battery technology and cause economic losses. For these reasons, solid electrolytes and new batteries using these electrolytes are being developed, which eliminates safety problems and provides the opportunity to work in high voltages. Considering the current developments, compared to liquid electrolytes, solid electrolytes can be used in the battery industry considering their current and future status.

The choice of electrolyte in lithium-ion batteries is an important factor affecting battery performance. Most liquid electrolytes are stable up to 1.5 V, so these electrolytes cannot be used without reducing the operating voltage and can be oxidized by the cathodes during discharge. Furthermore, the proximity of liquid electrolytes to an oxidizing agent, the cathode, can cause thermal runaways, which can cause fire or explosion. When it is exceeded 1.5 V, it creates a SEI layer that partially passivates the surface. The danger of oxidation is a problem that hinders high voltage cathodes, and therefore the use of organic liquid electrolytes is limited to certain voltage ranges. Although this danger has been reduced over the years, such problems can still be encountered and cause recalls as we have seen in the media. Solid electrolytes are considered as a solution for these limitations. This type of electrolyte provides electrical conduction to liquid electrolytes at ambient temperature, similar to electrolytic solutions, by the movement of ions. These properties show that solid electrolytes can be used in batteries and various energy storage systems [35].

Table 2.3. *Comparison of the properties of liquid and solid electrolytes in lithium-ion batteries [47].*

Parameter	Liquid cell	Solid-state cell
Separator	Flexible	Rigid and brittle ceramic
Production	Low price, large format.	High price, small format
Ionic conductivity	High, near room temperature	Moderate, broad temperature range
Electrolyte safety	Flammable, volatile	Nonflammable, safe, nonvolatile
SEI layer	Yes, affects cycle life	None, longer cycle life
High-voltage cathode materials	No, decomposition	Yes
Thermal stability	Poor	Excellent
Self-discharge	Bad, limited shelf life	Good, longer shelf life
Overcharge	Sensitive	Abuse tolerant
Dendrite growth	Yes	Limited, extended cycle life
Specific energy	Low	High, less inactive materials

Expectations from solid electrolyte materials for the use of solid-state lithium-based batteries in energy storage applications in the future are as follows;

- High ionic conductivity ($\geq 10^{-3}$ S/cm)
- Low activation energy ($\leq$ 1 eV, for easy transport of ions)
- Negligible electronic conductivity ($\leq$ 0.01% × ionic conductivity)
- Large electrochemical window
- In order for the ions to move, a large number of empty spaces with equivalent activation energy must be present in the electrolytes.
- The anion working field must be polarizable
- It must be physically and chemically compatible with the anode and cathode.

Solid electrolytes attract attention due to their long life, mechanical strength and easy shaping. In addition, being stable against lithium, long cycle life, high chemical

stability, high energy density and high reliability are important features. But they have low ionic conductivity.

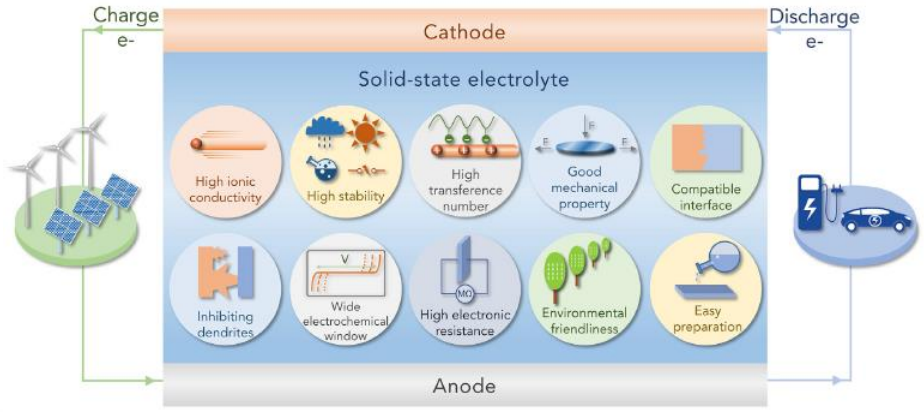

Figure 2.4. *Properties of Solid Electrolytes [34]*

The 1960s can be considered the starting point for solid electrolytes. The idea of using these electrolytes in batteries came about in the 1960s. In 1960, β-alumina was observed to carry fast 2D sodium ions and was used in high temperature sodium sulfide batteries. After these achievements were observed, practical applications of solid electrolytes increased after 1960 [32].

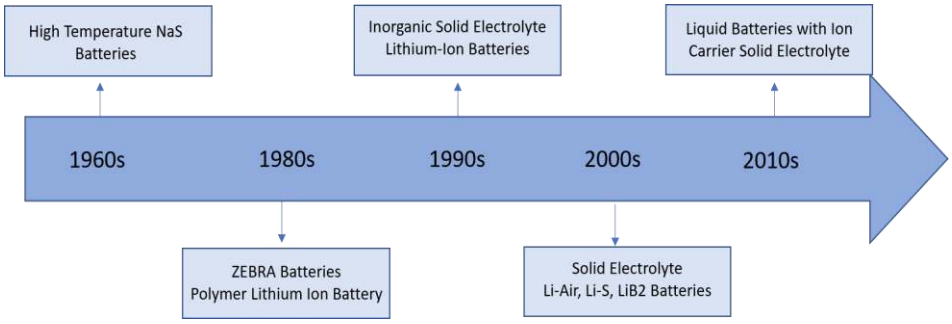

Figure 2.5. *Historical Development of Solid Electrolytes [33].*

Studies on solid electrolytes have focused on these two solid electrolyte types, since sulfide-based solid electrolytes have high ionic conductivity and oxide-based solid electrolytes have high ionic conductivity as well as high chemical stability.

2.5.1. Organic polymer solid electrolytes

There are two types of polymer solid electrolytes. These are gel polymer solid electrolyte and solvent free solid polymer electrolyte. Organic polymer electrolytes have important advantages such as their ability to easily contact the electrode with the electrolyte, their high flexibility and easy processing [36]. Although gel polymer solid electrolytes exhibit weaker mechanical properties, they provide high ionic conductivity and the ion conduction mechanism is similar to liquid electrolytes. These electrolytes are formed by incorporating liquid electrolyte solutions into the polymer matrix, and the gel matrix increases the reliability of the liquid solvent. The ionic conductivity of the gel polymer solid electrolyte is high (~10^{-3} S/cm at room temperature), as the liquid solvent trapped in the gel polymer matrix facilitates ion transport [38].

Solvent-free solid polymer electrolytes are mechanically stronger and the ion conduction mechanism is as follows: sodium salts are dissolved in the polymer carrier, and then sodium ions are transported inside the polymer carriers by the local movement of the polymer chains. In this electrolyte, sodium salts are dispersed in polymer chains instead of liquid solvents. This structure solves the problem of leakage and evaporation, which are the problems of organic solvents. Compared with gel polymer solid electrolytes, solvent-free polymer solid electrolytes have low ionic conductivity (10-9~10^{-6} S/cm), but it is observed to increase depending on temperature (10^{-4}~10^{-3} S/cm- above 80 °C) [37].

2.5.2. Composite solid electrolytes

Since the early 2000s, there have been extensive efforts to use solid electrolytes in lithium-ion, lithium sulfur and lithium air batteries. Although there are some studies focusing on purely inorganic solid ceramic electrolytes or organic solid polymer electrolytes, solid composite electrolytes that take the benefit of the advantages and eliminate the disadvantages of both inorganic and organic solid electrolytes have been the focus of attention. Inorganic ceramic electrolytes are used as fillers to increase the mechanical strength and ionic conductivity of composite solid electrolytes [39]. These fillers can be passive ceramic fillers such as SiO_2, TiO_2, $BaTiO_3$, as well as active ceramic fillers such as NASICON [40]. Various polymers such as PEO, PAN, PVDF, PMMA have been used as polymer matrix to develop solid composite electrolytes. The use of polymer matrix in composite solid electrolytes provides several advantages. The

flexibility of the electrolyte increases due to the addition of polymer, the presence of polymer minimizes the resistance at the electrode-electrolyte interface, polymers are cheaper than inorganic ceramic electrolytes and easier to process [39].

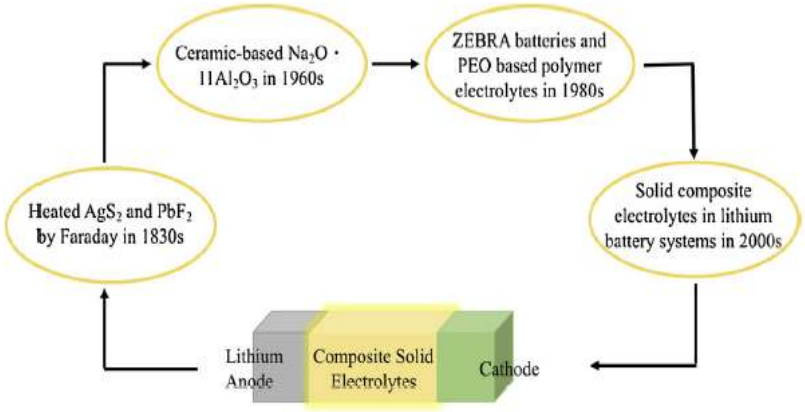

Figure 2.6. *Historical progress of the development of solid composite electrolytes and their applications in lithium battery systems [39].*

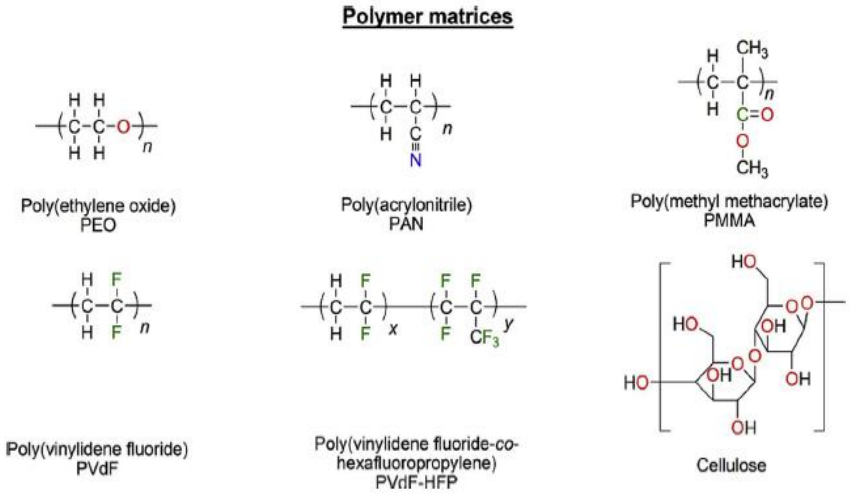

Figure 2.7. *Chemical structures of commonly studied polymer matrices for solid composite electrolytes [39].*

2.5.3. Inorganic solid electrolytes

Compared with other solid electrolytes, inorganic solid electrolytes have been the subject of extensive research thanks to their high ionic conductivity and low electronic conductivity. Inorganic solid electrolytes consist of locally symmetrical and mobile ions. The mobile ions jump from one region of the structure to the adjacent region with point

defect movements and thus provide ion transmission. The conductivity of these compounds increases with temperature, since ionic conduction occurs by point-defect movement. This makes inorganic solid electrolytes ideal for high temperature applications. However, the ionic conductivity in some inorganic compounds is quite high even at low temperatures. Therefore, various ceramic electrolytes are being investigated for use in lithium-ion batteries.

The ionic conductivity of these electrolytes depends on the number of mobile ions and vacancies, the energy threshold required for jumping, and the number of jump and gap regions [41]. There are four main types of inorganic solid electrolytes being investigated to be used in lithium-ion batteries because of their superior safety properties. These are NASICON, LISICON, Perovskite and Garnet type electrolytes [42]. Although the LGPS family of solid electrolytes has high ionic conductivity, it is not considered due to its toxicity. The non-toxic Garnet type solid electrolyte $Li_7La_3Zr_2O_{12}$ (LLZO) is a promising electrolyte for the reason that it has relatively high ionic conductivity. Garnet-type cubic $Li_7La_3Zr_2O_{12}$ (LLZO) solid electrolytes have become the focus of solid-state lithium-ion batteries. Since their ionic conductivity is not high enough to enable their use, there are some attempts to develop it with different production and doping methods.

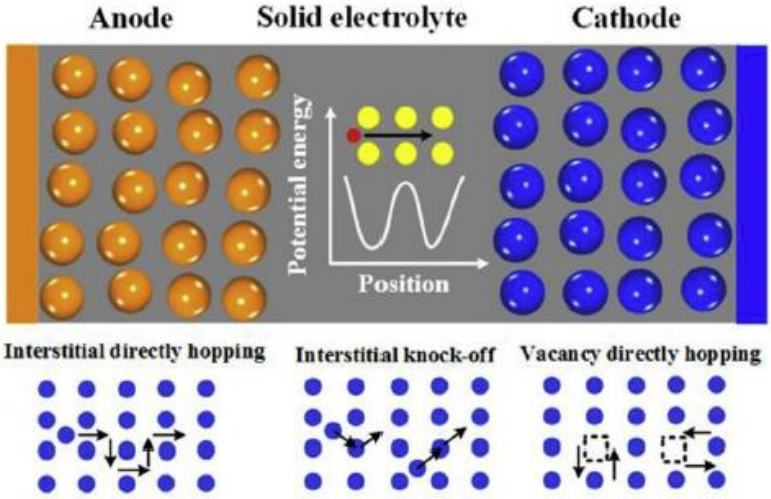

Figure 2.8. *Schematic representation of various types of mobile ion diffusion in a solid inorganic electrolyte [49].*

Perovskite is known as ABO_3, and BO_3 surrounds the ions of the A site, becoming the framework of the crystal structure. Currently, the most studied material in perovskite

structure is $Li_{0.34}La_{0.51}TiO_{2.94}$ (LLTO). The ionic conductivity of this material is 2×10^{-5} S/cm, which is a high value compared to other materials. LLTO has such high ionic conductivity because its structure is deformed when there are not enough A site ions. However, the ionic conductivity of LLTO differs between its total ion conductivity (2×10^{-5} S/cm) and bulk ion conductivity (1×10^{-3} S/cm). This shows that the movement of Li^+ ions is limited by the contact resistance formed at the grain boundaries. In order to solve this problem, various researches have been carried out to find the optimum heat treatment temperature [45].

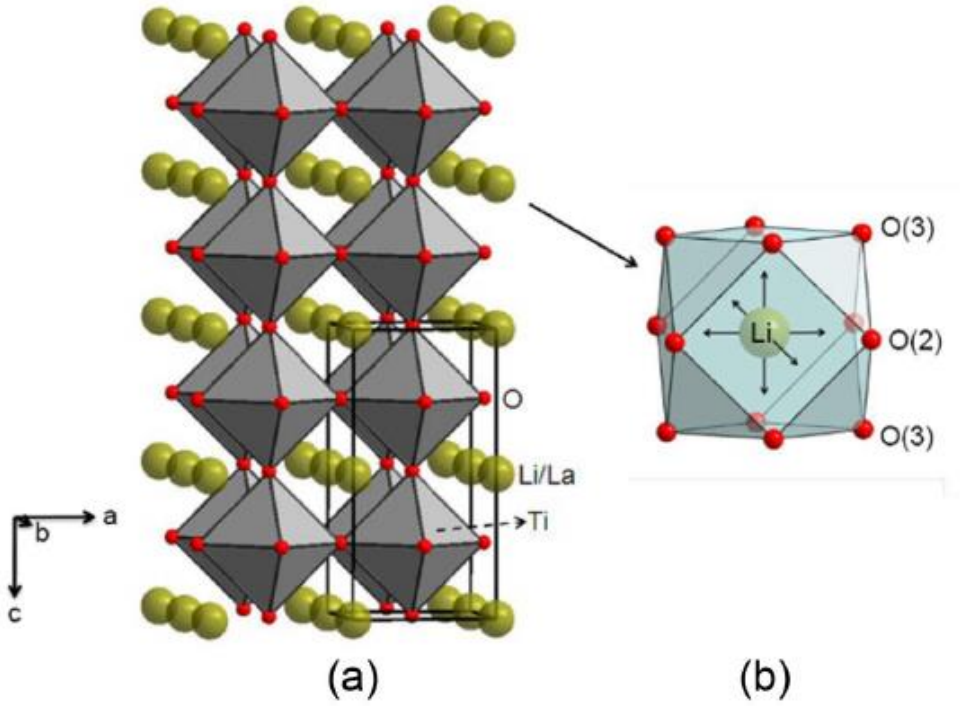

Figure 2.9. *Crystal structure of Perovskite type solid electroliytes [45].*

The general structure of NASICON (Na super ionic conductor) solid electrolyte is known as $AM_1M_2P_3O_{12}$ / $AM_1M_2(PO_4)_3$. The AO_6 octahedron and PO_4 tetrahedrons share six oxygen atoms at the edges to form a three-dimensional skeleton. Three-dimensional channels are formed in the crystal lattice and the transmission of ions is possible through these channels. β-alumina, $Na_3Zr_2Si_2PO_{12}$ and $NaZr_2$ $(PO_4)_3$ are materials that represent the NASICON structure. Currently, studies are carried out on $Li_{1+x}Al_xTi_{2-x}(PO_4)_3$ (LATP) $(0 \leq x \leq)$ [45].

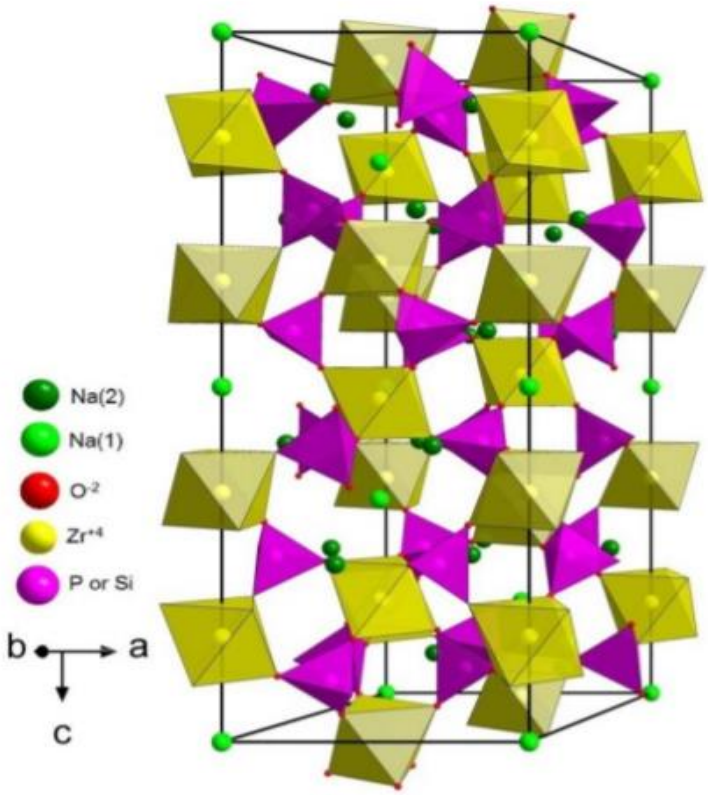

Figure 2.10. *Crystal structure of NASICON type solid electrolytes [44].*

LISICON, short for lithium super ionic conductor, has the structural formula $Li_{2+2x}Zn_{1-x}GeO_4$. Due to its structure, lithium ions are distributed between two different octahedron sites and move between them. A typical example of LISICON electrolytes is $Li_{14}ZnGe_4O_{16}$ with Li and Zn in the A regions and Ge or V in the B regions [42], and this material has a high ionic conductivity of 1.2×10^{-1} S/cm at 300 ºC but 10^{-7} S/cm at room temperature. However, Thio-LISICON (for example, Li_4GeS_4 and Li_5AlS_4), in which the oxygen in the structure is replaced by sulfur, has a 100 times higher ionic conductivity and researchers are developing methods to replace the oxygen in LISICON with sulfur [45].

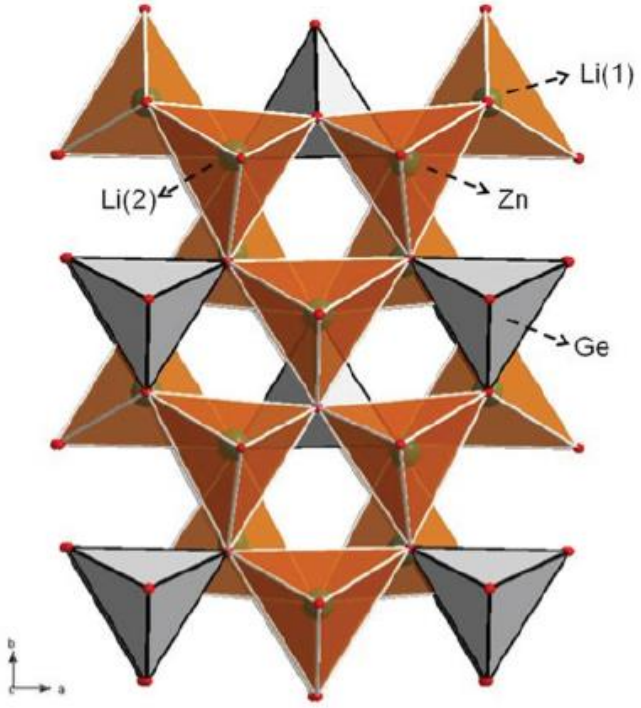

Figure 2.11. Crystal structure of LISICON type solid electrolytes [45].

The structure of the garnet-type solid electrolyte consists of a tetrahedron, a dodecahedron, and an octahedron, which may be referred to as regions A, B, and C, respectively, and coordinating oxygen atoms. It is expressed as $A_3B_3C_2O_{12}$. Among the garnet electrolytes, the most studied compound was Lithium Lanthanum Zirconia Oxide (LLZO). The LLZO electrolyte has ionic conductivity values of 5 x 10^{-4} S/cm in the cubic structure and 1.6 × 10^{-6} S/cm in the tetragonal structure. Experiments are carried out using various dopants to obtain a stable cubic structure. However, in order to synthesize a garnet electrolyte, long-term (12-24 hours) heat treatment is required at temperatures of 1100 ºC and above. During these processes, Li^+ ions become volatile, and the garnet structure may collapse or a solid electrolyte with low ionic conductivity is synthesized. Experiments on dopants and heat treatment process are ongoing to eliminate these problems [45].

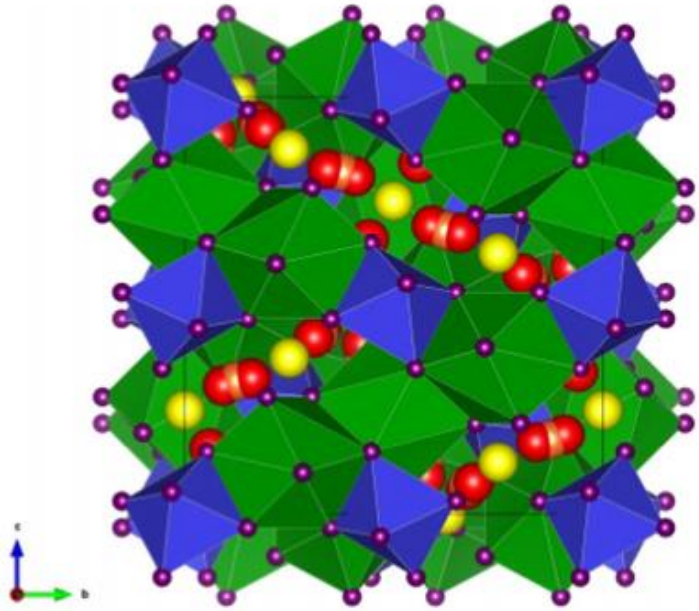

Figure 2.12. Crystal structure of Garnet type solid electrolytes [46].

There are some advantages of using inorganic solid electrolytes in rechargeable batteries: high li-ion transfer number at room temperature, compatibility with some electrodes that cannot coexist with liquid electrolyte, good electrochemical stability, Compared to polymer-based electrolytes, inorganic solid electrolytes with high ionic conductivity and high Na ion transfer number at room temperature can effectively improve battery performance thanks to their both long-term cycle life and high power density [41].

In the studies so far, the low ionic conductivity and poor stability of inorganic solid electrolytes at ambient temperature inhibits commercial applications of inorganic solid electrolytes in all solid state lithium-ion batteries. The ionic conductivity of most inorganic solid electrolytes is lower than that of liquid electrolytes at room temperature. Many inorganic solid electrolytes are unstable at low potentials against anodes such as graphite and metallic lithium, while some are reactive against cathode materials, resulting in high interface resistance [41]. In addition, it has been determined that ionic conductivity varies from grain to grain boundaries even within the same electrolyte material because of regional differences [37]. Therefore, optimization and commercialization of inorganic solid electrolytes with high stability and ionic conductivity is of vital importance for all solid state batteries.

Table 2.4. *Reported ionic conductivities of inorganic solid electrolytes including LISICON-like, NASICON-like, perovskite, and garnet [41].*

Clasification	Ionic conductivity (S/cm)	Temperature (K)
LISICON-like		
$Li_7P_3S_{11}$	3.20×10^{-3}	298
β-Li_3PS_4	3.0×10^{-2}	500
$Li_{9.6}P_3S_{12}$	1.00×10^{-2}	298
$Li_{10}GeP_2S_{12}$	1.20×10^{-2}	298
$Li_{3.25}Ge_{0.25}P_{0.75}S_4$	2.20×10^{-3}	298
$Li_{3.4}Si_{0.4}P_{0.6}S_4$	6.4×10^{-4}	298
$Li_{9.54}Si_{1.74}P_{1.44}S_{11.7}Cl_{0.3}$	2.50×10^{-2}	298
NASICON-like		
$LiTi_2(PO_4)_3$	3.83×10^{-7}	298
$Li_{1.3}Al_{0.3}Ti_{1.7}(PO_4)_3$	3.00×10^{-3}	298
$Li_{1.2}Ti_{1.8}Sc_{0.2}(PO_4)_3$	2.5×10^{-3}	298
$Li_{1.6}Al_{0.}\ Ge_{0.8}(PO_4)_3$	0.70×10^{-3}	298
$Li_{1.3}Al_{0.3}Ti_{1.7}(PO_4)_3$	1.21×10^{-3}	298
$Li_{1.4}\ Al_{0.4}\ Ti_{1.6}\ (PO_4)_3$	5.63×10^{-3}	298
$Li_{1.3}Al_{0.3}Ti_{1.7}(PO_4)_3$	6.20×10^{-3}	298
Pervoskite		
$La_{0.57}Li_{0.29}TiO_3$	1.60×10^{-3}	300
Li_3OCl	0.85×10^{-3}	298
$Li_3OCl_{0.5}Br_{0.5}$	1.94×10^{-3}	298
Li_2OHCl	2.8×10^{-3}	468
Garnet		
$Li_7La_3Zr_2O_{12}$	3.10×10^{-4}	298
$Li_{6.55}La_3Zr_2Ga_{0.15\sim0.3}O_{12}$	1.30×10^{-3}	298
$Li_7La_3Zr_2O_{12}$ (0.9 wt% Al)	3.55×10^{-4}	298
$Li_{6.4}La_3Zr_{1.4}Ta_{0.6}O_{12}$	1.00×10^{-3}	298
$Li_{6.5}La_3Zr_{1.75}Te_{0.25}O_{12}$	1.02×10^{-3}	303
$Li_{7.06}La_3Zr_{1.94}Y_{0.06}O_{12}$	9.56×10^{-4}	298
$Li_{6.5}La_{2.9}Ba_{0.1}Zr_{1.4}Ta_{0.6}O_{12}$	8.30×10^{-4}	300
$Li_{6.5}La_3Zr_{1.5}Ta_{0.5}O_{12}$	7.94×10^{-4}	300
$Li_{6.4}La_3Zr_{1.7}W_{0.3}O_{12}$	7.89×10^{-4}	303
$Li_{6.6}La_3Zr_{1.6}Sb_{0.4}O_{12}$	7.70×10^{-4}	303

2.5.3.1. Sulfide based inorganic solid electrolytes

Sulfide based solid electrolytes are important solid electrolytes because they require low temperature during their synthesis and fast sodium ion conduction at room temperature. Since sulfide-based electrolytes have higher ionic conductivity than oxide-based electrolytes, they are seen as one of the promising electrolyte types in lithium batteries [48]. The reason why they have higher ionic conductivity is that the sulfur ions are larger than the oxide ions, leaving wider channels in the structure that act as conductive orbits. In addition, the polarization of sulfur ions is higher than that of oxide electrolytes. In this way, because of the high polarization, lithium ions are more weakly attracted to the structure formed in sulfur than the structure formed in the oxide, and they can be more mobile in the sulfur-based structure [50].

Due to the softness of the electrolyte during the assembly of the battery cell, only cold pressing is sufficient to form a good contact between the sulfide-based solid electrolyte and the electrode materials. In this case, it reduces the cost of industrial production [51].

Table 2.5. *Ionic conductivity σ(RT) and activation energy E_a(eV) of sulfide-based solid electrolytes at room temperature [48].*

Electrolyte	**Structure, lattice Parameters (Å)**	**σ (RT) (S/cm)**	**E_a (eV)**
Li_6PS_5Cl	amorphous	$3.3x10^{-5}$	0.38
	crystalline cubic, a = 9.85	$1.9x10^{-9}$	
Li_6PS_5Br	amorphous	$3.2x10^{-5}$	0.32
	crystalline, a = 9.98	$6.8x10^{-3}$	
Li_6PS_5I	amorphous	$2.2x10^{-4}$	0.26
	crystalline, a = 10.142	$4.6x10^{-7}$	
β -Li_3PS_4	amorphous	$2.8x10^{-4}$	0.37
$Li_{3.25}Si_{0.25}P_{0.75}S_4$	crystalline, orthorhombic	$1.2x10^{-3}$	0.20
	a = 13.158, b = 8.029, c = 6.129		
$Li_7P_3S_{11}$	crystalline, triclinic	$0.2x10^{-3}$	0.2
	a=12.501, b= 6.031, c=12.530		
$Li_7P_2S_8I$	crystalline, orthorhombic	$6.3x10^{-3}$	0.31
$Li_7P_2S_8I$	crystalline, orthorhombic	6.010^{-3}	0.27
	a = 12.703, b = 8.45, c = 5.94		
$Li_{15}(PS_4)_4Cl_3$	crystalline, a = 14.308	$4.0x10^{-8}$	0.59
$Li_{14.8}Mg_{0.1}(PS_4)_4Cl_3$	a = 14.323	$2.0x10^{-7}$	0.41

$Li_{10}GeP_2S_{12}$	crystalline, tetragonal a = 8.717; c = 12.634	$12x10^{-3}$	0.24
$Li_{10}SiP_2S_{12}$	crystalline, tetragonal a = 8.658, c = 12.519	$2.0x10^{-3}$	0.30
$Li_{10}SiP_2S_{11.3}O_{0.7}$	crystalline, tetragonal a = 8.666, c = 12.529	$3.1x10^{-3}$	0.32
$Li_{10}SnP_2S_{12}$	crystalline, tetragonal a = 8.734, c = 12.773 Å	$6.0x10^{-3}$	0.31
$Li_{10}Si_{0.3}Sn_{0.7}P_2S_{12}$	crystalline, tetragonal a = 8.741, c = 12.757	$8.0x10^{-3}$	0.29
$Li_{10.3}Al_{0.3}Sn_{0.7}P_2S_{12}$	crystalline, tetragonal a = 8.743, c = 12.787	$5.0x10^{-3}$	0.29
$Li_{9.42}Si_{1.02}P_{2.1}S_{9.96}O_{2.04}$	tetragonal	$1.1x10^{-4}$	0.23
$Li_{9.54}Si_{1.74}P_{1.44}S_{11.7}Cl_{0.3}$	crystalline, tetragonal a = 8.709, c = 12.569	$2.5x\ 10^{-2}$	0.23

2.5.3.2. Oxide based inorganic solid electrolytes

Unlike sulfide-based inorganic solid electrolyte materials, oxide-based inorganic solid electrolyte materials have high chemical stability under atmospheric conditions. Since sulfide-based inorganic solid electrolyte materials have chemical instability even to moisture, these electrolytes must be produced in a controlled and inert environment. oxide-based inorganic solid electrolytes can be produced and used in air. As a result of their high chemical stability, oxide-based electrolytes promise long cycle life and high power density. These two properties, which are vital for batteries, make the use of these solid electrolytes in solid state batteries attractive.

Oxide-based inorganic solid electrolytes have large energy gaps between the valence and conduction bands, providing high stability at high voltages. Table 2.6. summarizes the structural and electrical properties of various oxide-based inorganic solid electrolytes.

Table 2.6. *Ionic conductivity σ(RT) and activation energy Ea(eV) of oxide-based solid electrolytes at room temperature [48].*

Electrolyte	Structure, lattice Parameters (Å)	σ (RT) (S/cm)	E_a (eV)
$Li_7La_3Zr_2O_{12}$	garnet type, cubic a = 12.82–13.01	10^{-3}–10^{-4}	0.31–0.34
$Li_7La_3Zr_2O_{12}$	crystalline, tetragonal a = 13.068, c = 12.66	10^{-5} -10^{-6}	0.40-67
$Li_{6.75}La_3Z_{1.75}Ta_{0.25}O_{12}$	crystalline, cubic a = 12.96	$0.87x10^{-3}$	0.22
$Li_{6.5}La_3Zr_{1.5}Ta_{0.5}O_{12}$	crystalline, tetragonal a = 12.929	$0.75x10^{-3}$	-
$Li_{6.15}La_3Zr_{1.75}Ta_{0.25}Al_{0.2}O_{12}$	crystalline, cubic, a = 12.95	$0.37x10^{-3}$	0.30
$Li_{6.25}La_3Zr_2Al_{0.25}O_{12}$	crystalline, cubic, a = 12.96	$0.68x10^{-3}$	-
$Li_{6.15}La_3Zr_{1.75}Ta_{0.25}Ga_{0.2}O_{12}$	crystalline, cubic, a = 12.95	$0.41x10^{-3}$	0.27
$Li_{6.25}La_3Zr_2Ta_{0.25}Ga_{0.2}O_{12}$	crystalline, cubic a= 12.97	$1.04x10^{-3}$	-
$Li_{1.5}Al_{0.5}Ti_{1.5}P_3O_{12}$	crystalline, hexagonal a = 8.50, c = 20.52	$3.0x10^{-3}$	0.26
$Li_{0.34}La_{0.56}TiO_3$	crystalline, cubic, a = 3.872	$1.53x10^{-3}$	0.33
$Li_4Al_{1/3}Si_{1/6}Ge_{1/6}P_{1/3}O_4$	LISiCON type structure	$0.9x10^{-3}$	0.28
$Li_{3.53}(Ge_{0.75}P_{0.25})_{0.7}V_{0.3}O_4$	LISICON-type	$5.1x10^{-5}$	0.43
$Li_{2.88}PO_{3.73}N_{0.14}$(LIPON)	amorphous	$3.3x10^{-6}$	0.54
$Li_{3+x}Si_xP_{1-x}O_4$ (LiSiPON)	amorphous	$2.06x10^{-5}$	0.45

In 1976, Goodenough et al. conducted studies on $Na_{1+x}Zr_2Si_xP_{3-x}O_{12}$ (NASICON), which provides a conductivity of ≤ 5 S/cm at 300 ºC for x=2. The NASICON structure has a three-dimensional skeleton and its ion transport properties are related with the lattice volume. The conductivity values obtained from this study were comparable to β-alumina, which was one of the best solid electrolytes at that time, and it was mentioned that it is possible to replace Na^+ ions with Li^+, Ag^+ and K^+ ions. In 1977 Shanon and et al.

described a set of electrolyte systems. These: $Li_{2+x}C_{1-x}B_xO_3$, $Li_{3-x}B_{1-x}C_xO_3$, $Li_{4+x}Si_{1-x}Si_{1-x}Al_xO_4$, $Li_{4-x}Si_{1-x}P_xO_4$, $Li_{4-2x}Si_{1-x}S_xO_4$, and $Li_{5-x}Al_{1-x}Si_xO_4.Li_{0.8}Zr_{1.8}Ta_{0.2}P_3O_{12}$. Later, many researchers experimented with electrolytes as additives or electrolytes. In 1978, Levasseur et al. conducted a study on borate-type amorphous oxide-based glassy electrolytes and their conductivity was $>10^{-4}$ and 10^{-6} S/cm at 350 ºC and 25 ºC, respectively [48].

Different types of oxide electrolyte systems based on NASICON, LISICON, garnet, perovskite type crystalline materials have been reported in the literature. Among all compositions, garnet-type Ta-, Ga-, Al-doped $Li_7La_3Zr_2O_{12}$ (LLZO) and $Li_{1.3}Al_{0.3}Ti_{1.7}(PO_4)_3$ (LATP) oxide-based solid electrolytes have been studied for solid-state batteries because of their good conductivity. The ionic conductivity of these garnet-type solid electrolytes, which is resistant even to molten lithium, is 10^{-5} S/cm. However, when elements such as La and Zr are replaced, it increases to the value of 10^{-3} S cm^{-1} [48].

It should be noted that ceramic solid electrolytes such as LLZO and LATP are polycrystalline and show grain/grain boundary microstructure. These electrolytes have high grain boundary resistance. Reducing the sintering temperature as much as possible reduces the grain boundary resistance, as well [52]. The sintering temperature can be reduced with additives that support sintering.

3. THE AIM OF THE STUDY

Energy consumption in the world is increasing day by day with the development of technology and human needs. As a result of this energy need, CO_2 emissions increase in relation with consumption and this causes serious damages to the environment. Thanks to the developing technology, renewable energy sources have been used for a long time to prevent these damages and systems are being developed to store the energy obtained from these sources. Storage systems are just as important as generating energy so that energy can be used in cars, machines, computers and mobile devices. Lithium-ion batteries appear at this stage. However, lithium-ion batteries have some problems such as sudden explosions and fires due to the liquid electrolyte they contain. Inorganic solid electrolytes are one of the reliable solutions for these safety problems. Among the inorganic solid electrolytes, $Li_7La_3Zr_2O_{12}$ (LLZO) is a promising solid electrolyte in lithium-ion batteries with its high performance in stability, safety and ionic conductivity. However, the ionic conductivity values of this electrolyte still cannot reach the conductivity values of commercially used liquid electrolytes.

Garnet type LLZO exists in two stable phases. These are the cubic and tetragonal phases. Crystal structures of Cubic and Tetragonal LLZO structures are shown in Figure 3.1. Although the tetragonal phase is stable at room temperature, its ionic conductivity is low. Cubic LLZO has high ionic conductivity but it is difficult to stabilize at room temperature. Element doping is one of the most effective wa”ys to stabilize the cubic phase of LLZO and increase its ionic conductivity. In addition, the dopant causes nano-defects in the structure and these defects enable ion transport.

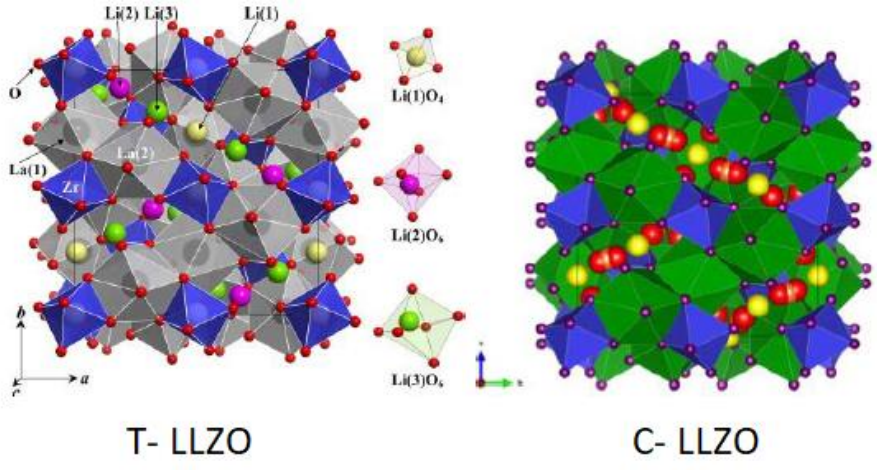

Figure 3.1. Crystal structure of tetraganol LLZO(T-LLZO) and cubic LLZO(C-LLZO) [46].

Therefore, doping with various elements such as Y [53], Ga [54], Al [55-56], Ta [57], Nb [58], Fe [59] and Bi [60] have been investigated to increase the ionic conductivity. The conductivity and densification results, which are obtained as a result of Fe [59] and Al [55-56] doping, are remarkable. However, Fe_2O_3 and Al_2O_3 were used as Fe and Al sources in these studies. These powders are costly and require additional purification steps. Fe and Al atoms can only be replaced by Li atoms and are occupied in Li sites according to imperfect energy calculations [61]. In addition to these studies, doping with multi-site occupied elements has recently received a lot of attention in the LLZO. Studies reported in the literature that examine doping with multi-site occupation revealed that ionic conductivity improved. In short, any additive can have characteristic effects on LLZO's performance in various fields.

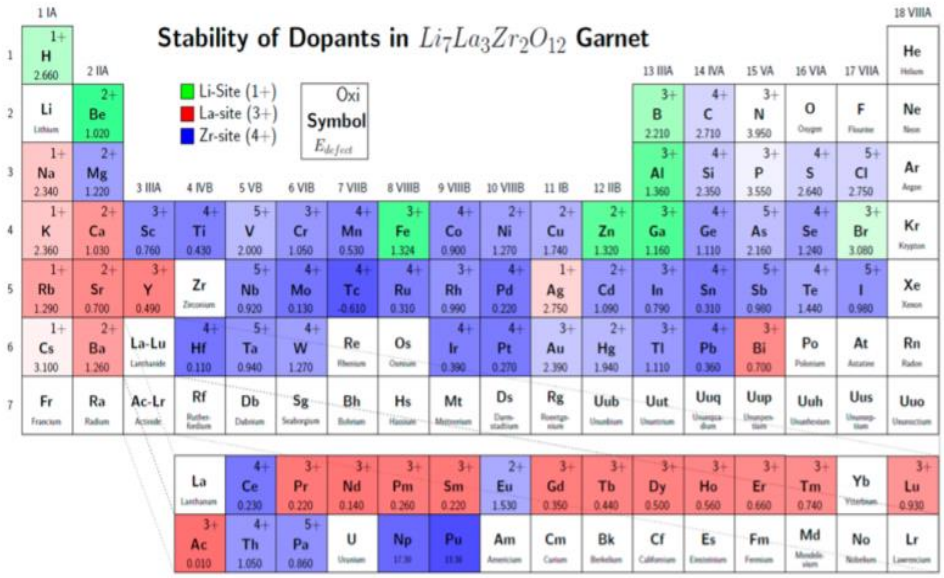

Figure 3.2. *Site and oxidation state preference for various doped elements. The color shows the most stable cation site (green for Li-site, red for La-site, and blue for Zr-site) [61].*

Red mud is the waste material produced during the production of alumina from bauxite ores by the bayer process. Depending on the type of ore and operating conditions, approximately 0.8-1.5 tons of red mud are produced for each ton of alumina. According to estimates, 70 million tons of red mud are produced annually in the world. Red mud is

pumped in factories and collected in a tailings dam, which means loss of land. In addition, this stored mud brings with it the risk of water and environmental pollution due to its high alkaline properties and containing toxic metals. Numerous studies have been conducted to evaluate red mud, but no significant economic benefit has been observed [62].

Red mud consists of various oxides/hydroxides of elements such as Fe [59], Al [55-56], Si [68], Na, Ca [66] and Ti [67]. Each of these elements can positively or negatively affect the structure, morphology and performance of LLZO [65]. The influence of the elements Fe, Al and Si on the cubic phase stabilization of LLZO has been proven. It has been reported that Ti can replace Zr site and Na can replace La site in cubic LLZO structure [67]. However, no information based on the effect of Ti and Na additions on electrochemical performance could be gathered from published studies. It has been found that Ca–La replacement in cubic LLZO structure reduced the lattice constant. But Ca doping showed very limited enhancement on the electrochemical performance [66].

Thanks to the multi-element content of red mud, which is produced as a waste material during the production of alumina from bauxite ores, it shows a co-doping effect with multi-site occupations. This study discusses the use of red mud as a multi-element additive in LLZO synthesis in terms of microstructure-property-performance relationship and the processes before sintering.

4. MATERIALS AND METHODS

Production scheme of Tetragonal LLZO(T-LLZO) and Red mud doped LLZO, in other words cubic LLZO(RMD-LLZO) powders are given in Figures 4.1. and 4.2. Preparation of calcined T-LLZO powder: $LiOH.H_2O$ (Alfa Aesar), La_2O_3 (Sigma Aldrich), ZrO_2 (Sigma Aldrich) powders in stoichiometric ratios and high purity were mixed in a mortar mill for 1 hour (Retsch, RM200). The prepared T-LLZO powder was calcined in a muffle type furnace (Nabertherm Max. Temperature 1340 °C 11 kW, 400 V, 3 phase) at 1000 °C for 6 hours in an open atmosphere and milled in a mortar mill after calcination.

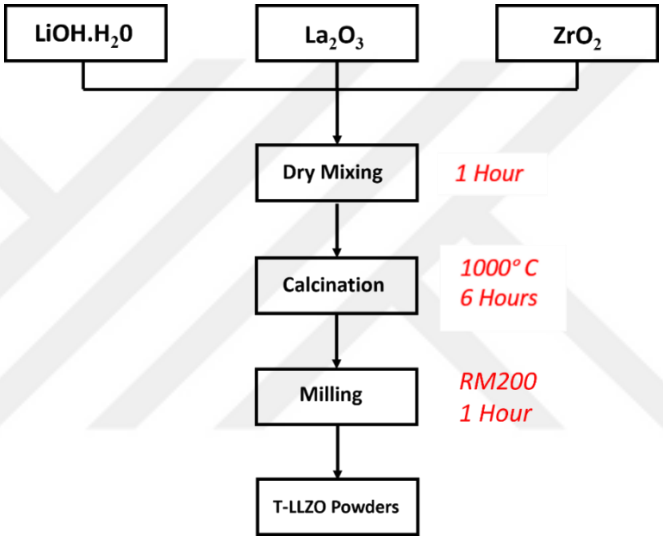

Figure 4.1. *Production scheme of Tetragonal LLZO(T-LLZO) powders.*

Preparation of calcined RMD-LLZO powder: $LiOH.H_2O$ (Alfa Aesar), La_2O_3 (Sigma Aldrich), ZrO_2 (Sigma Aldrich) and red mud powders were mixed in stoichiometric ratios in a mortar mill for 1 hour (Retsch, RM200). The prepared RMD-LLZO powder was calcined in a muffle type furnace (Nabertherm Max. Temperature 1340 °C 11kW, 400V, 3 Phase) at 1000 °C for 6 hours in an open atmosphere and milled in a mortar mill after calcination. 0.08 molar red mud powder was used for the production of RMD-LLZO. In previous studies at Eskişehir technical university, it was determined that RMD-LLZO prepared by using 0.08 molar red mud powder has high ionic conductivity, provides excessive grain growth and stabilizes the cubic phase [64].

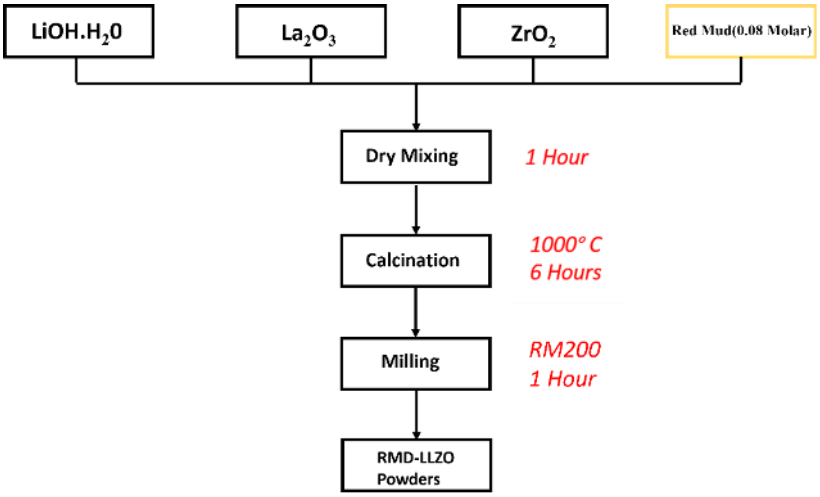

Figure 4.2. *Production scheme of red mud doped LLZO(RMD-LLZO) powders.*

During the experiments, T-LLZO and RMD-LLZO powders produced by these methods were used.

Red mud is a waste material mostly composed of Fe, Al and Si. The percentage of elements it contains is given in table 4.1.

Table 4.1. *XRF data of red mud.*

Elements	wt. %
Fe	35.02
Al	23.38
Si	19.93
Na	10.17
Ca	6.17
Ti	4.97
Others	0.36

Phase analysis of red mud is given in Figure 4.3. In the literature, Fe_2O_3 is used for Fe doping while Al $(OH)_3$ is used for Al doping. Red mud contains Fe_2O_3 used for Fe doping and Al $(OH)_3$ used for Al doping. Therefore, the results can be compared with the literature.

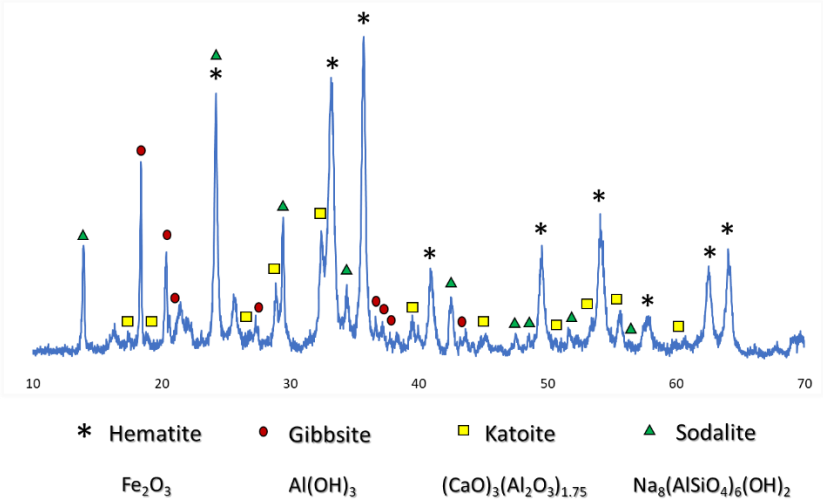

Figure 4.3. *Phase analysis of red mud*

The flow chart including the production steps of T-LLZO with RMD-LLZO addition is given in Figure 4.4. In studies conducted in line with this scheme, the effect of RMD-LLZO doping on T-LLZO was investigated.

The samples were produced by conventional solid state reaction, which offers advantages such as simple preparation process, low cost and high yield. Two separate mixtures were prepared. 1. Mixture (T-LLZO): $LiOH.H_2O$ (Alfa Aesar), La_2O_3 (Sigma Aldrich), ZrO_2 (Sigma Aldrich) powders in stoichiometric ratios and high purity were mixed in a mortar mill for 1 hour (Retsch, RM200). 2. Mixture (RMD-LLZO): $LiOH.H_2O$ (Alfa Aesar), La_2O_3 (Sigma Aldrich), ZrO_2 (Sigma Aldrich) and red mud powders in stoichiometric ratios and high purity were mixed in a mortar mill for 1 hour (Retsch, RM200). An excess of 15% lithium is added to the stoichiometry to compensate for losses of the element lithium (Li) due to high temperature heat treatments. (Also, the effect of excess lithium added in later experiments was investigated.) $LiOH.H_2O$, La_2O_3 and red mud powders were dried before calcination. The mixtures were calcined in a muffle type furnace (Nabertherm Max. Temperature 1340 °C 11kW, 400V, 3 Phase) at 1000 °C in an open atmosphere for 6 hours. After calcination, each mixture was milled separately in a mortar mill for 1 hour in order to remove the segregations caused by the melting phases in the mixtures and to eliminate grain growth. In order to form pellets from the obtained mixtures, 1.5 grams of pellets from the powders in various proportions were first formed by the dry press method and then by the cold isostatic process (CIP-Stansted Fluid Power

Ltd) method at 300 MPa pressure for 5 minutes. The obtained pellets were sintered in an atmospheric environment at 1100 °C, 1150 °C and 1200 °C, respectively, in a muffle type furnace (Nabertherm Max. Temperature 1340 °C 11kW, 400V, 3 Phase) by applying the powder bed method for 12 hours.

RMD-LLZO was sifted while the experiment was repeated. It was observed that there were small grain size powders sifted via sieve and large grain size powders that were not sifted via sieve. In addition to the study, T-LLZO with RMD-LLZO addition samples were prepared by using RMD-LLZO powders that were sifted and whose grain size were smaller than 63 microns.

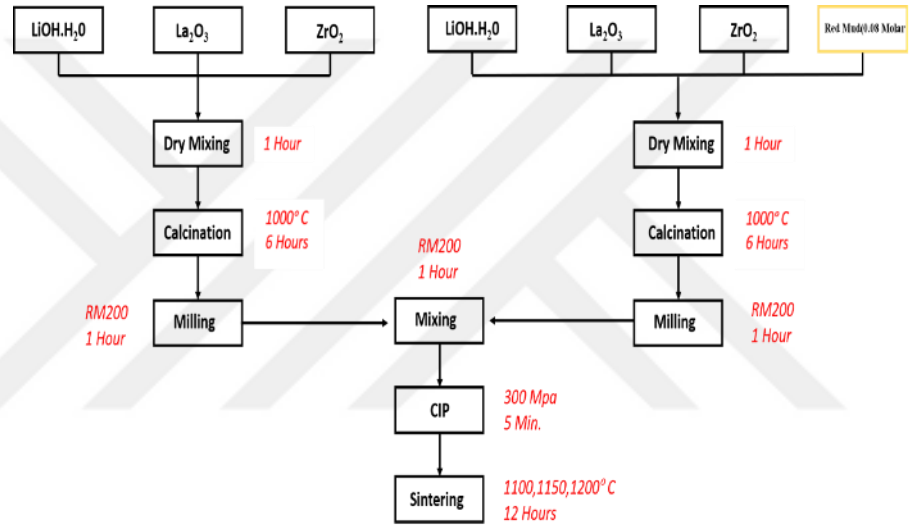

Figure 4.4. *Production scheme of T-LLZO samples with added RMD-LLZO.*

In the next study, calcined tetragonal LLZO powder was milled by ball milling for 1,2,4 and 8 hours. Samples were prepared from powders with reduced grain size. The effect of grain size on densification and ionic conductivity was investigated. The production scheme of the experiment is given in Figure 4.5.

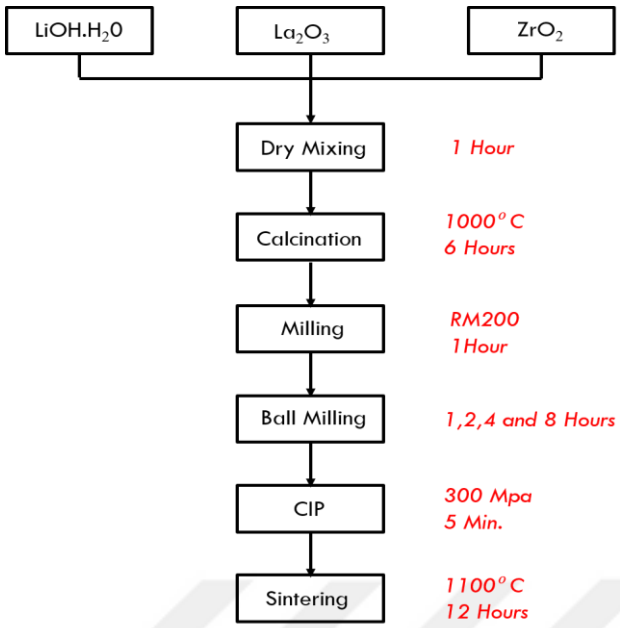

Figure 4.5. *Production scheme of T-LLZO samples milled at different times.*

In the next study, the effect of RMD-LLZO doping was investigated in addition to the effect of milling time. Samples were prepared using T-LLZO with RMD-LLZO addition powders that were milled in a ball mill for 2, 4 and 8 hours. The production scheme of the experiment is given in Figure 4.6.

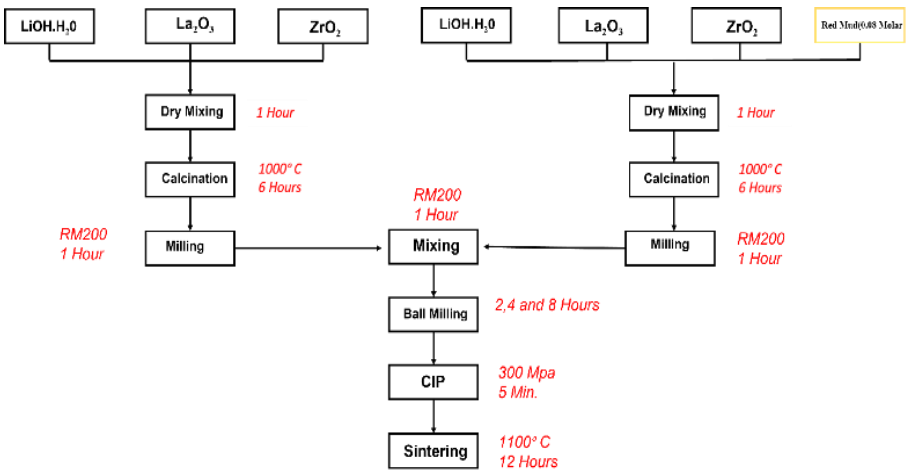

Figure 4.6. *Production scheme of the study examining the effect of milling time and RMD-LLZO doping.*

In the next study, the mixture of T-LLZO with RMD-LLZO addition was calcined in pellet form, unlike other studies. The effect of compaction before calcination was investigated. The production scheme of the experiment is given in Figure 4.7.

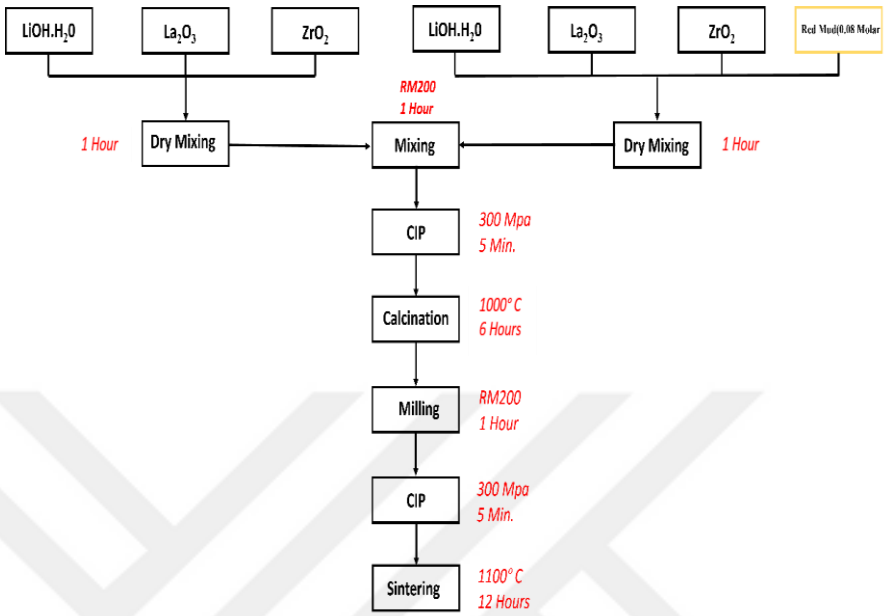

Figure 4.7. *Production scheme of the study in which the effect of the compression process applied before calcination was examined.*

In the next study, after calcination, direct sintering process was started without cooling. This process can also be called two-step sintering. The difference of this study from the previous study is that after calcination the pellets were not milled. The powders, stoichiometry and the furnace used were same. The production scheme of the study, which examines the effect of sintering without waiting for its cooling after calcination, is given in Figure 4.8.

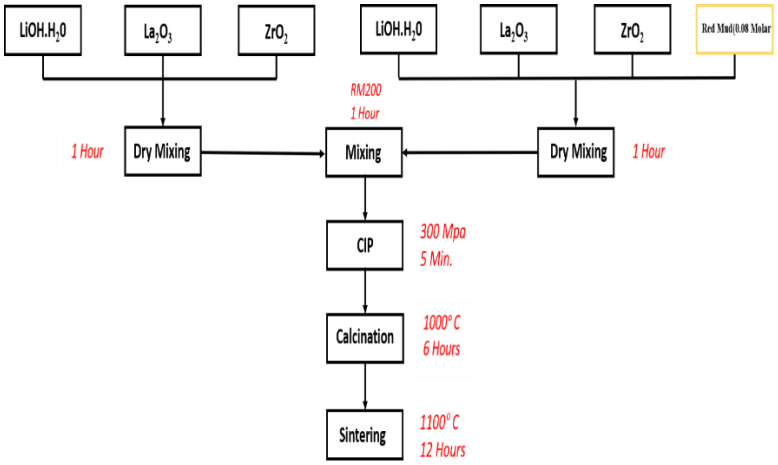

Figure 4.8. *Production scheme of the study examining the effect of sintering without cooling after calcination.*

4.1. Characterization Processes

LLZO samples; It was characterized by X-ray diffraction (XRD), scanning electron microscopy (SEM), archimedes density measurement and AC impedance analysis.

4.1.1. Sample preparation for characterization processes

Residues on the sintered samples were cleaned using 400,600,800,1200,2400 grit sandpaper and then both surfaces of the samples were polished. Afterwards, the samples were broken for SEM analysis and the broken surfaces were gold/palladium coated. For XRD analysis, the samples were ground in a mortar and XRD analyzes were taken as powder.

4.1.2. X-ray diffraction (XRD) analysis

X-ray diffraction (XRD) analysis was used to obtain information about the phases developed in the microstructures of the undoped and doped LLZO samples produced using the conventional solid-state reaction. Phase analysis was performed with the Rigaku Miniflex 600 x-ray diffraction (XRD) instrument. XRD analyzes were performed between 15 and 55° (2Θ), 40 kV acceleration voltage, 15 mA current, 1°/min scanning speed and 0.02 step size.

4.1.3. Microstructure analysis

Microstructures, phase characteristics, surface morphologies and grain size distributions of the produced Undoped and doped LLZO samples were investigated by Phenom ProX and Zeiss SUPRA 50 VP scanning electron microscope (SEM). It was

investigated in backscattered electron (BSE) and secondary electron (SE) modes at an acceleration voltage of 15 kV.

4.1.4. Ionic Conductivity Measurements

Gamry Reference 600 potentiostat/galvanostat system was used for the determination of ionic conductivity of sintered samples. Before measuring the ionic conductivities, the samples were coated with a gold/palladium electrode. Ionic conductivity values were measured in 50mV alternating current amplitude and frequency range of 10^6-10^1 Hz. Ionic conductivity values were calculated from the resulting Nyquist diagram.

4.1.5. Density measurement

Density measurement was determined by immersing the samples in isopropyl alcohol (liquid) according to Archimedean density measurement principle and images obtained from SEM analysis. The typical microstructure of LLZO contains a significant number of closed pores. During the application of the Archimedean method, the samples immersed in the liquid cannot be wetted due to the presence of closed porosity. Therefore, SEM analyzes were accepted as the main criterion for density measurement.

5. RESULTS AND DISCUSSION

5.1. Effect of RMD-LLZO Addition and Sintering Temperature on the T-LLZO

5.1.1. SE and BSE images

BSE images of T-LLZO(a) and RMD-LLZO(b) are given in Figure 5.1. According to the images, the grains did not even make a neck in the sample produced from T-LLZO powders. It is seen that sintering is insufficient, the reason is that 12 hours was not enough for sintering at 1100 ºC. The image of RMD-LLZO shows significant grain growth. When these samples prepared under the same conditions and sintered at the same temperature are compared, they show the effect of the red mud additive used to promote sintering.

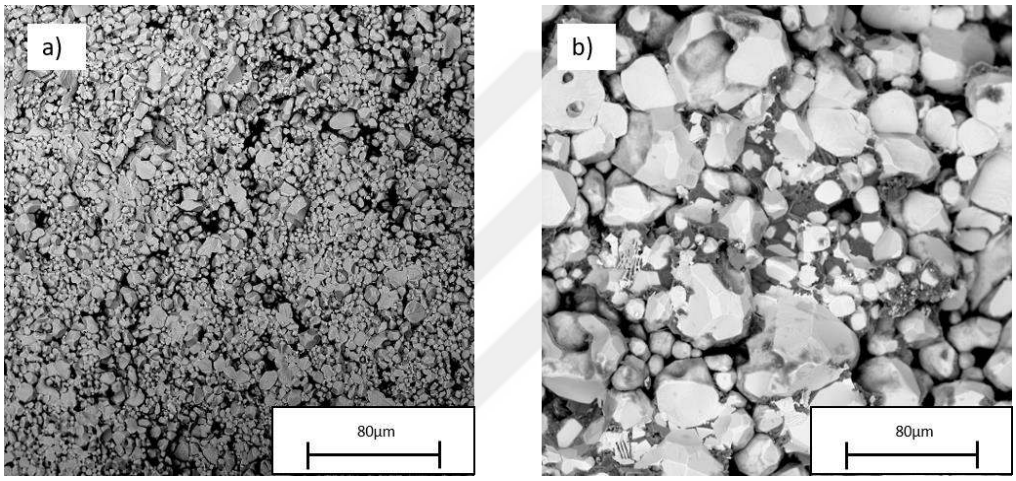

Figure 5.1. *T-LLZO(a) and RMD-LLZO(b) BSE images.*

The SE and BSE images of the samples with 5, 10 and 15 % RMD-LLZO added to T-LLZO are given in Figure 5.2. As the amount of RMD-LLZO added to T-LLZO increases, the number of closed pores and the size of closed pores decrease. There is grain growth up to a certain point, but after this point, due to the LLZO structure, the closed pores inside merge and grain separation occur at the last stage. This means that small grains are formed. Since this situation causes the formation of gaps, it affects the sintering negatively and reduces the ionic conductivity. This is due to T-LLZO with RMD-LLZO addition used to support sintering. Although we do not increase the temperature, the T-LLZO with added RMD-LLZO continues to be sintering. This situation, which is observed by increasing the sintering temperature of LLZO, can also be observed by the doping effect. The graphic representation of this situation is given in Figure 5.3.

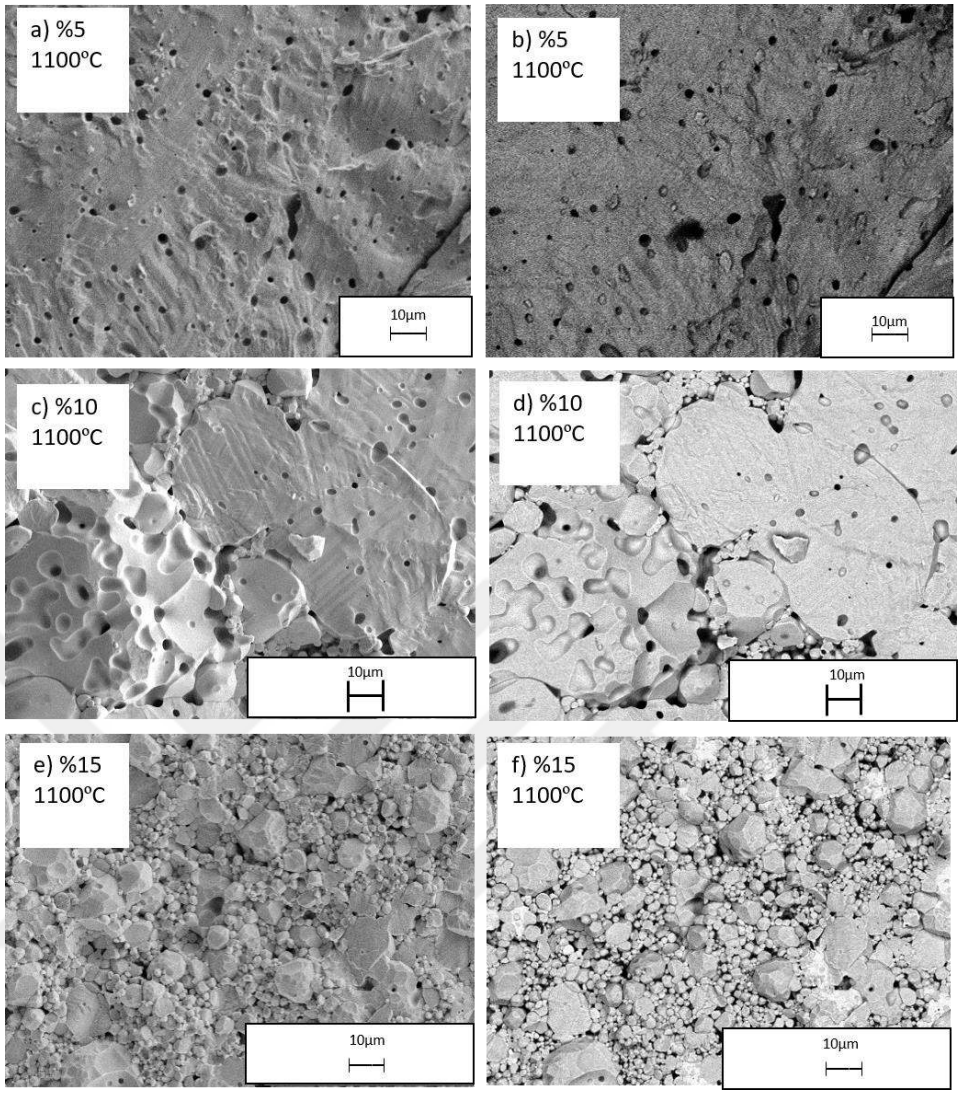

Figure 5.2. *SE and BSE images of Tetragonal LLZO samples with 5,10,15% wt added RMD-LLZO. SE image of T-LLZO with 5% RMD-LLZO added (a), BSE image of T-LLZO with 5% RMD-LLZO added (b), SE image of T-LLZO with 10% RMD-LLZO added (c), BSE image of T-LLZO with 10% RMD-LLZO added (d), SE image of T-LLZO with 15% RMD-LLZO added (e), BSE image of T-LLZO with 15% RMD-LLZO added (f).*

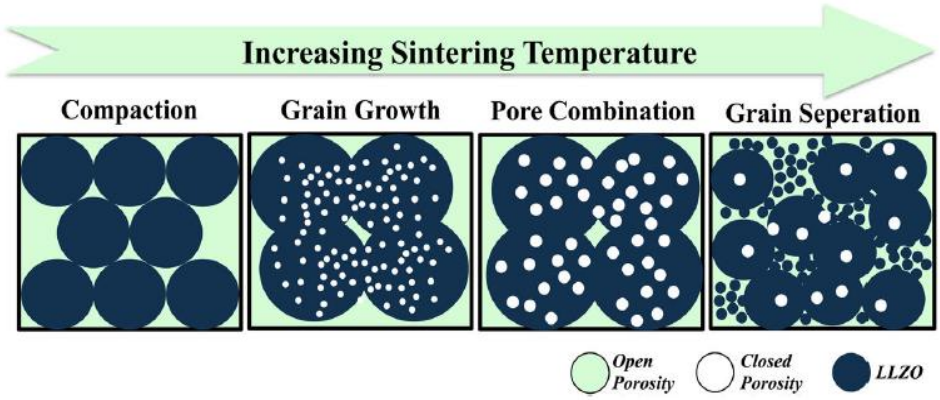

Figure 5.3. *LLZO densification model as a function of temperature [63].*

The SE and BSE images of the T-LLZO with RMD-LLZO addition prepared using the sifted RMD-LLZO powders are given in Figure 5.4. The grain sifted via the sieve are small. Powders with small grain sizes react more easily during the sintering because their activation energy is lower. A better sintering can be achieved because the diffusion mechanisms will work faster. It can be assumed that as the amount of RMD-LLZO increases, there is more incentive to sintering. As mentioned in the previous example, because of the structure of LLZO, small grains are formed as a result of the combination of closed pores inside, which leads to grain separation. It can be clearly seen in samples with 10% and 15% addition. Crater formation is observed in 10% and 15% added samples. The crater formation indicates that the grains came out of there, and the diameter of the craters gives the approximate grain size. It is seen that the craters are larger in the sample with 15% addition, which indicates that the grains have grown even larger in this sample.

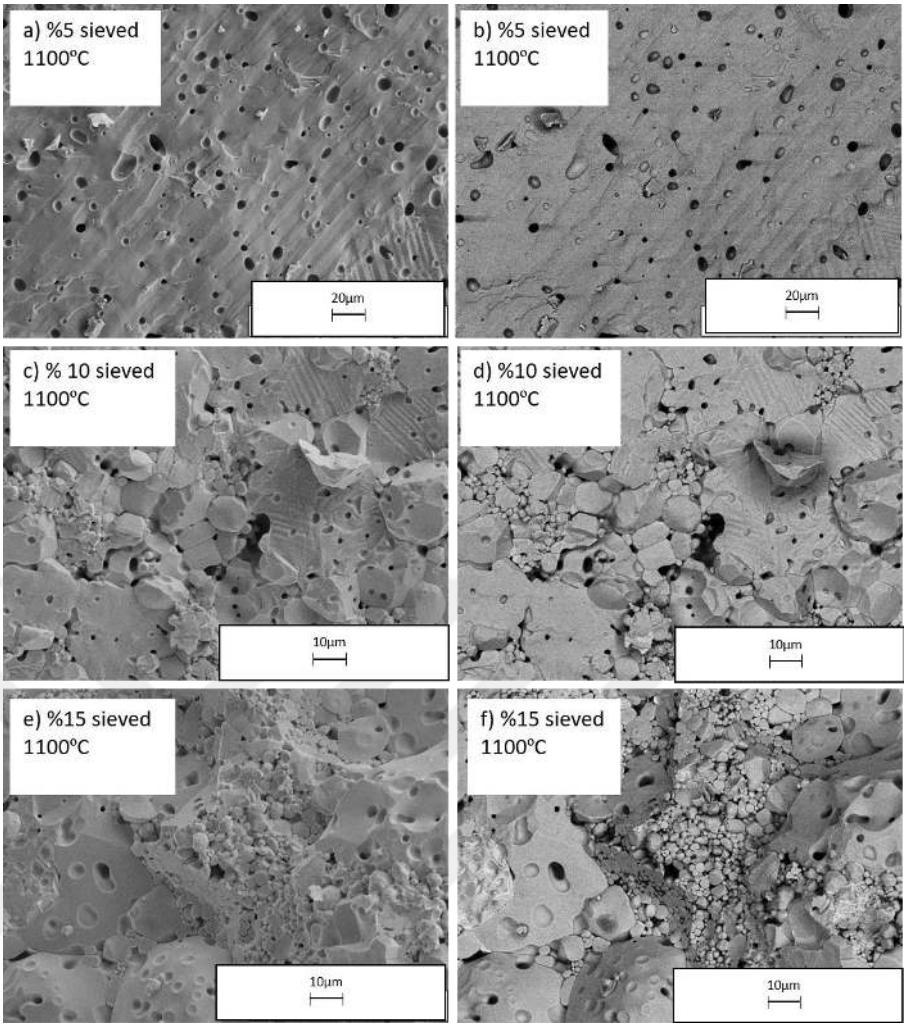

Figure 5.4. *SE and BSE images of T- LLZO samples containing 5,10,15% by weight sifted RMD-LLZO. SE image of T-LLZO with 5% RMD-LLZO added (a), BSE image of T-LLZO with 5% RMD-LLZO added (b), SE image of T-LLZO with 10% RMD-LLZO added (c), BSE image of T-LLZO with 10% RMD-LLZO added (d), SE image of T-LLZO with 15% RMD-LLZO added (e), BSE image of T-LLZO with 15% RMD-LLZO added (f).*

SE and BSE images of T-LLZO added with RMD-LLZO samples sintered at 1150 ºC and 1200 ºC are given in Figure 5.5 and 5.6. In addition to the added cubic powder (T-LLZO powder added with RMD-LLZO), the increase in sintering temperature further encouraged sintering. Excessive formation of closed pores was observed in the samples due to the increase in sintering temperature.

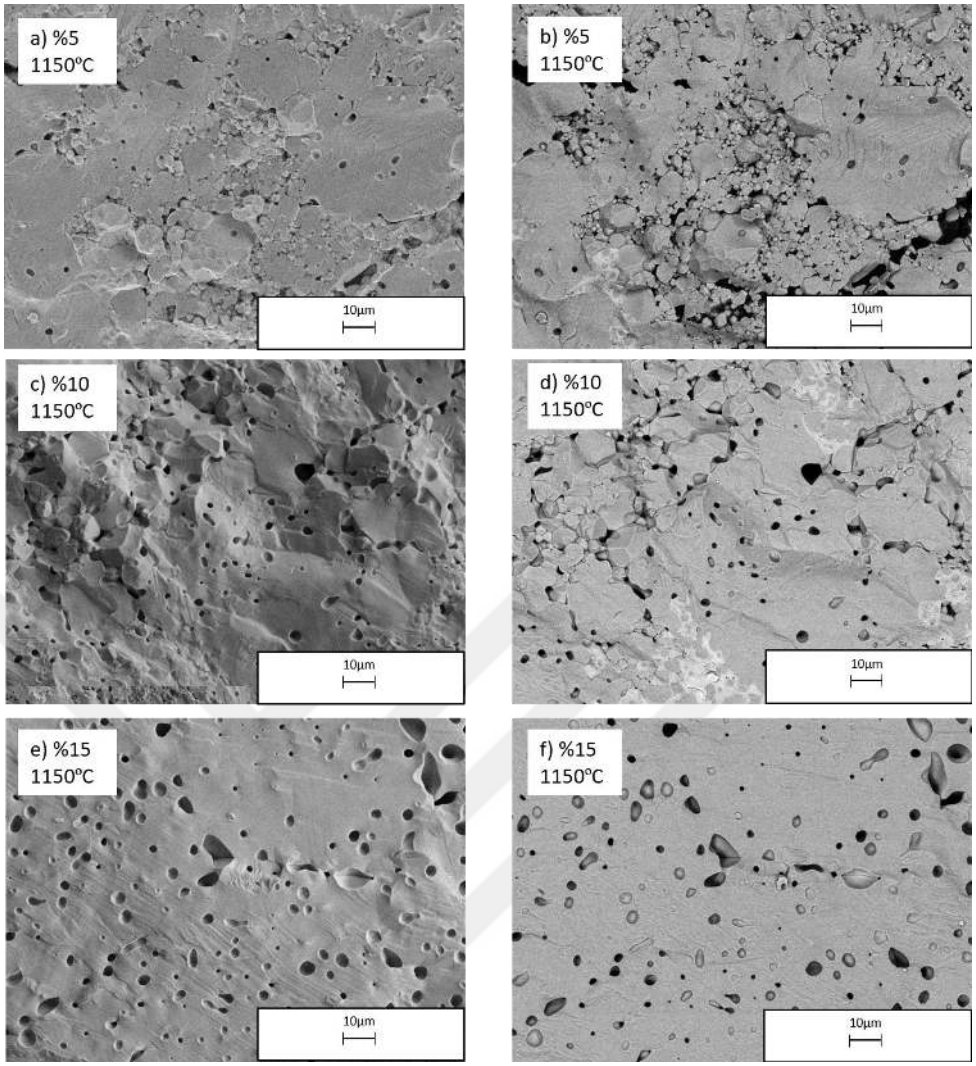

Figure 5.5. *SE and BSE images of Tetragonal LLZO samples with 5,10,15% wt addition RMD-LLZO. SE image of T-LLZO with 5% RMD-LLZO addition at 1150 ºC (a), BSE image of T-LLZO with 5% RMD-LLZO addition at 1150 ºC (b), SE image of T-LLZO with 10% RMD-LLZO addition at 1150 ºC (c), BSE image of T-LLZO with 10% RMD-LLZO addition at 1150 ºC (d), SE image of T-LLZO with 15% RMD-LLZO addition at 1150 ºC (e), BSE image of T-LLZO with 15% RMD-LLZO addition at 1150 ºC (f).*

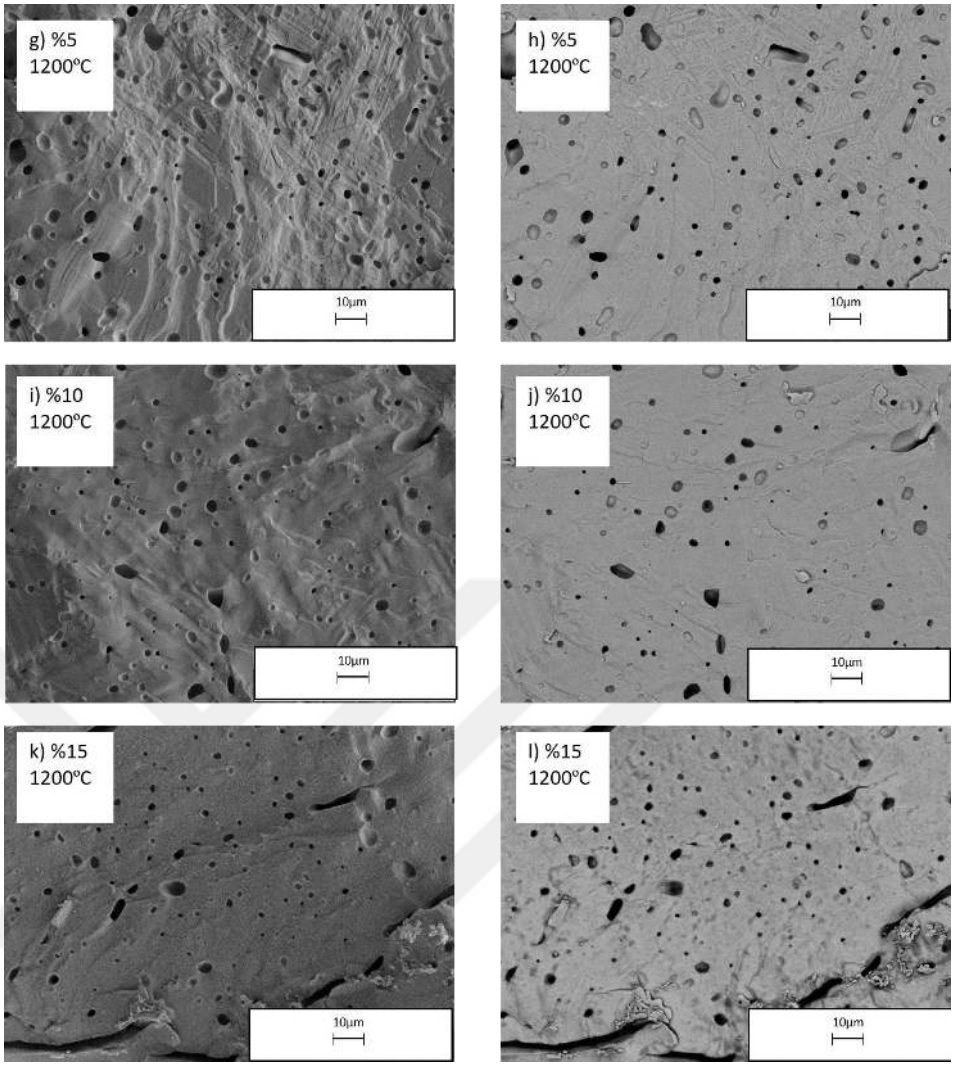

Figure 5.6. *SE and BSE images of Tetragonal LLZO samples with 5,10,15% wt addition RMD-LLZO. SE image of T-LLZO with 5% RMD-LLZO addition at 1200 ℃ (g), BSE image of T-LLZO with 5% RMD-LLZO addition at 1200 ℃ (h), SE image of T-LLZO with 10% RMD-LLZO addition at 1200 ℃ (i), BSE image of T-LLZO with 10% RMD-LLZO addition at 1200 ℃ (j), SE image of T-LLZO with 15% RMD-LLZO addition at 1200 ℃ (k), BSE image of T-LLZO with 15% RMD-LLZO addition at 1200 ℃ (l).*

5.1.2. Phase analysis

The XRD patterns of T-LLZO and RMD-LLZO after calcination are given in Figure 5.7. Compared with the Tetragonal and Cubic LLZO XRD patterns in Figure 5.5, T-LLZO still remained in the tetragonal structure after calcination. On the other hand, RMD-LLZO turned into a cubic structure even after calcination.

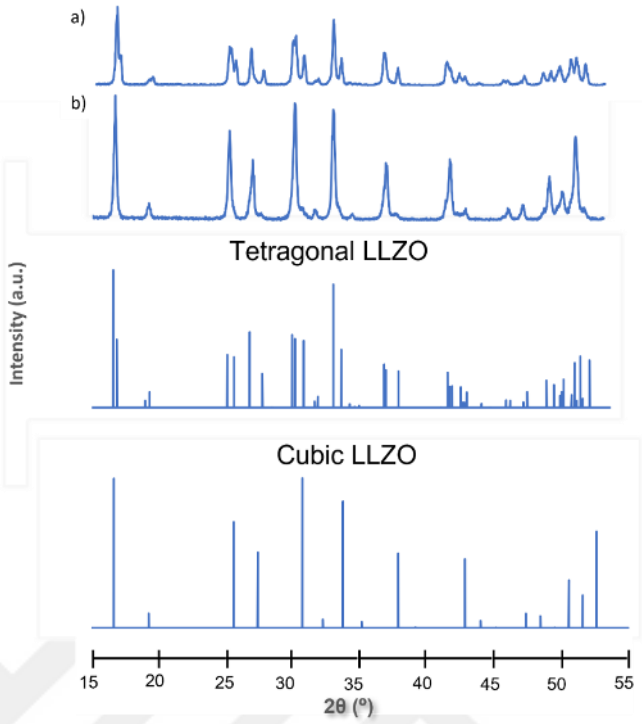

Figure 5.7. *Phase analysis of T-LLZO(a) and RMD-LLZO(b) after calcination*

The XRD patterns of the samples after sintering are given in Figure 5.7. After sintering at 1100 ºC for 12 hours, it was observed that all samples turned into cubic structures. Impurity phases are observed in samples of T-LLZO (c) with 5% RMD-LLZO addition, 10% T-LLZO with RMD-LLZO addition (d), and 15% T-LLZO with RMD-LLZO addition (e). No impurity phases are seen in the samples of T-LLZO with 5% sieved RMD-LLZO (f) and T-LLZO with 10% sieved RMD-LLZO (g). However, these impurity phases are seen in the T-LLZO with 15% sieved RMD-LLZO addition (h). This is because the RMD-LLZO powders used in the preparation of samples (c), (d) and (e) were not sieved. Since there are particles with larger grain size in powders that are not sieved, these large particles enter the reaction more difficult during sintering and can remain undissolved in the structure. Since these particles do not diffuse, impurity phases are observed in the XRD analysis. In the samples (f) and (g) prepared with sieved RMD-LLZO powders, impurity phases are not observed since there are no particles with large grain size. However, as the amount of added RMD-LLZO increases, the impurity seen in sample (h) reappears.

The XRD patterns of the samples sintered at 1150 ºC and 1200 ºC after sintering are given in Figure 5.8. It can be seen from the XRD patterns that all the samples are in cubic structure. There are impurities observed in the structure. These are segregated and incompletely combined phases.

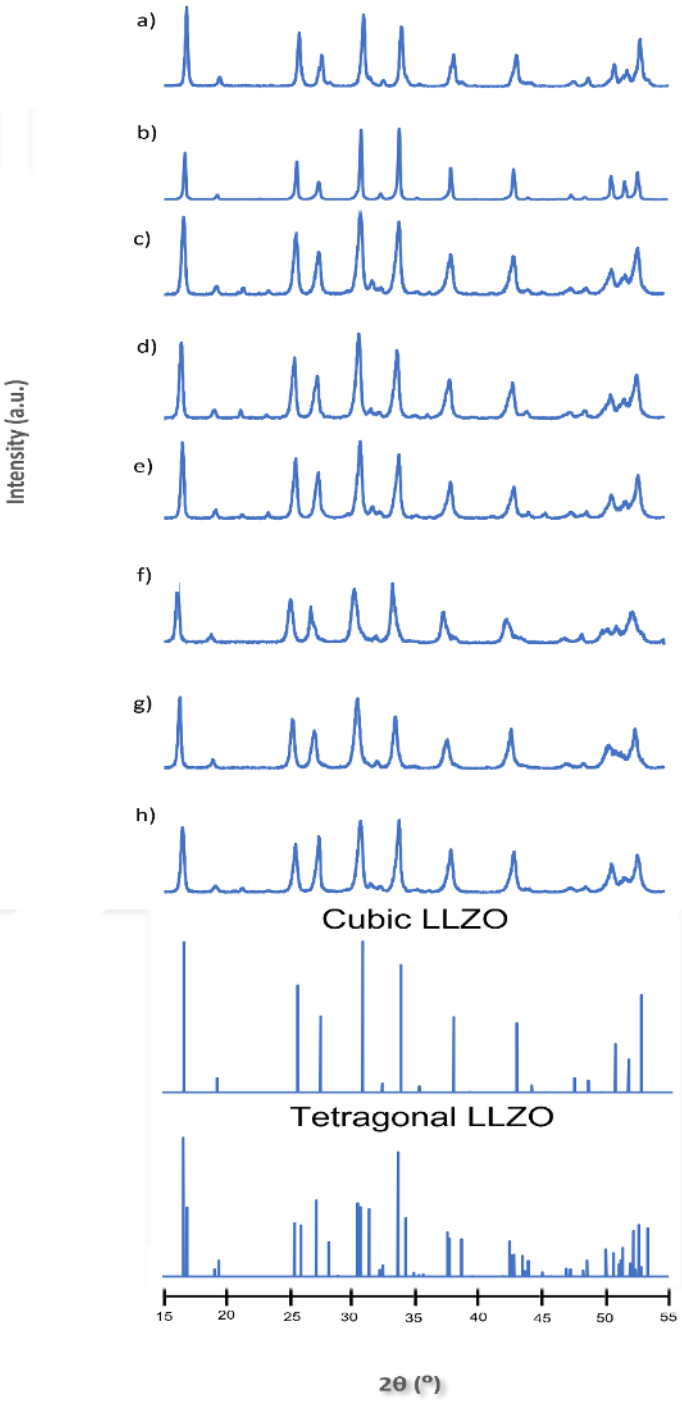

Figure 5.8. *The XRD patterns of the samples after sintering. T-LLZO at 1100 ºC (a), RMD-LLZO at 1100 ºC (b), T-LLZO with 5% RMD-LLZO addition at 1100 ºC (c), T-LLZO with 10%RMD-LLZO addition at 1100 ºC (d), T-LLZO with 15% RMD-LLZO addition at 1100 ºC (e), T-LLZO with 5% sifted RMD-LLZO addition at 1100 ºC (f), T-LLZO with 10% sifted RMD-LLZO addition at 1100 ºC (g), T-LLZO with 15% sifted RMD-LLZO addition at 1100 ºC (h).*

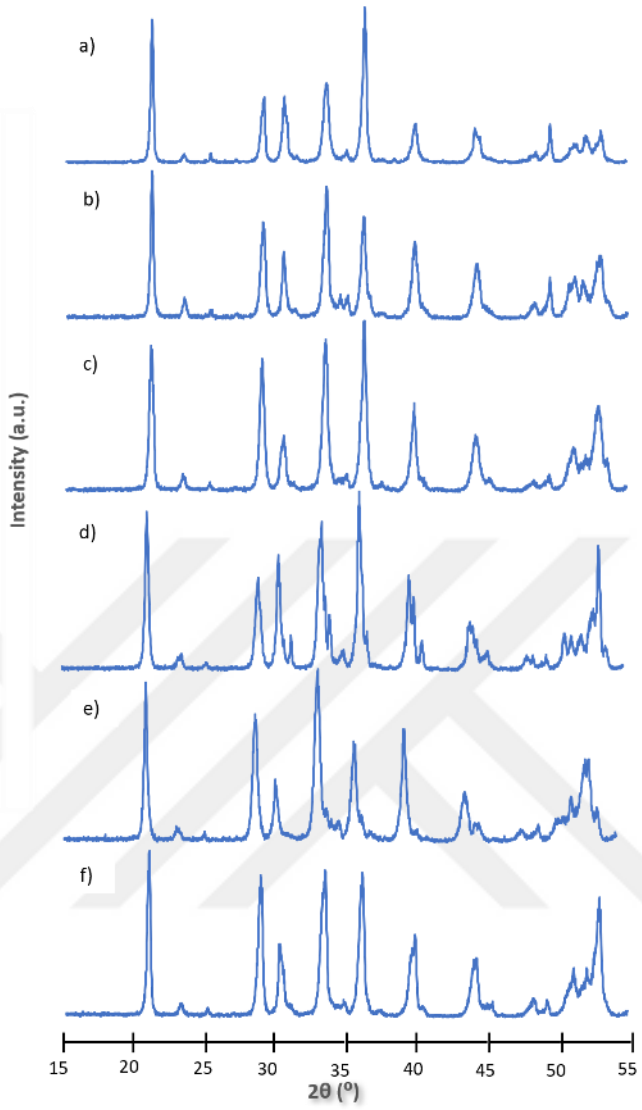

Figure 5.9. *The XRD patterns of the samples after sintering. T-LLZO with 5%RMD-LLZO addition at 1150 ℃ (a), T-LLZO with 10% RMD-LLZO addition at 1150 ℃ (b), T-LLZO with 15% RMD-LLZO addition at 1150 ℃ (c), T-LLZO with 5% RMD-LLZO addition at 1200 ℃ (d), T-LLZO with 10% RMD-LLZO addition at 1200 ℃ (e), 15% T-LLZO with RMD-LLZO addition at 1200 ℃ (f).*

5.1.3. Effect of RMD-LLZO addition on ionic conductivity

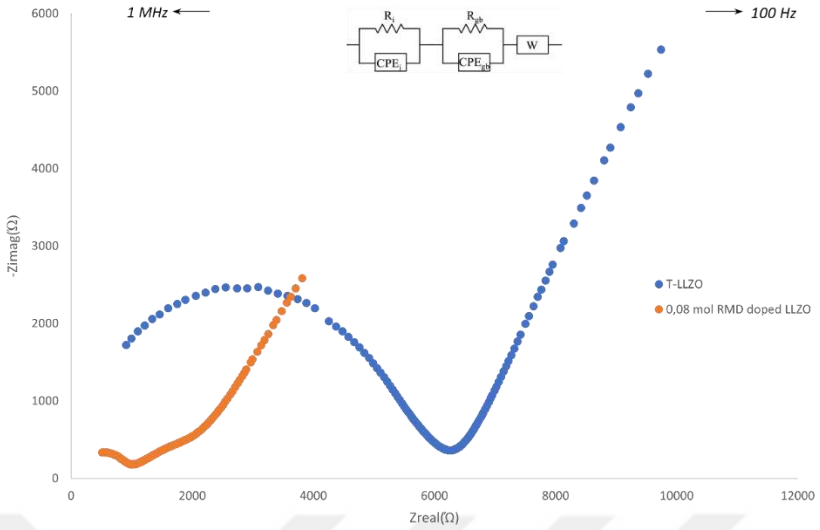

Figure 5.10. *Nyquist plots of T-LLZO and RMD-LLZO*

Figure 5.10. shows Nyquist plots of pellets sintered at 1100 ºC of T-LLZO and RMD-LLZO samples. The change in ionic conductivity was observed with the effect of doping. In the potentiostat graph, the first semicircle represents the bulk conductivity. The second semicircle indicates the grain boundary resistance. The third semicircle represents the ion-blocking (Li) electrode potential. It is accepted that with increased bulk conductivity and reduced grain boundary resistance, the LLZO internal resistance should be reduced. It is observed that the diameter of the semicircle decreases with the addition of red mud. The addition of red mud increased the bulk conductivity. Ionic conductivity values were calculated with the data taken from the graph and considering the geometric factors. As a result of the calculations, the ionic conductivity of the T-LLZO sample is 4.1×10^{-5} S/cm and the ionic conductivity of the RMD-LLZO sample is 9×10^{-5} S/cm.

Figure 5.11. shows Nyquist plots of pellets of T-LLZO with RMD-LLZO added samples sintered at 1100 ºC.

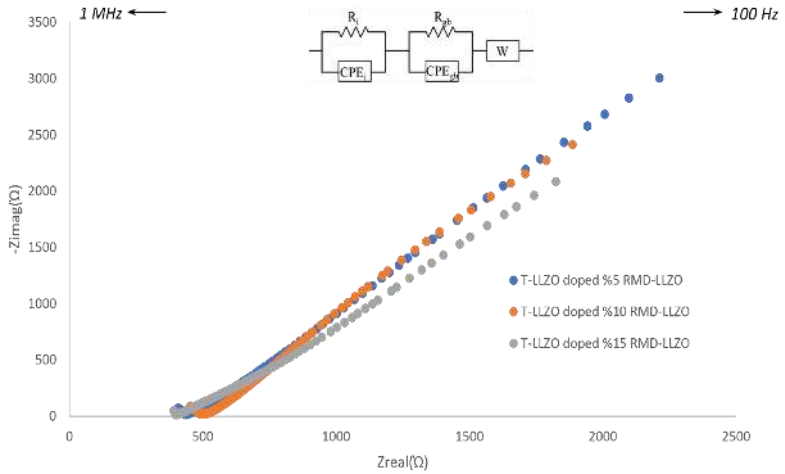

Figure 5.11. *Nyquist plots of T-LLZO samples with 5.10 and 15% RMD-LLZO at 1100 ºC.*

Measured ionic conductivity values are given in Figure 5.12. The highest ionic conductivity was obtained by adding 10% RMD-LLZO at 1100 ºC. As seen in the graph, there was an increase in ionic conductivity because the semicircle was not clear. The lack of clarity of the semicircle indicates that the grain boundary resistance is negligible compared to the grain resistance.

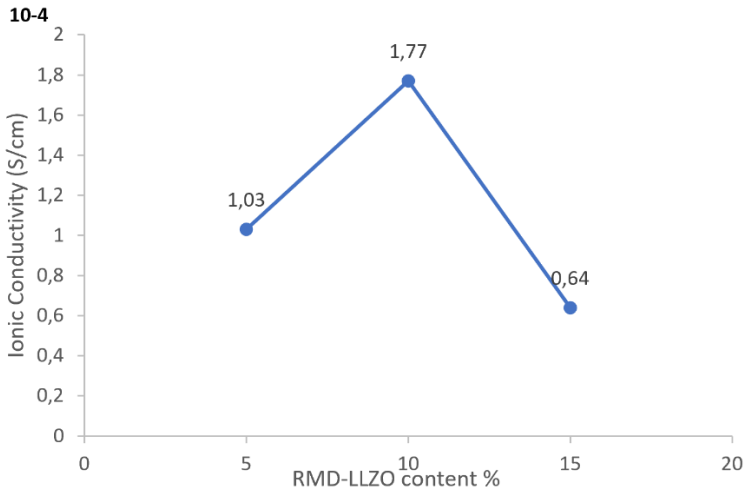

Figure 5.12. *Measured conductivities for all 5.10 and 15% RMD-LLZO additions at 1100 ºC.*

Figure 5.13. shows Nyquist plots of pellets of sieved T-LLZO with RMD-LLZO added samples sintered at 1100 ºC.

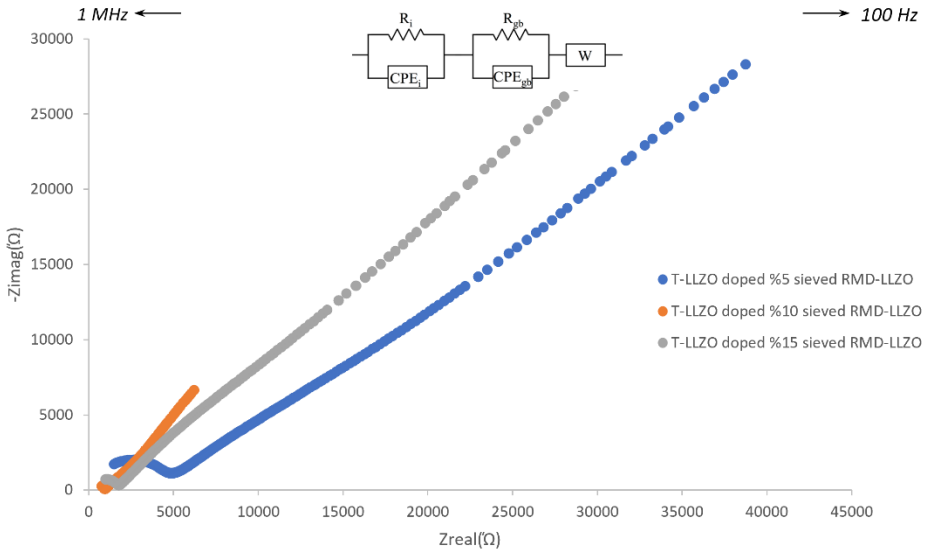

Figure 5.13. *Nyquist plots of T-LLZO with 5.10 and 15% sifted RMD-LLZO addition at 1100 ºC.*

Measured ionic conductivity values are given in Figure 5.14. Similar ionic conductivity results were obtained when compared with the unsieved RMD-LLZO additive. The highest ionic conductivity was obtained by adding 10% unsifted RMD-LLZO at 1100 ºC.

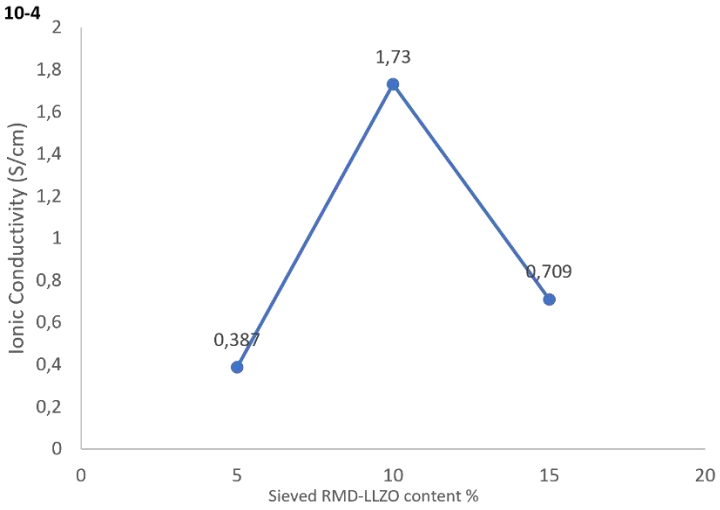

Figure 5.14. *Measured conductivities for all 5.10 and 15% sifted RMD-LLZO additions at 1100 ºC.*

Nyquist plots of T-LLZO with 5.10% and 15% RMD-LLZO addition at 1150 ºC are given in Figure 5.15. Since the semicircle is not clear, it indicates that the grain boundary resistance is negligible compared to the grain resistance.

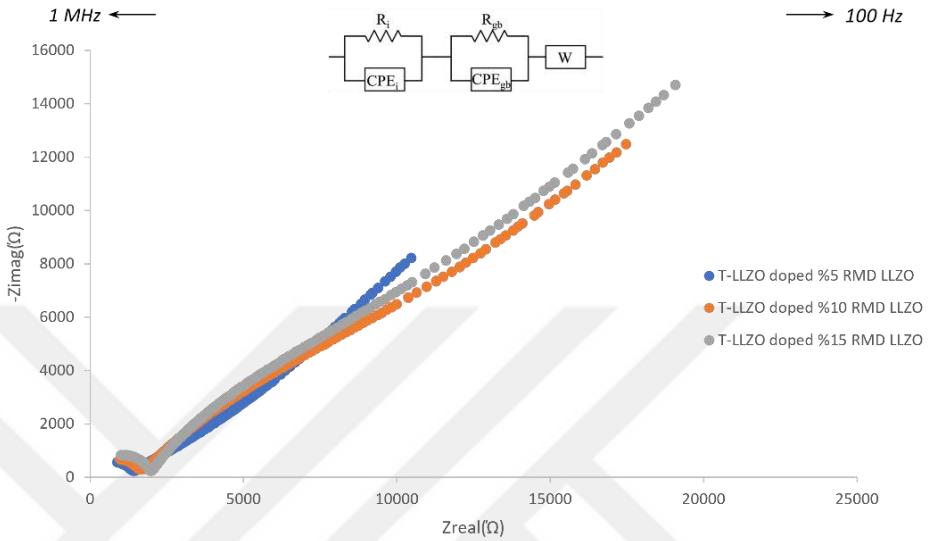

Figure 5.15. *Nyquist plots of T-LLZO samples with 5.10%and 15% RMD-LLZO at 1150 ºC.*

Measured ionic conductivity values are given in Figure 5.16. The increase in temperature and the increase in the amount of RMD-LLZO decreased the ionic conductivity. The decrease in ionic conductivity can also be examined with SEM images. When the SE and BSE images of the samples sintered at 1150 ºC were examined, an increase in the amount of closed porosity was observed as the amount of RMD-LLZO increased. The ionic conductivity values also decrease as the amount of RMD-LLZO increases.

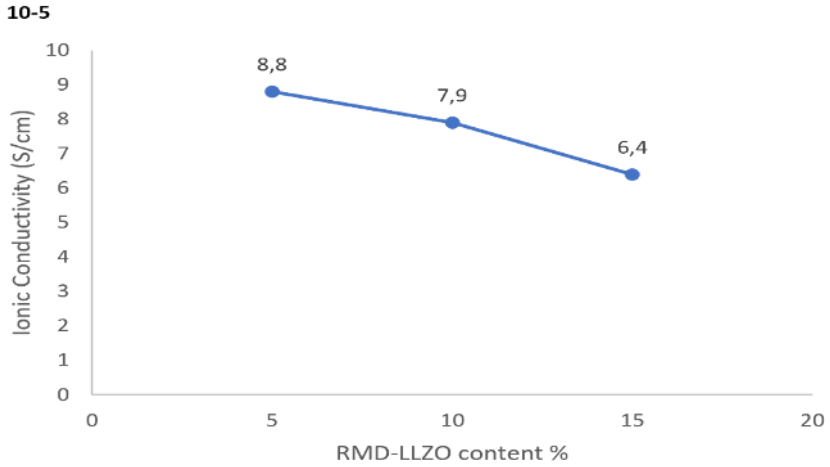

Figure 5.16. *Measured conductivities for all 5.10 and 15% RMD-LLZO additions at 1150 ºC.*

Nyquist plots of T-LLZO with 5.10% and 15% RMD-LLZO addition at 1150 ºC are given in Figure 5.17.

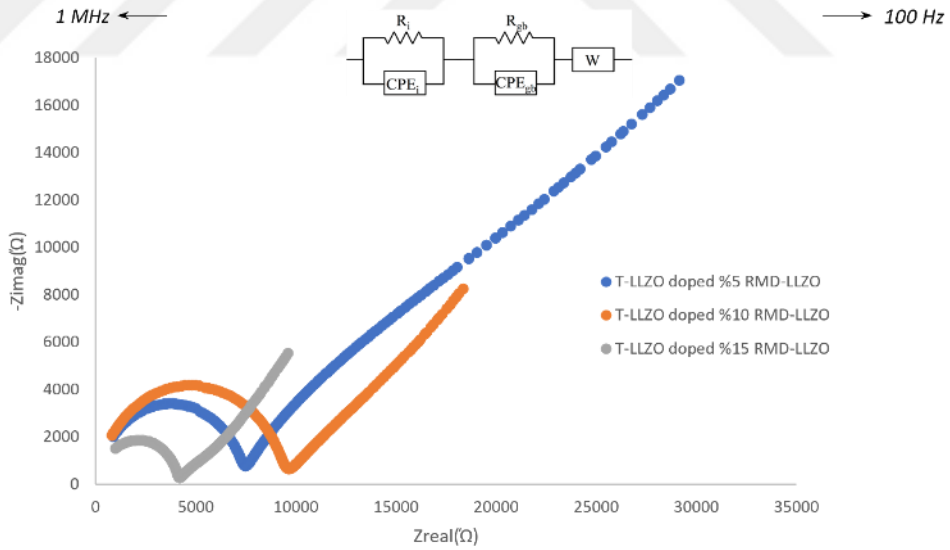

Figure 5.17. *Nyquist plots of T-LLZO with 5.10 and 15% RMD-LLZO addition at 1200 ºC.*

Measured ionic conductivity values of the samples are given in Figure 5.18. Compared to the samples sintered at 1100 ºC and 1150 ºC, much lower ionic conductivity values were obtained. When the SEM images are examined, a large amount of closed

porosity is observed in all of the 5.10 and 15% RMD-LLZO added samples. We are trying to convert the tetragonal phase to cubic phase with the increase in temperature, but the effect of the cubic powder we add, namely RMD-LLZO powder, is seen more clearly at low temperatures. As it approaches 1230 ºC, the transformation temperature, LLZO turns into cubic phase from tetragonal phase. So the 5% RMD-LLZO we add acts as if it is a higher percentage. The reliability of the effect of the added RMD-LLZO powder increases as it moves away from the phase conversion temperature.

Since it is very close to the 1200 ºC transformation temperature, scattering decreases in ionic conductivity values, that is, it becomes more stable. SEM images also show that the samples have similar structures. At 1100 ºC and 1150 ºC, scattering increases in conductivity values. This is proof that the red mud additive shows the catalyst effect more clearly at lower temperatures.

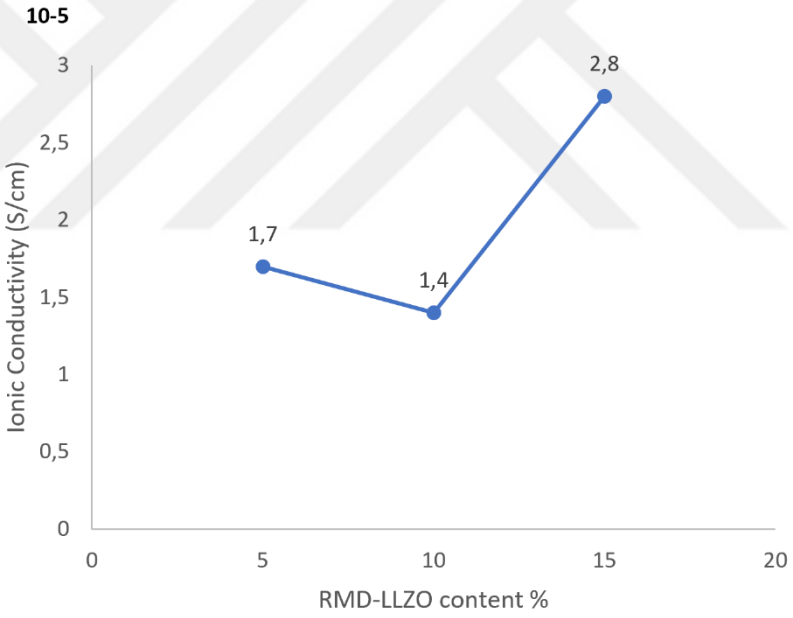

Figure 5.18. *Measured conductivities for all 5.10 and 15% RMD-LLZO additions at 1200 ºC.*

Comparison of the measured ionic conductivity values of the samples sintered at different temperatures and containing different amounts of RMD-LLZO addition is given in Figure 5.19. The highest ionic conductivity value was obtained in T-LLZO with 10% RMD-LLZO added, sintered at 1100 ºC.

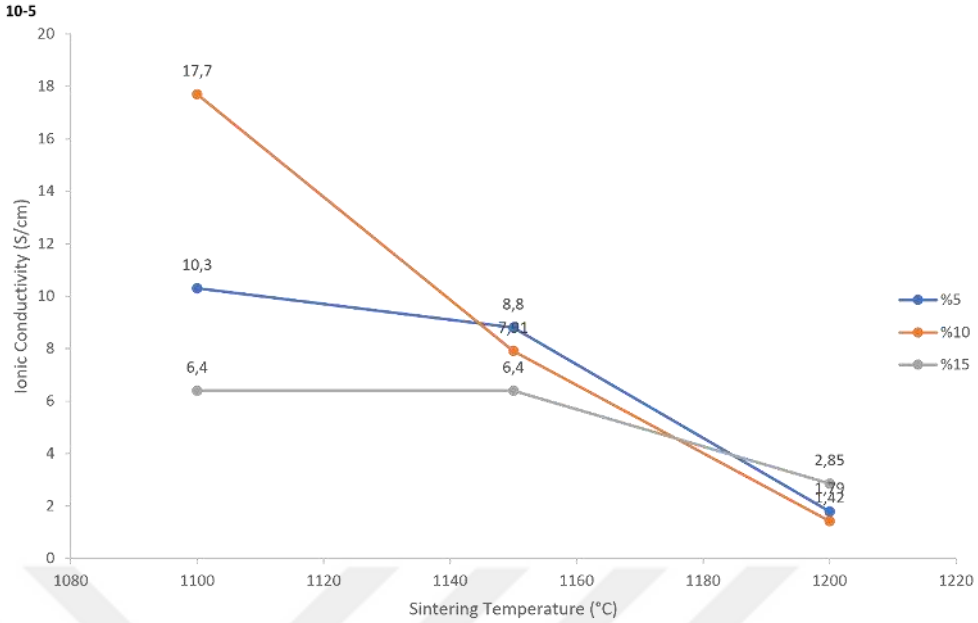

Figure 5.19. *Comparison of measured ionic conductivity values of RMD-LLZO added T-LLZO sintered at 1100 ℃, 1150 ℃ and 1200 ℃.*

5.2. Effect of Milling Time on the Densification of T-LLZO

5.2.1. SE and BSE images

SE and BSE images of samples obtained from T-LLZO powders prepared at different milling times are given in Figure 5.20. It is seen that the grain size is approximately the same in all samples. However, the difference between the ball milled sample and the unmilled sample can be seen. Even after 1 hour of milling, intergranular neck was formed and the sample became denser. While the grains were more spherical in the sample where they were unmilled in the ball mill, intergranular necks were formed in the samples obtained from the milled powder. During the first hours of milling, a very serious grain reduction occurs, but as the milling time increases, it is seen that the grain reduction is limited. In the samples obtained from the powders milled in the ball mill for 4 and 8 hours, at least 2 or 3 grains came together to form a clover shape. However, it was observed that the powder, whose grain size decreased by milling, did not have much effect on the densification of the final product.

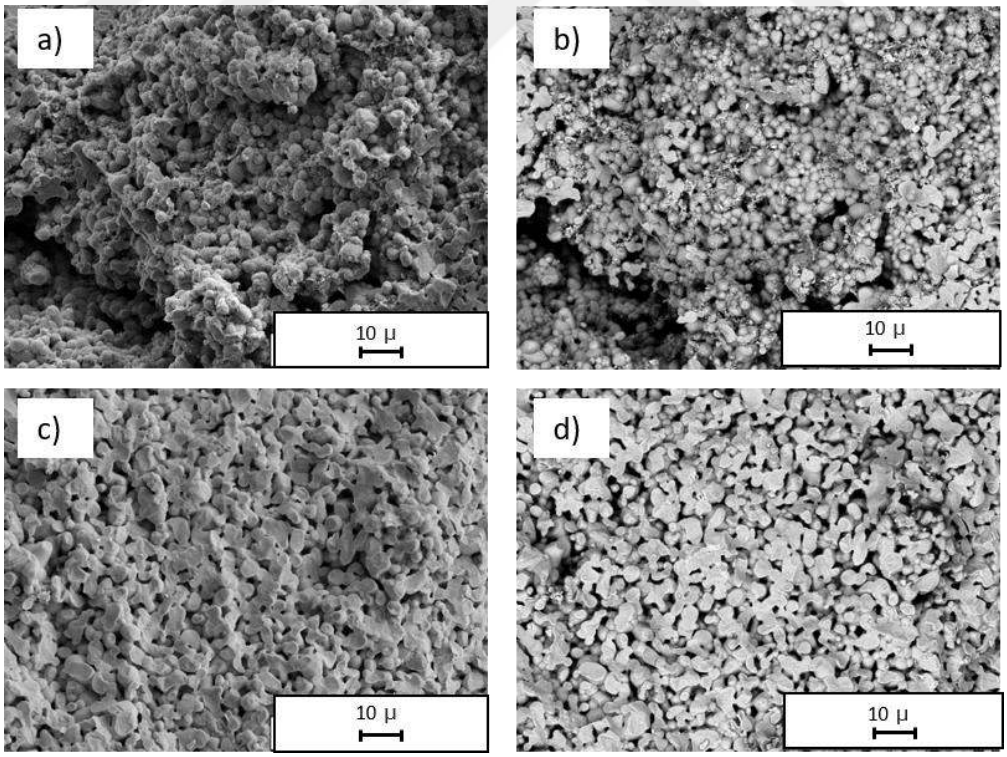

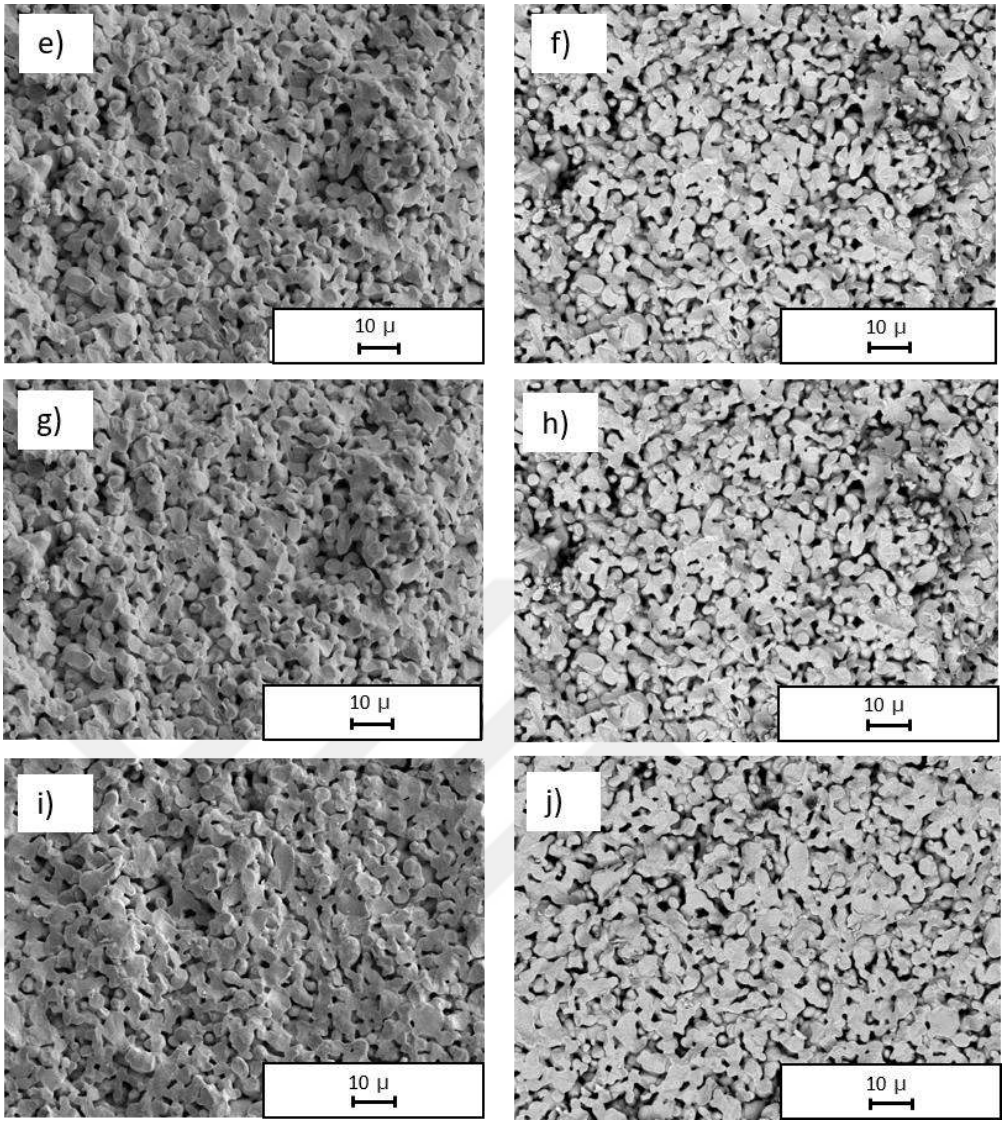

Figure 5.20. *SE and BSE images of samples obtained from T-LLZO powders prepared at different milling times. SE image of sample obtained from powder prepared without ball milling (a), BSE image of sample obtained from powder prepared without ball milling (b), SE image of the sample obtained from the powder prepared in 1 hour ball milling (c), BSE image of the sample obtained from the powder prepared in 1 hour ball milling (d), SE image of the sample obtained from the powder prepared in 2 hours ball milling (e), BSE image of the sample obtained from the powder prepared in 2 hours ball milling (f), SE image of the sample obtained from the powder prepared in 4 hours ball milling (g), BSE image of the sample obtained from the powder prepared in 4 hours ball milling (h), SE image of the sample obtained from the powder prepared in 8 hours ball milling (i), BSE image of the sample obtained from the powder prepared in 8 hours ball milling (j).*

5.2.2. Phase analysis

The XRD patterns of the samples after calcination are given in Figure 5.21. It is observed that all samples are in tetragonal structure.

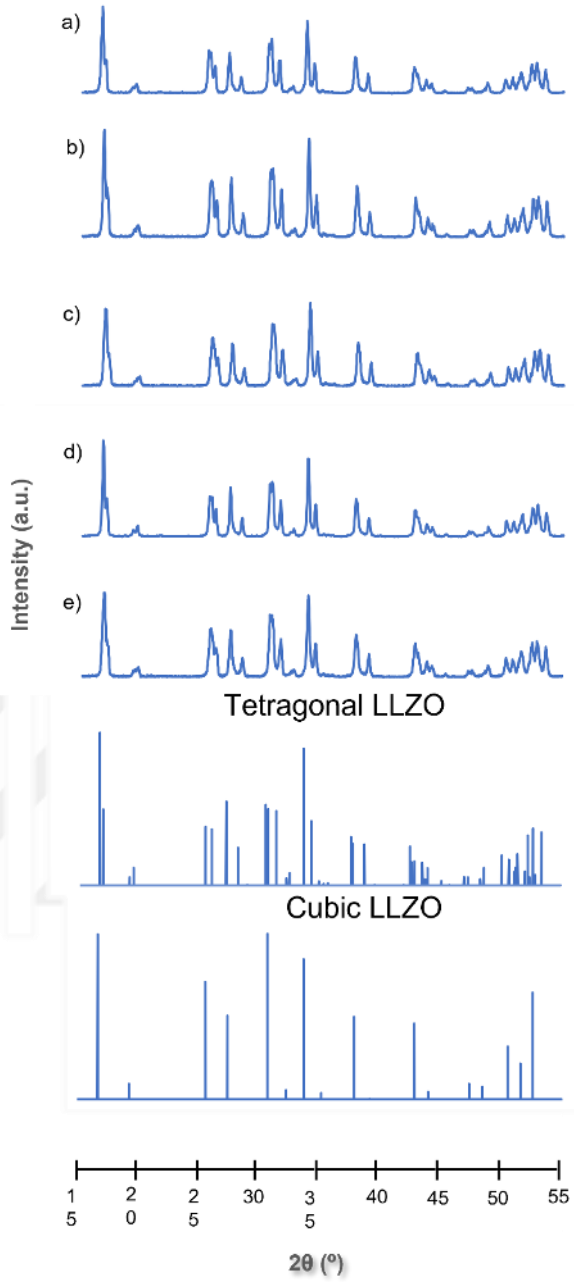

Figure 5.21. *XRD patterns of samples obtained from powders milled at different times after calcination. Sample obtained from powder prepared without ball milling(a), sample obtained from the powder prepared in 1 hour ball milling(b), sample obtained from the powder prepared in 2 hours ball milling(c), sample obtained from the powder prepared in 4 hours ball milling(d), sample obtained from the powder prepared in 8 hours ball milling(e).*

The XRD patterns of the samples after sintering are given in Figure 5.22. It was observed that all samples were in cubic structure. As can be seen from the XRD results, the LLZO peaks can be defined quite well. The cubic and tetragonal phases appear to be

approximately equal in the sample obtained from the powder milled in the ball mill for 4 hours. Experimental error can be assumed as this is seen only in the sample obtained from this powder.

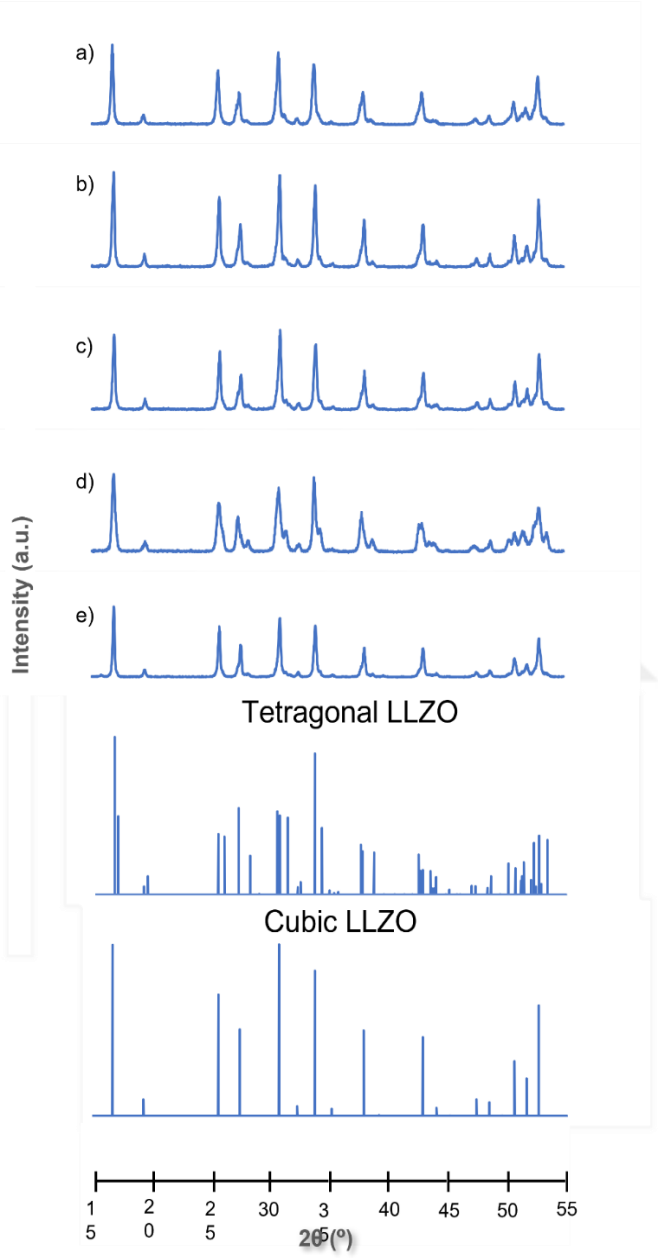

Figure 5.22. *XRD patterns of samples obtained from powders milled at different times after sintering. Sample obtained from powder prepared without ball milling(a), sample obtained from the powder prepared in 1 hour ball milling(b), sample obtained from the powder prepared in 2 hours ball milling(c), sample obtained from the powder prepared in 4 hours ball milling(d), sample obtained from the powder prepared in 8 hours ball milling(e).*

5.2.3. Effect of milling time on ionic conductivity

Nyquist plots of samples obtained from powders milled at different times are given in Figure 5.23.

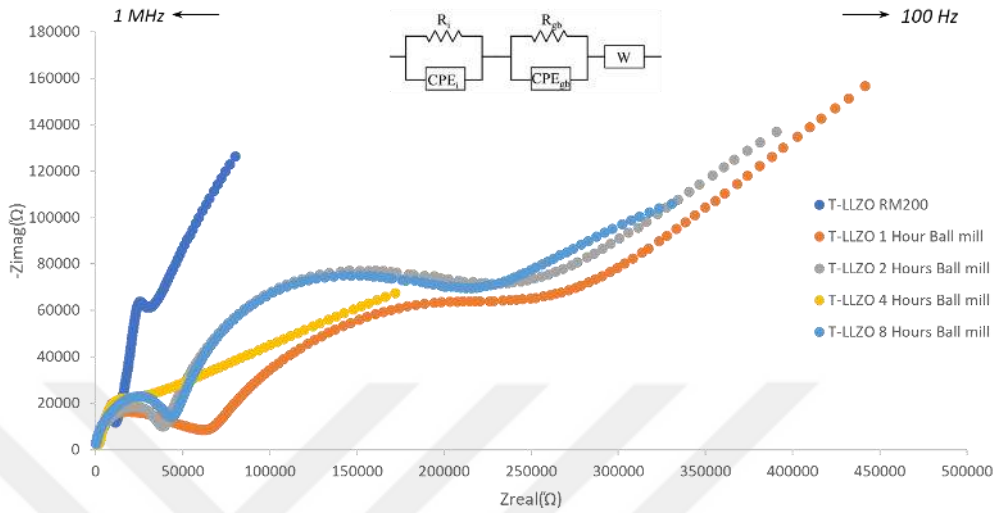

Figure 5.23. *Nyquist plots of T-LLZO samples obtained from powders milled at different times.*

The measured ionic conductivities of the samples obtained from the powders ground at different times are given in Figure 5.24. From the SEM images, it was seen that the effect of milling time on the reduction of grain size was limited. As a result, the increase in ionic conductivity was equally limited. Since the prepared samples do not have a dense structure, their ionic conductivity is also low. The ionic conductivity graph in Figure 5.24 shows that the ionic conductivity increases with the increase of the milling time. It was observed that the ionic conductivity increased until the sample milled for 4 hours, but the ionic conductivity decreased in the sample milled for 8 hours. In SEM images, it was observed that the amount of interconnected structures increased as the milling time increased. Based on the SEM images, it can be thought that the ionic conductivity will increase as the milling time increases, as structures with larger grains are obtained. However, in the XRD patterns of the samples obtained after sintering, it was determined that all samples had a cubic structure, except for the sample obtained from T-LLZO powder milled for 4 hours. The fact that the sample contains a tetragonal phase and has higher ionic conductivity than other samples illustrated an experimental or measurement error here.

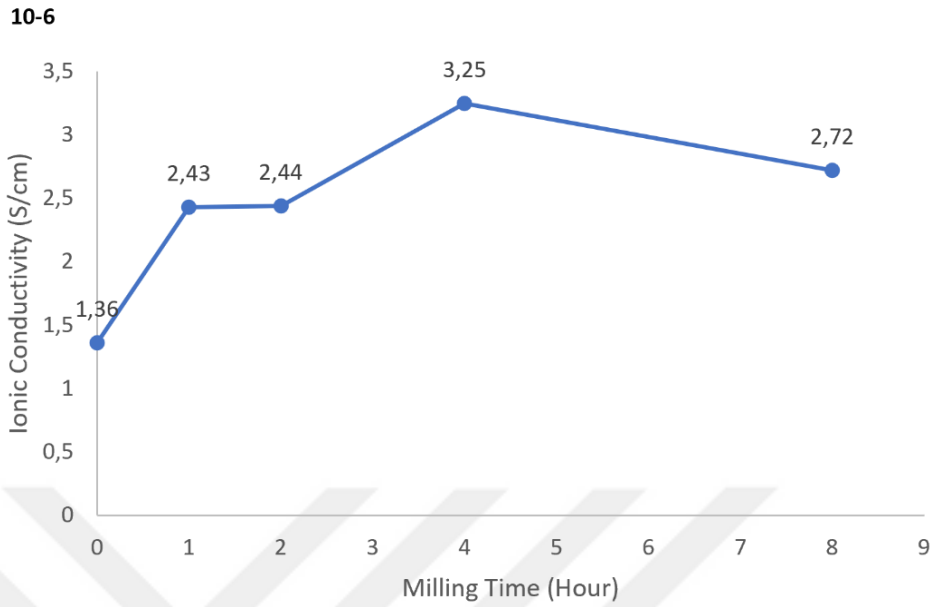

Figure 5.24. *Measured ionic conductivities of T-LLZO samples obtained from powders milled at different times.*

5.3 Effect of Milling Time on the Densification and Ionic Conductivity of T-LLZO containing RMD-LLZO Samples

In previous studies, the best microstructure and conductivity were obtained in 10% RMD-LLZO + 90% T-LLZO mixture. Therefore, in this study, the effect of milling time was investigated based on this mixture.

5.3.1 SE and BSE images

SE and BSE images of T-LLZO with RMD-LLZO addition milled for 2, 4 and 8 hours are given in Figure 5.25. In the images, it is seen that as the milling time increases, more grains bond with each other. While more unbonded spherical grains were observed in the sample milled for 2 hours, interlink formation was observed as the milling time increased. It was observed that in the sample milled for 2 hours, the fracture occurred at the grain boundaries while the fracture occurred at inside the grain in the samples milled for 4 and 8 hours. Especially, more interlink was observed in the sample milled for 8 hours. As the milling time increases, it is seen that more grains are combined as a result of sintering. However, a structure that worths to mill for 6 hours was not obtained.

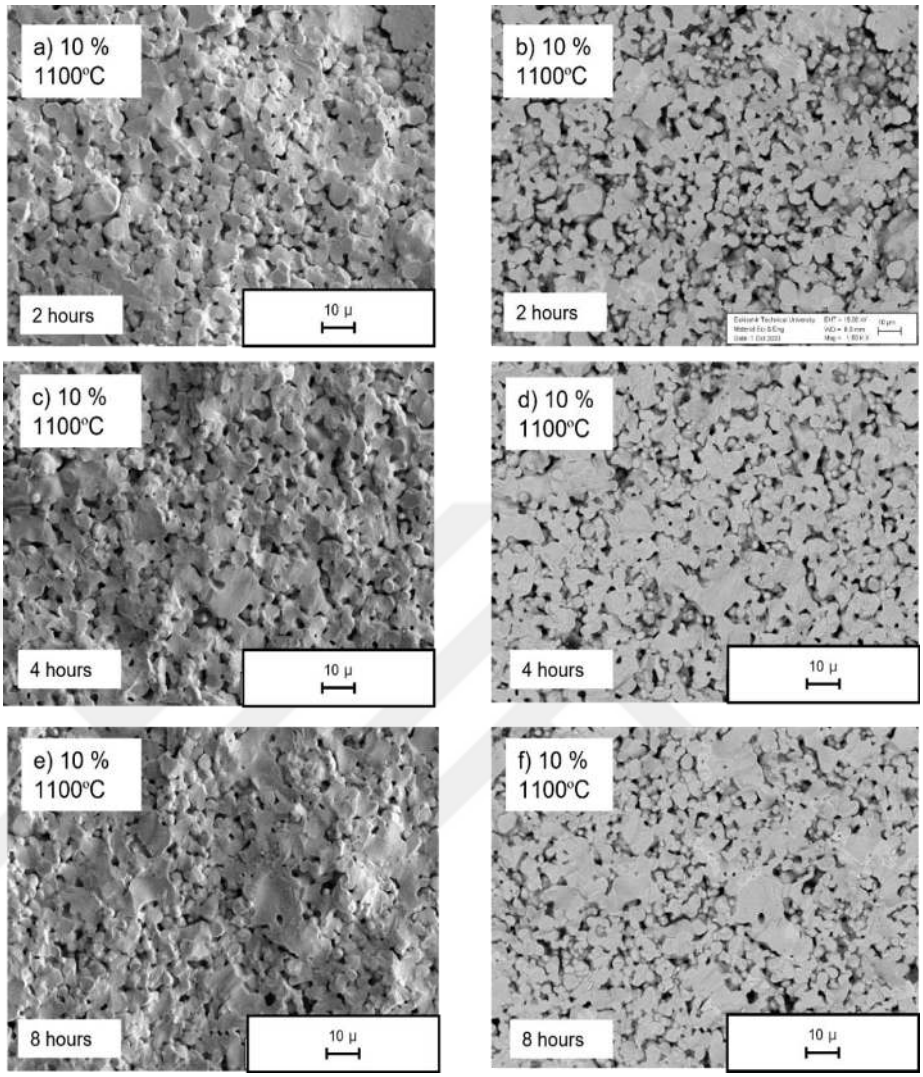

Figure 5.25. *SE and BSE images of T-LLZO samples with the addition of 10% RMD-LLZO milled for 2,4 and 8 hours. SE image of T-LLZO with 10% RMD-LLZO addition, milled for 2 hours (a), BSE image of T-LLZO with 10% RMD-LLZO addition, milled for 2 hours (b), SE image of T-LLZO with 10% RMD-LLZO additon, milled for 4 hours (c), BSE image of T-LLZO with 10% RMD-LLZO addition, milled for 4 hours (d), SE image of T-LLZO with 10% RMD-LLZO addition, milled for 8 hours (e), BSE image of T-LLZO with 10% RMD-LLZO addition, milled for 8 hours (f).*

5.3.2 Phase analysis

The phase analyzes of the samples after calcination are given in Figure 5.26. It is observed that all samples are in tetragonal structure.

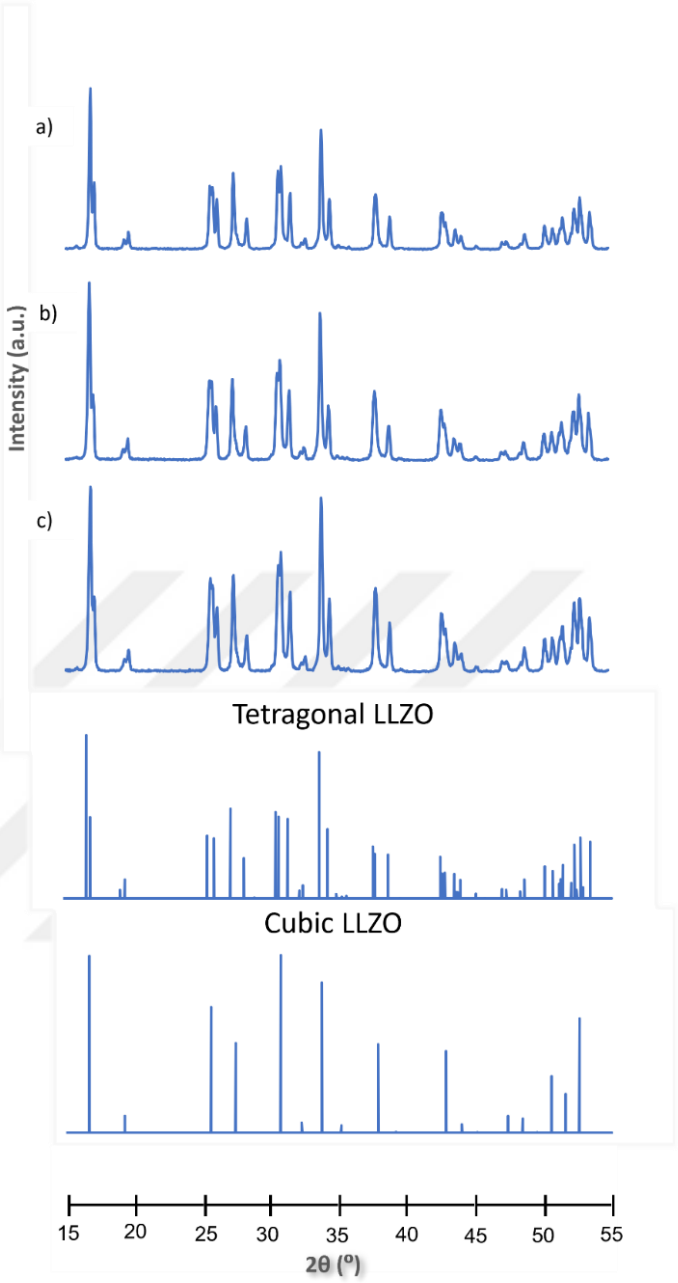

Figure 5.26. *Phase analysis of samples after calcination. T-LLZO with 10% RMD-LLZO addition, milled for 2 hours (a), T-LLZO with 10% RMD-LLZO addition, milled for 4 hours (b), T-LLZO with 10% RMD-LLZO addition, milled for 8 hours (c).*

The phase analyzes of the samples after sintering are given in Figure 5.27. It was observed that all samples were in cubic structure. By using cubic powder additive, the intended cubic structure in the final product was obtained.

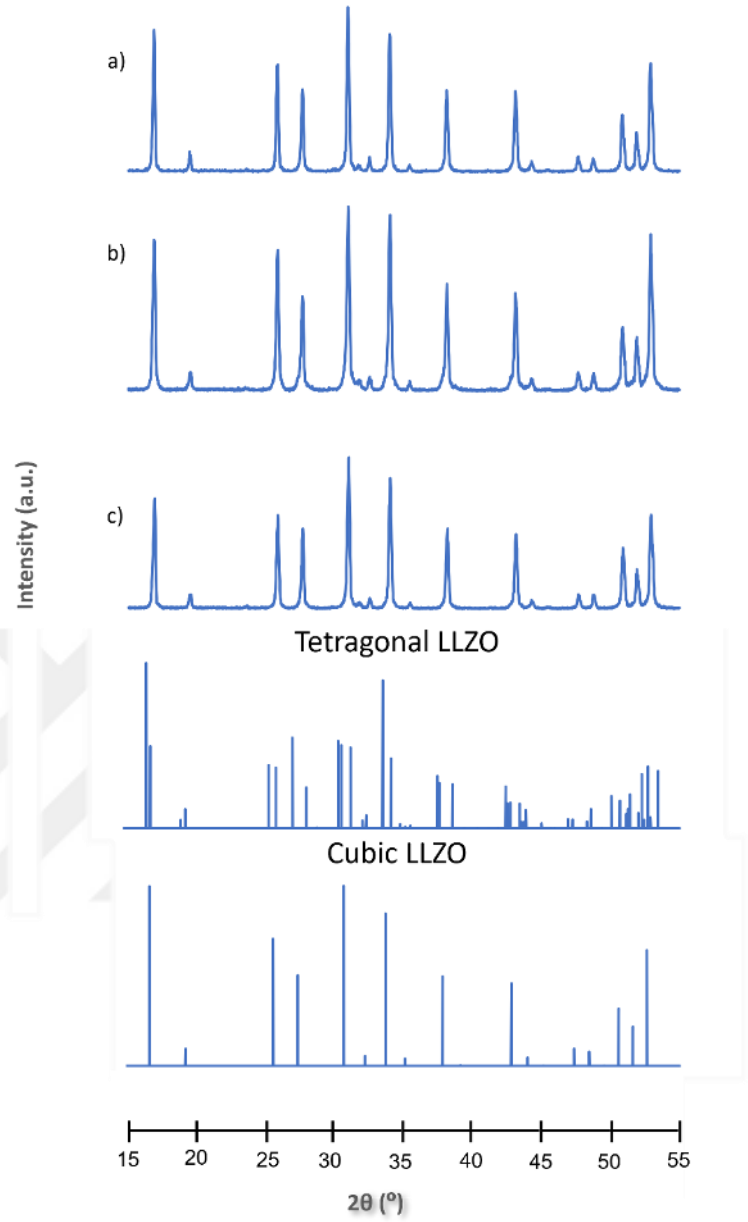

Figure 5.27. *Phase analysis of samples after sintering. T-LLZO with 10% RMD-LLZO addition, milled for 2 hours (a), T-LLZO with 10% RMD-LLZO addition, milled for 4 hours (b), T-LLZO with 10% RMD-LLZO addition, milled for 8 hours (c).*

5.3.3 Effect of milling time on ionic conductivity of T-LLZO with RMD-LLZO addition

Nyquist graphs of samples obtained from T-LLZO with RMD-LLZO addition powders milled at different times are given in Figure 5.28. Depending on the increase in milling time, the change of ionic conductivity values was observed. It has been observed that the diameter of the first semi-circle representing the bulk conductivity in the potentiostat graph decreases as the grain size of powders decreases. It was observed that the milling time increased the bulk conductivity. The second semicircle representing the grain boundary resistance is not clear, which shows that the grain boundary resistance is negligible.

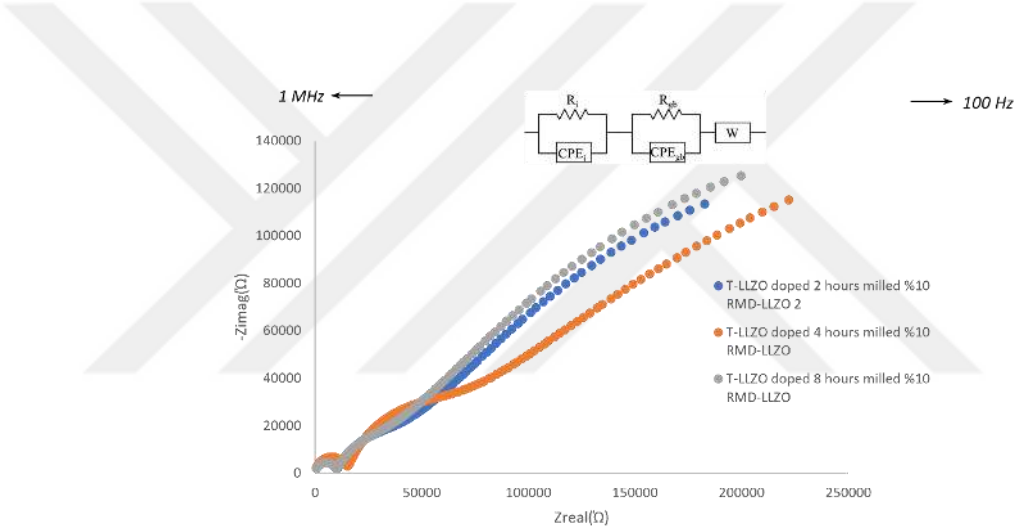

Figure 5.28. *Nyquist plots of T-LLZO with 10% RMD-LLZO addition obtained from powders milled at different times.*

Measured ionic conductivities of samples obtained from T-LLZO with 10% RMD-LLZO added powders milled at different times are given in Figure 5.29. The ionic conductivity increased as the milling time increased. However, an increase worth milling was not observed. Higher ionic conductivity values can be obtained without adding a ball mill to the process.

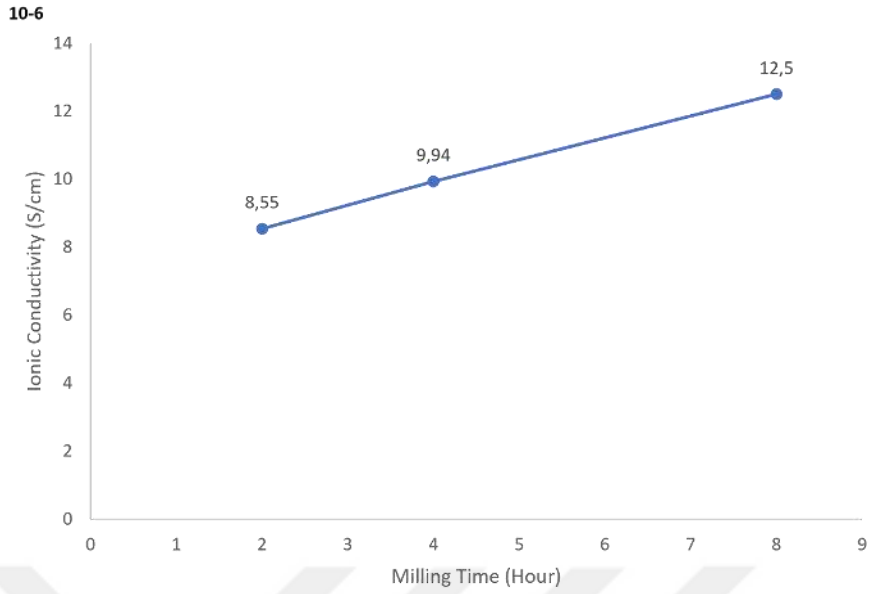

Figure 5.29. *Measured ionic conductivities of 10% RMD-LLZO added T-LLZO samples obtained from powders milled at different times.*

5.4 Investigation of the Effect of CIP Process Before Calcination and the Effect of Powder Bed Use During Sintering

During this study, the samples were divided into two groups. The mixture prepared in the first group was calcined in powder form, and the mixture prepared in the second group was calcined in pellet form. During the experiment, the effect of the compression process applied before the calcination process was investigated. In addition, powder bed and powder bedless samples were prepared to investigate the effect of powder bed use.

5.4.1 SE and BSE images

From the samples shown in Figure 5.30., it is seen that the calcined sample in powder form has a denser structure. It can be seen from the SEM images that sintering is partially inhibited when the calcination is done in pellet form.

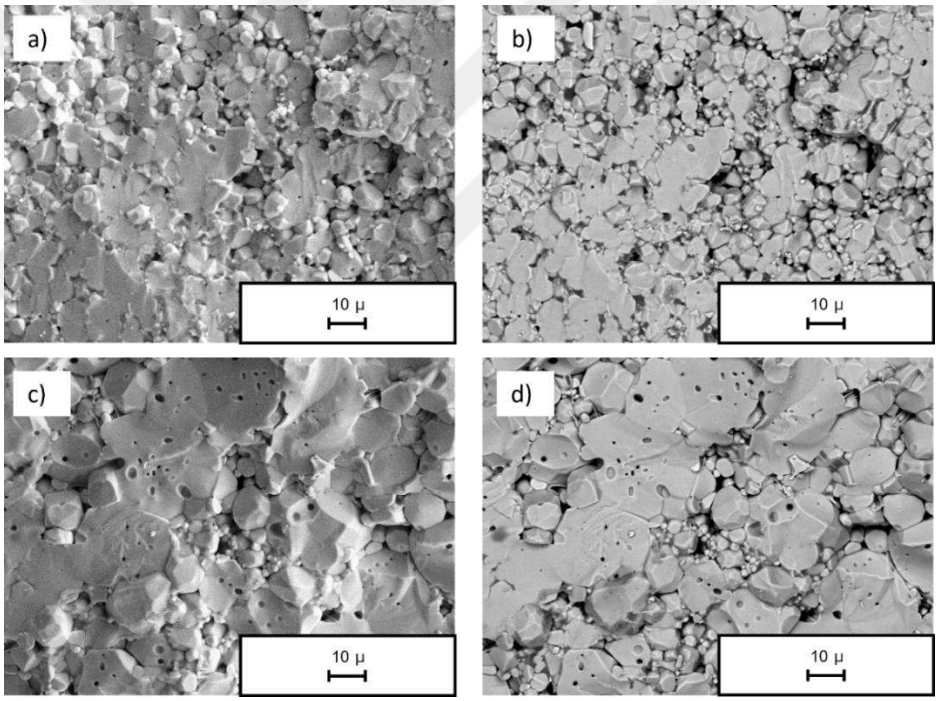

Figure 5.30. *SE and BSE images of T-LLZO with 10% RMD-LLZO addition samples obtained from the sample calcined in pellet and powder form. SE image of T-LLZO with 10% RMD-LLZO addition obtained from the sample calcined in pellet form. (a), BSE image of T-LLZO with 10% RMD-LLZO addition obtained from the sample calcined in pellet form. (b), SE image of T-LLZO with 10% RMD-LLZO addition obtained from the sample calcined in powder form. (c), BSE image of T-LLZO with 10% RMD-LLZO addition obtained from the sample calcined in powder form (d).*

It is seen that the SEM images of the mixtures calcined in pellet and powder form, shown in Figure 5.31. and Figure 5.16, are similar after sintering. Before the calcination process, the gases emerging in the decomposition reaction cannot be easily separated

from the system and remain between the particles in the sample, which is compressed in CIP with 300 MPa pressure and brought to pellet form. This affects sintering and inhibits sintering. This situation is not observed in the sample sintered after being calcined in powder form.

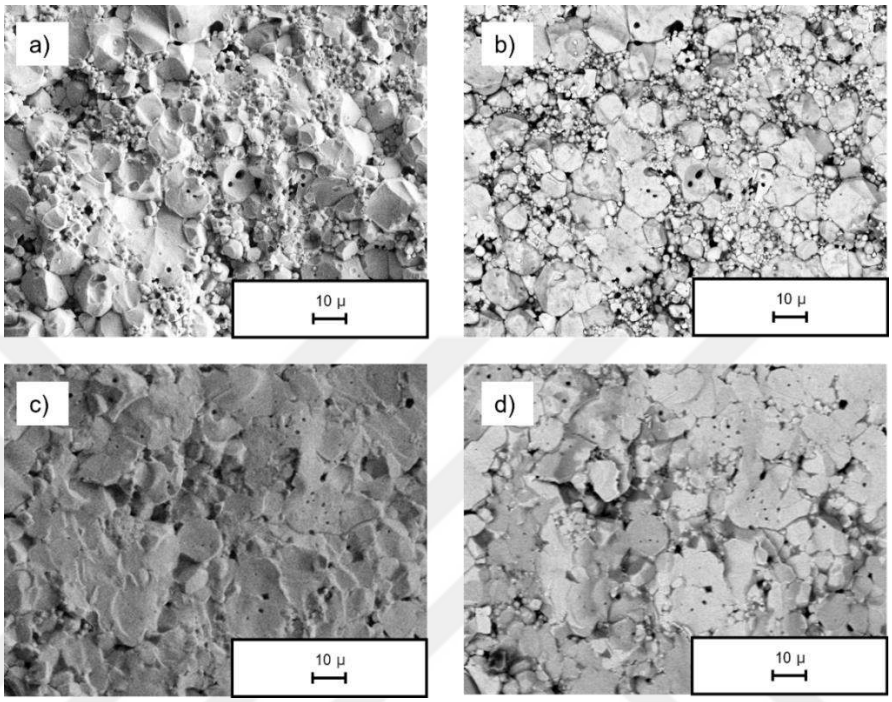

Figure 5.31 *SE and BSE images of 10% T-LLZO with RMD-LLZO addition samples obtained from the sample calcined in pellet and powder form. SE image of T-LLZO with 10% RMD-LLZO addition obtained from the sample calcined in pellet form. (a), BSE image of T-LLZO with 10% RMD-LLZO addition obtained from the sample calcined in pellet form. (b), SE image of T-LLZO with 10% RMD-LLZO addition obtained from the sample calcined in powder form. (c), BSE image of T-LLZO with 10% RMD-LLZO addition obtained from the sample calcined in powder form. (d). (While these samples were sintered, powder bed was not used.)*

5.4.2 Phase analysis

After calcination phase analysis of T-LLZO with 10% RMD-LLZO addition obtained from calcined samples in pellet and powder form is given in Figure 5.32. After

calcination, it is seen that both samples have a cubic structure. Impurity phases are not observed.

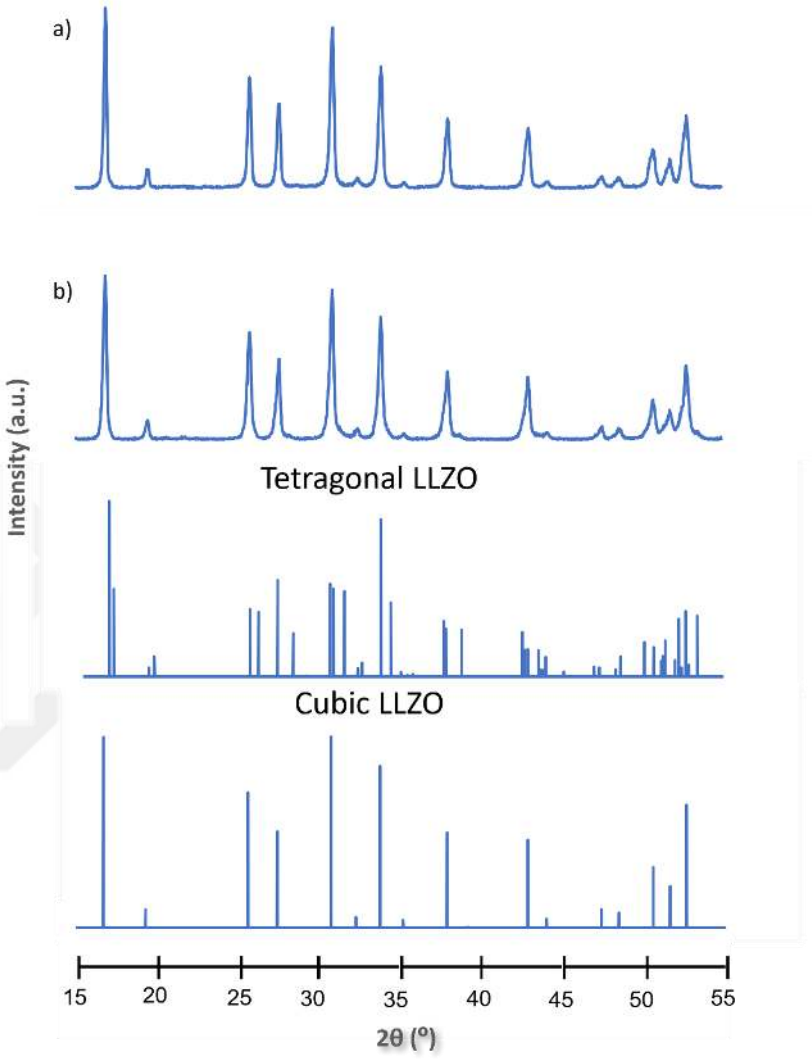

Figure 5.32. *After calcination phase analysis of calcined samples in pellet and powder form. After calcination phase analysis of the sample calcined in pellet form. (a), After calcination phase analysis of the sample calcined in powder form. (b).*

After sintering phase analysis of T-LLZO with 10% RMD-LLZO addition obtained from calcined samples in pellet and powder form is given in Figure 5.33. It was observed that both samples had a cubic structure after sintering. No impurity phase was observed.

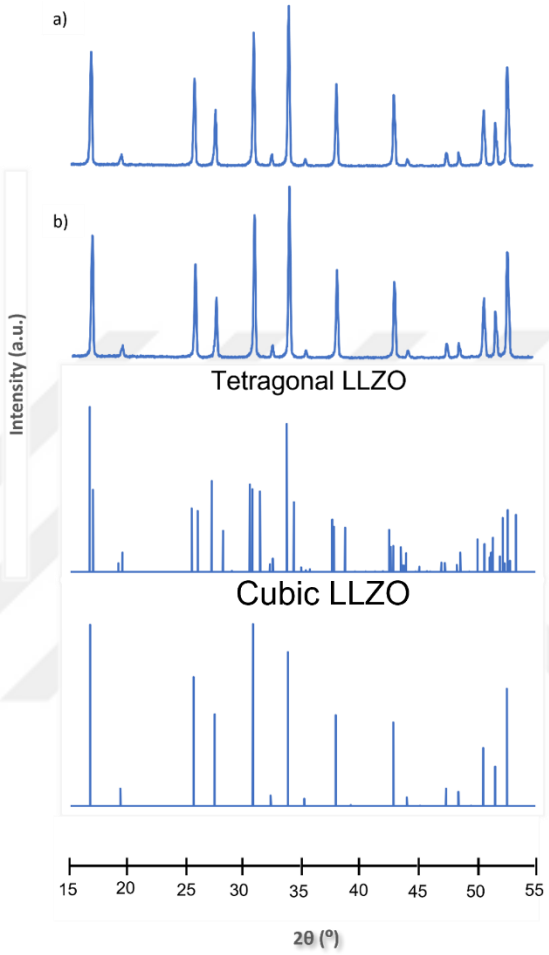

Figure 5.33. *After sintering phase analysis of calcined samples of pellet and powder form. After sintering phase analysis of the sample calcined in pellet form. (a), After sintering phase analysis of the sample calcined in powder form. (b).*

In Figure 5.34., post-calcination phase analysis of T-LLZO with 10% RMD-LLZO addition, calcined in pellet and powder form is given. It was determined that both samples had a cubic structure after calcination.

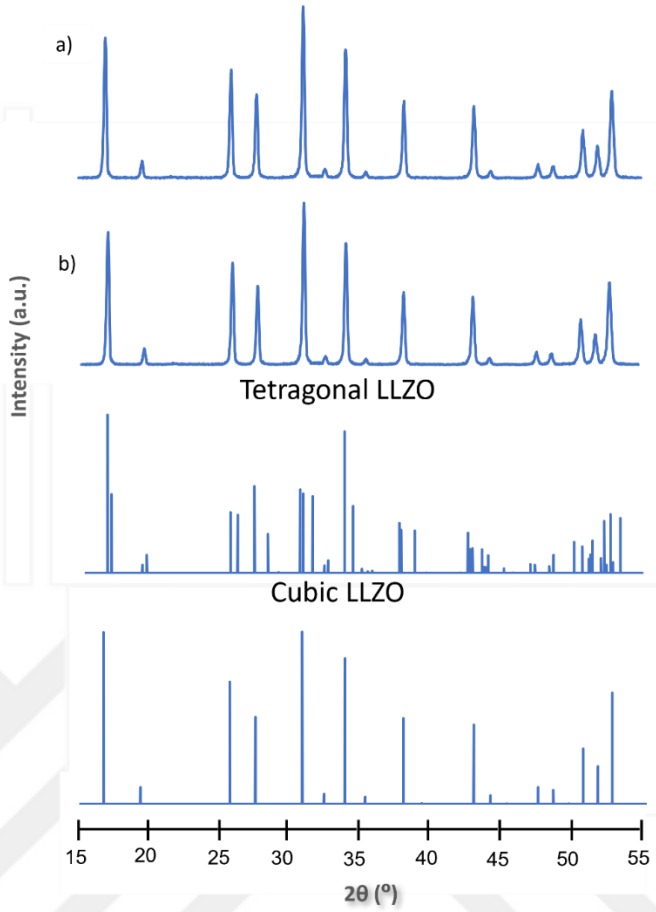

Figure 5.34. *After calcination phase analysis of calcined samples in pellet and powder form. After calcination phase analysis of the sample calcined in pellet form. (a), After calcination phase analysis of the sample calcined in powder form. (b).*

In Figure 5.35, post-sintering phase analysis of T-LLZO with 10% RMD-LLZO addition, calcined in pellet and powder form is given. These two samples were sintered without using powder bed. (a) $La_2Zr_2O_7$ was observed due to lithium loss in the sample calcined in pellet form.

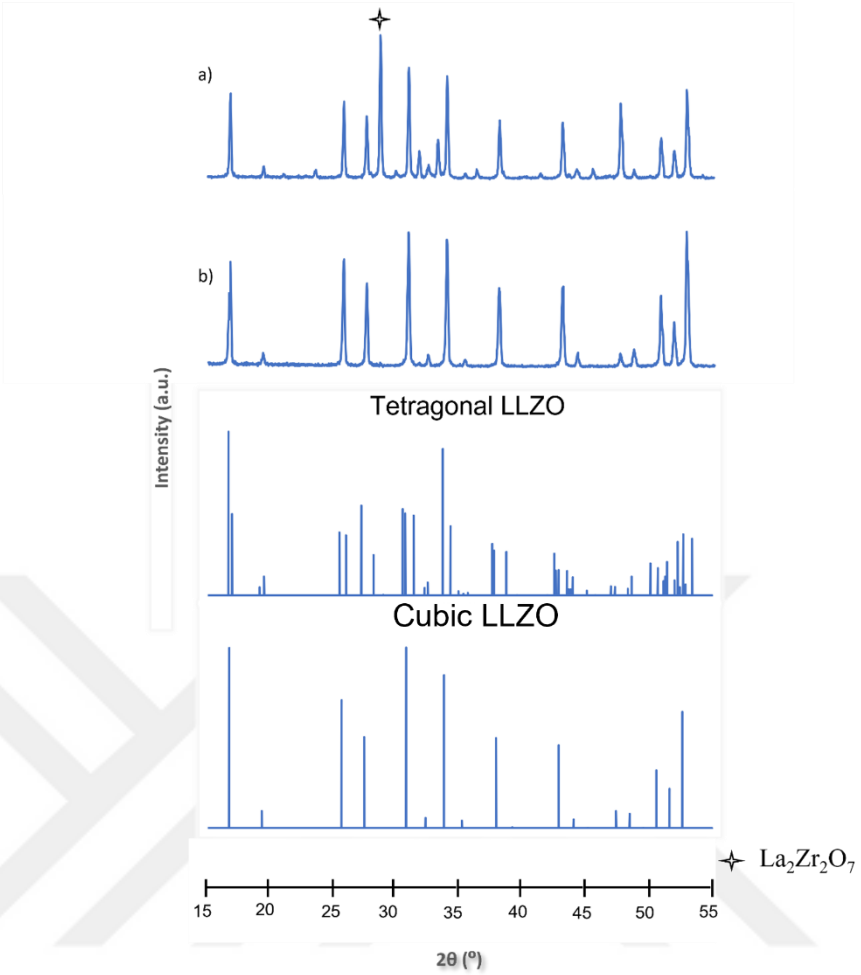

Figure 5.35. *After sintering phase analysis of calcined samples of pellet and powder form. After sintering phase analysis of the sample calcined in pellet form. (a), After sintering phase analysis of the sample calcined in powder form. (b). (While these samples were sintered, powder bed was not used.)*

5.4.3 Investigation of the effect of CIP process before calcination and the effect of powder bed usage during sintering on ionic conductivity

Nyquist plots of the samples, which were calcined in pellet form and powder form, and powder bed was used during sintering, are given in Figure 5.36.

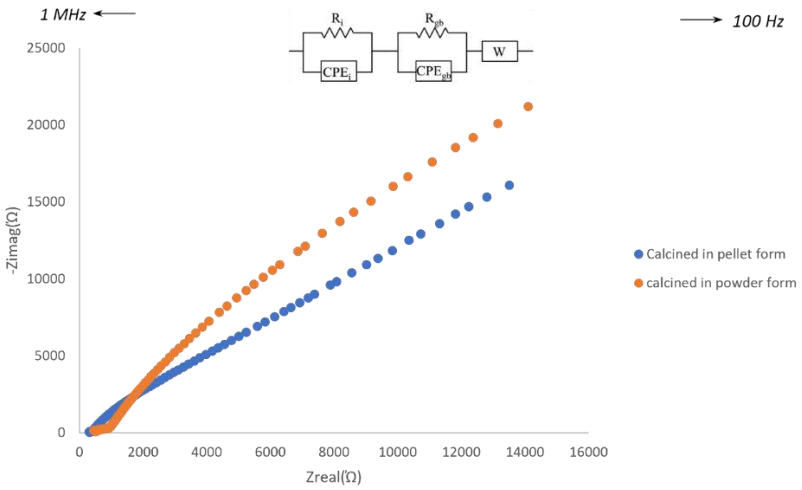

Figure 5.36. *Nyquist plots of T-LLZO with 10% RMD-LLZO addition calcined in pellet and powder form.*

Nyquist graphs of the samples calcined in pellet and powder form and powder bed unused during sintering are given in Figure 5.37.

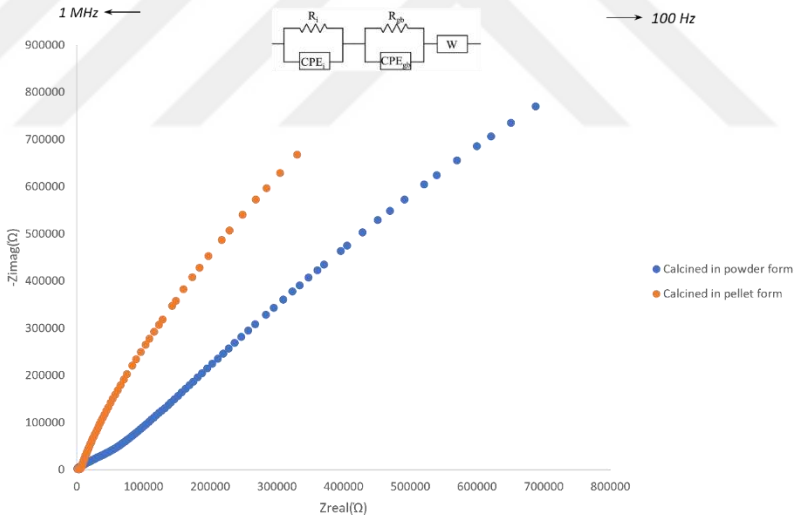

Figure 5.37. *Nyquist plots of T-LLZO with 10% RMD-LLZO addition calcined in pellet and powder form. samples calcined in pellet and powder form. (While these samples were sintered, powder bed was not used.)*

Calculated ionic conductivity values of the samples obtained after sintering of powders calcined in pellet and powder form are given in Figure 5.38. In the ionic conductivity values of 4 samples, it was determined that the samples calcined in powder

form had higher ionic conductivity. It has been determined that the use of powder bed during sintering provides higher ionic conductivity values.

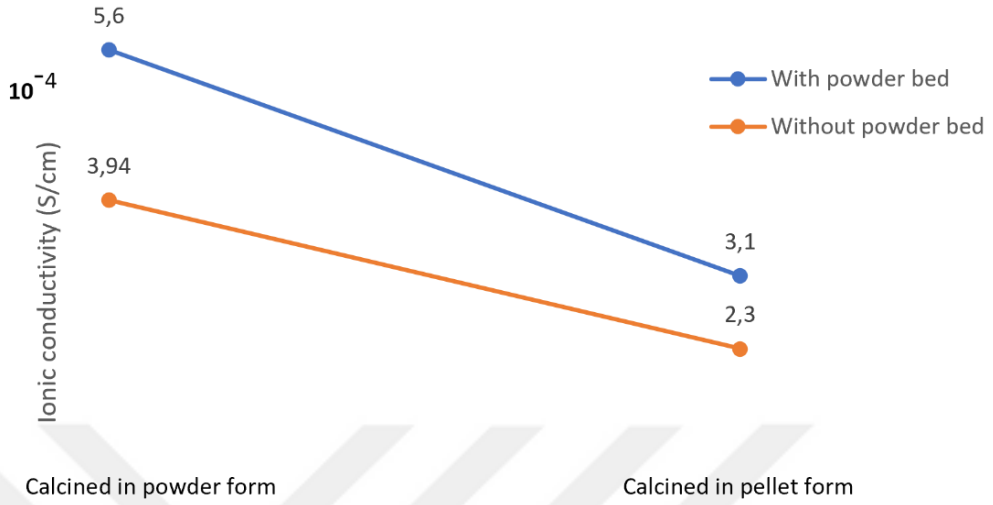

Figure 5.38. *Calculated ionic conductivities of T-LLZO with 10% RMD-LLZO addition calcined in pellet and powder form.*

5.5 Densification of LLZO Containing RMD-LLZO Powder without Calcination

5.5.1 SE and BSE images

The SE and BSE images in Figure 5.39 show that the sample contains many closed pores and has a cracked structure. Gaps in images are due to lithium loss. Lithium loss occurs very quickly from grain boundaries and triple intersection regions, not homogeneously inside the grain. Due to the gaps formed after the lithium loss, the grains are prevented from meeting and growing with each other. Although grain growth was observed in the images, closed pores were formed due to lithium loss and a dense structure could not be obtained.

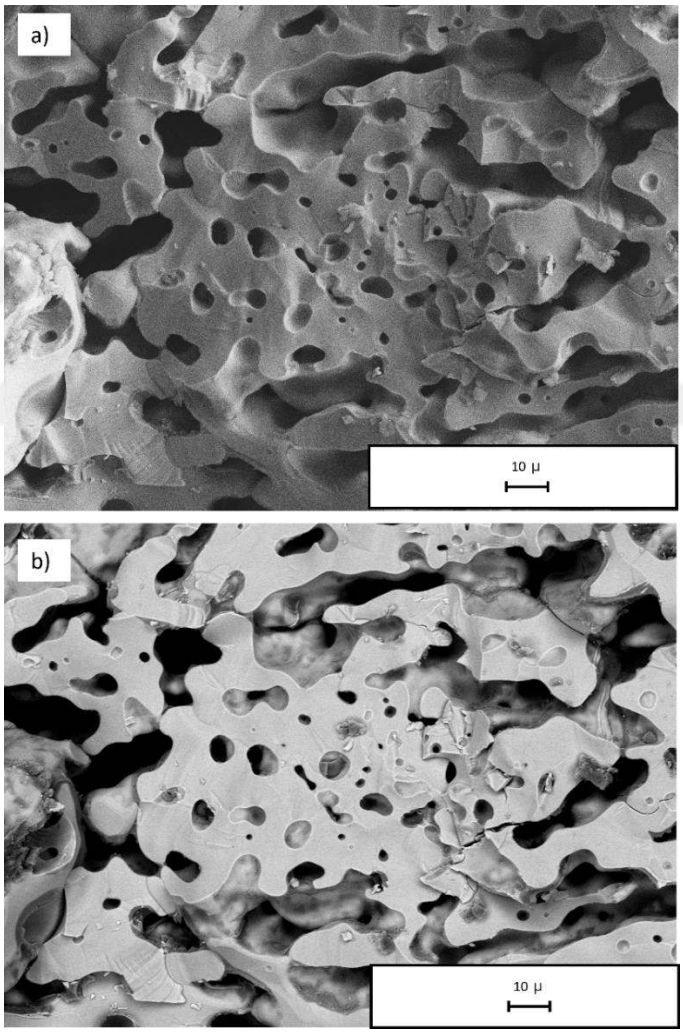

Figure 5.39. *SE and BSE images of 10% RMD-LLZO added T-LLZO samples, which are directly sintered without cooling after being calcined in pellet form. SE image (a), BSE image (b).*

5.5.2 Phase analysis

In Figure 5.40., the XRD pattern of the sample sintered without cooling after calcination is given. It was observed that the sample has a cubic LLZO structure.

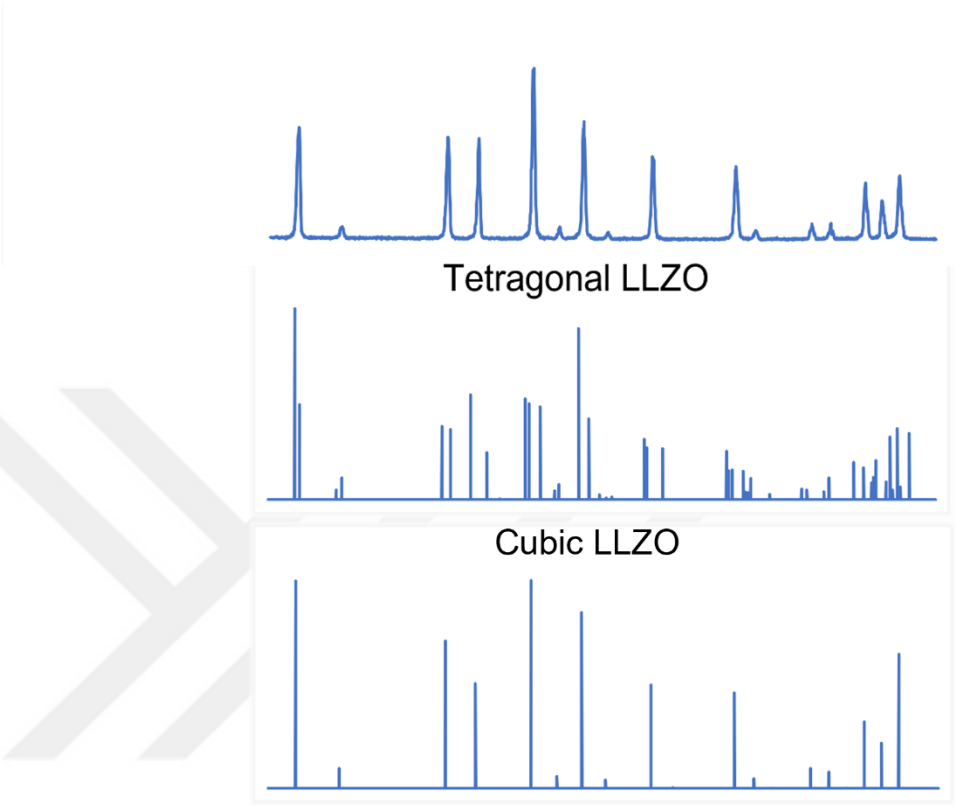

Figure 5.40. *XRD pattern of the sintered sample without cooling after calcination*

5.5.3 Effect of one-step densifiction on ionic conductivity

The nyquist plot of 10% RMD-LLZO added T-LLZO samples densificated in one step is given in Figure 5.41.

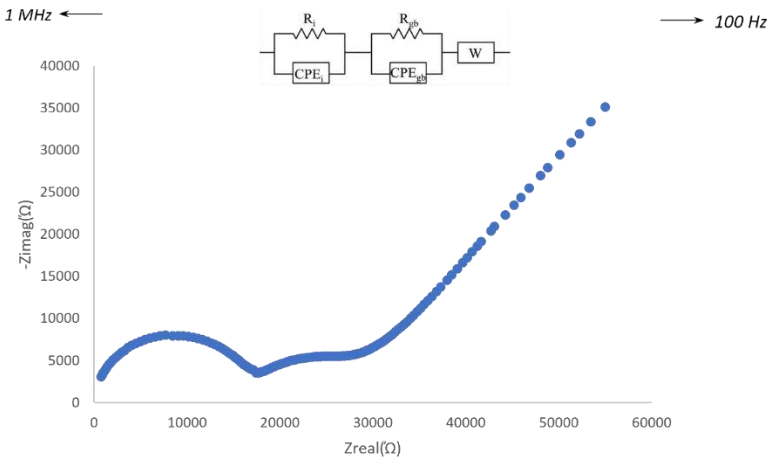

Figure 5.41. *Nyquist plot of 10% T-LLZO with RMD-LLZO addition.*

The calculated ionic conductivity value of the sample is 6.05×10^{-5} S/cm. In the microstructure images, it was observed that the sample was not dense and contained closed porosities. The ionic conductivity value was also low in this direction.

6. CONCLUSION AND FUTURE WORKS

Garnet type $Li_7La_3Zr_2O_{12}$ samples with cubic structure were produced by conventional solid state reaction. It is known that the porosity that occurs during production in all known solid electrolyte structures has negative effects on ionic conductivity. It is aimed to produce cubic LLZO with high density and low porosity after sintering.

In line with this goal, we showed that red mud, which is the waste material generated during aluminum production by the bayer process, can be used to convert $Li_7La_3Zr_2O_{12}$, which has tetragonal structure, to cubic structure and obtain a dense structure, thus obtaining a dense structure and high ionic conductivity (5.6×10^{-4} S/cm). In order to obtain a dense structure and high ionic conductivity, we conducted various studies based on parameters such as temperature, red mud doping, grain size, pre-compression and powder bed usage, and we investigated the results of these studies experimentally.

Since LLZO is polycrystalline, it shows grain/grain boundary microstructure and has high grain boundary resistance. In order to reduce the grain boundary resistance, we aimed to lower the sintering temperature by using additives that support sintering. We tried to obtain cubic LLZO at temperatures lower than 1230 ºC, which is the cubic phase transformation temperature of tetragonal LLZO. By adding 5,10,15% Red mud Doped LLZO (RMD-LLZO) by weight to Tetragonal LLZO (T-LLZO), we enabled it to support sintering and transform the sample into a cubic structure at 1100 ºC, 1150 ºC and 1200 ºC thanks to the core effect. We obtained the highest ionic conductivity value and the most dense microstructure in the T-LLZO with 10% RMD-LLZO addition sintered at 1100C. In subsequent studies, different applications were tried on the basis of 1100 ºC and 10% RMD-LLZO contribution. We found that the effect of doping becomes clearer as the T-LLZO moves away from the phase transformation temperature. We found that as the phase transformation temperature approaches, the containing additives LLZO turns into a multi-porosity microstructure originating from grain separation and its ionic conductivity is negatively affected because of this. The effects of milling and milling time were investigated from the data obtained after sintering of milled T-LLZO and T-LLZO with RMD-LLZO addition. It has been observed that it does not have sufficient effect on the production of a sample with a dense microstructure and high ionic conductivity.

Therefore, it has been found that adding the milling step to the process is not appropriate. The effect of the compression process applied before calcination was investigated. Accordingly, samples in the form of pellets and powders were prepared and calcined. It was observed that samples calcined in powder form had a denser microstructure and higher ionic conductivity than samples calcined in pellet form. In this situation, the gases that emerged during the calcination in the sample calcined in pellet form could not exit the system because they were in a compressed structure and it was seen that it affected the sintering afterwards. This situation was not encountered as the gases emerging during the calcination easily left the system in the calcined sample in powder form. When the same experiment was repeated without using a powder bed, similar microstructures emerged after sintering. However, the ionic conductivity of the samples sintered without using powder bed was lower. In addition, $La_2Zr_2O_7$ was detected due to lithium leakage in the phase analysis of the sample, which was calcined in pellet form and then sintered without using a powder bed. It is known that $La_2Zr_2O_7$ negatively affects the ionic conductivity, and the ionic conductivity of the sample was also lower than the other samples. One-step densification of T-LLZO with RMD-LLZO addition was investigated. As a result of sintering, a microstructure with a large number of porosities and cracked appearance emerged. Porosity and crack formation negatively affected the ionic conductivity. As a result of the experiments, it was determined that the sample with suitable grain growth and a dense structure and high ionic conductivity was the T-LLZO sample, which was calcined in powder form, sintered at 1100 ºC, powder bed was used during sintering and 10% RMD-LLZO added.

REFERENCES

[1] Mazman, M. and Yılmaz, C.H. (2019). *Energy storage solutions and general trends.* TMMOB Elektrik mühendisliği, 466, 32.

[2] Kozak, M. and Kozak, Ş. (2012). *Energy storage methods*. SDU International Technologic Science. 4 (2), 18-20.

[3] Aneke, M. and Wang, M. (2016). *Energy storage technologies and real life applications. Applied Energy*. 179, 350-377.

[4] Mahlia, T.M.I, Saktisahdan, T.J., Jannifar, A., Hasan, M.H. and Matseelar, H.S.C. (2014). *A review of available methods and development on energy storage; technology update.* Renewable and Sustainable Energy Reviews. 33, 532-545.

[5] Rohit, A.K., Devi, P. and Rangnekar, S. (2017). *An overview of energy storage and its importance in Indian renewable energy sector Part I – Technologies and Comparison*. Journal of Energy Storage. 13, 13-19.

[6] Zhou, Z., Benbouzid, M., Charpentier, J.F., Scuiller, F. and Tang, T. (2013). *A review of energy storage technologies for marine current energy systems*. Renewable and Sustainable Energy Reviews. 18, 390-400.

[7] Lund, H. and Salgi, G. (2009). *The role of compressed air energy storage (CAES) in future sustainable energy systems*. Energy Conversion and Management. 50 (2), 1172-1179.

[8] Yılmazoğlu, M. Z. (2010). *Isı Enerjisi Depolama Yöntemleri ve Binalarda Uygulanması*. Politeknik Dergi. 13(1), 33-42.

[9] Fernandez, A.I., Martinez, M., Segarra, M., Martorell, I. and Cabeza, L.F. (2010). *Selection of materials with potential in sensible thermal energy storage*. Solar Energy Materials and Solar Cells. 94(10), 1723-1729.

[10] Rismanchi, B., Saidur, R., BoroumandJazi, G. and Ahmed, S. (2012). *Energy, exergy and environmental analysis of cold thermal energy storage (CTES) systems*. Renewable and Sustainable Energy Reviews. 16 (8), 5741-5746.

[11] Kousksou, T., Bruel, P., Jamil, A., El Rhafiki, T. and Zeraouli, Y. (2014*). Energy storage: Applications and challenges*. Solar Energy Materials and Solar Cells. 120, 59-80.

[12] Suberu, M.Y., Mustafa, M.W. and Bashir, N. (2014). *Energy storage systems for renewable energy power sector integration and mitigation of intermittency*. Renewable and Sustainable Energy Reviews. 35, 499-514.

[13] Zhao, H., Wu, Q., Hu, H. and Rasmussen, C.N. (2015*). Review of energy storage system for wind power integration support*. Applied Energy. 137, 545-553.

[14] Nikolaidis, P. and Poullikkas, A. (2017). *A comparative review of electrical energy storage systems for better sustainability*. Journal of Power Technologies. 97(3), 220–245.

[15] https://en.globtek.com/nimh-battery-safety-notes/ (Date of Access : 25.05.2021)

[16] Rabiee, A., Khorramdel, H. and Aghaei, J. (2013). *A review of energy storage systems in microgrids with wind turbines.* Renewable and Sustainable Energy Reviews. 18, 316-326.

[17] Nguyen, T. and Savinell, R.F. (2010). *Flow Batteries*. Electrochemical Society Interface. 19, 54-56.

[18] Nielsen, K.E. and Molinas, M. (2010). Superconducting Magnetic Energy Storage (SMES) in Power Systems with Renewable Energy Sources. In Proceedings of the IEEE International Symposium on Industrial Electronics. 2487-2492.

[19] Rafik, F., Gualous, H., Gallay, R., Crausaz, A. and Berthon, A. (2007). Frequency, thermal and voltage supercapacitor characterization and modeling. Journal of Power Sources. 165(2), 928-934.

[20] Wakihara, M. (2001). Recent developments in lithium ion batteries. Materials Science and Engineering: R: Reports. 33(4), 109-134.

[21] Akkuş, N. (2011). *Şarj edilebilir lityum bataryalarda katot aktif madde olarak kullanılan LiMn2O4 bileşiğinin çoklu katyon katkılama ile döngü performansının iyileştirilmesi*. Master's Thesis. Kayseri: Erciyes University, Institute of Science.

[22] Tarascon, J. M. and Armand M. (2001). Issues and Challenges Facing Rechargeable Lithium Batteries. Nature. 414, 359-367.

[23] Mebarki, B., Draoui, B., Allaou, B., Rahmani, L. and Benachour, E. (2013). Impact of the Air-Conditioning System on the Power Consumption of an Electric Vehicle Powered by Lithium-Ion Battery. *Modelling and Simulation in Engineering*. 2013, 6 pages.

[24] Whittingham, M. S., Jacobson, A. J. (1982). *Intercalation Chemistry*, Academic Press. New York. p. 540.

[25] Yoshio, M., Brodd, R.J. and Kozawa, A. (2009). *Lithium-Ion Batteries:Science and Technologies*. Springer Science and Business Media. New York. pp. 1-7.

[26] Ozawa, K. (2009). Lithium Ion Rechargeable Batteries, Wiley-VCH Verlag GmbH, Weinheim, pp. 5-8.

[27] Nitta, N., Wu, F., Lee, J.T and Yushin. G. (2015). *Li-ion battery materials: present and future*. Today. 18(5), 252-264.

[28] Biçer, E., Mazman, M., Kaypmaz, C. and Uzun, D. (2020). Li-ion piller ve uygulamaları. Ankara: Nobel Akademik Yayıncılık.

[29] Ozawa, K. (2004). *Battery Seperators*. Chem. Rev. 104(10), 4419-4462.

[30] https://www.teijin.com/rd/technology/separator/ (Date of Access: 27.05.2021)

[31] XU, K. (2004). *Nonaqueous Liquid Electrolytes for Lithium-Based Rechargeable Batteries,* Chem. Rev. 104:4303-4417.

[32] Takuoshima, M.K. (2004). Development of Sulfur Batteries Development. Appl. Ceram. Technol. 76, 69–76.

[33] Kırkbınar, M. (2019). *Lityum hava bataryaları için lityum alüminyum titanyum fosfat esaslı cam seramik membranların geliştirilmesi*. Master's Thesis. Sakarya: Sakarya University, Institute of Science.

[34] Lu, Y., Li, L., Zhang, Q., Niu, Z. and Chen, J. (2018). *Electrolyte and interface engineering for solid-state sodium batteries*. Joule. 2(9), 1747-1770.

[35] Marom, R., Amalraj, S.F., Leifer, N., Jacob, D. and Aurbach, D. (2011*). A review of advanced and practical lithium battery materials*. J. Mater. Chem. 21(27), 9938- 9954.

[36] Zhang, Z., Zhang, Q., Ren, C., Luo, F., Ma, Q., Hu, Y.S., Zhou, Z., Li, H., Huang, X. and Chen, L. (2016). *A ceramic/polymer composite solid electrolyte for sodium batteries.* J. Mater. Chem. A. 4(41), 15823-15828.

[37] Doğan, M. (2019). *Katı hal enerji depolama cihazlarında fosfat esaslı ucuz çözüm yaklaşımları*. Master's Thesis. Sakarya: Sakarya University, Institute of Science.

[38] Kumar, D. and Hashmi, S.A. (2010). *Ionic liquid based sodium ion conducting gel polymer electrolytes*. Solid State Ionics. 181(8-10), 416-423.

[39] Dirican, M., Yan, C., Zhu, P. and Zhang, X. (2019). *Composite solid electrolytes for all-solid-state lithium batteries*. Materials Science & Engineering R: Reports. 136, 27–46.

[40] Zhang, Z., Xu, K., Rong, X., Hu, Y.S., Li, H., Huang, X. and Chen, L. (2017). *$Na_{3.4}Zr_{1.8}Mg_{0.2}Si_2PO_{12}$ filled poly(ethylene oxide)/Na(CF3SO2)2N as flexible composite polymer electrolyte for solid-state sodium batteries*. J. Power Sources. 372, 270-275.

[41] Zhang, B., Tan, R., Yang, L., Zheng, J., Zhang, K., Mo, S., Lin, Z. and Pan, F. (2018). *Mechanisms and properties of ion-transport in inorganic solid electrolytes.* Energy Storage Materials. 10, 139–159.

[42] Dermenci, K.B. (2018). *Development and characterızatıon of all solıd-state li-ion batteries.* PhD. Thesis. Eskişehir: Eskişehir Technical University, Graduate School of Sciences.

[43] Zheng, J., Li, Y., Yang, R., Li, G. and Ding, X. (2017). *Lithium ion conductivity in the solid electrolytes $(Li_{0.25}La_{0.25})_{1-x}M_{0.5x}NbO_3$ (M=Sr, Ba, Ca, x=0.125) with perovskite-type structure*. Ceramics International. 43, 1716–1721.

[44] Naqash, S., Gerhards, M.-T., Tietz, F., and Guillon, O. (2018). *Coefficients of Thermal Expansion of Al- and Y-Substituted NaSICON Solid Solution $Na_{3+2x}Al_xY_xZr_{2-2x}Si_2PO_{12}$*. Batteries. 4(3), 33.

[45] Kim, I.Y., Shin, S.Y., Ko, J.H., Lee, K.S., Woo, S.P., Kim, D.K. and Yoon, Y.S. (2017). *Functional Li-M (Ti, Al, Co, Ni, Mn, Fe)-O Energy Materials.* Journal of the Korean Ceramic Society. 54(1), 9-22.

[46] Rettenwander, D., Geiger, C.A., Tribus, M., Tropper, P., Wagner, R., Tippelt, G., Lottermoser, W. and Amthauer, G. (2015). *The solubility and site preference of Fe^{3+} in $Li_{7-3x}F_xLa_3Zr_2O_{12}$ garnets*. Journal of Solid State Chemistry. 230, 266-271.

[47] Kurzweil, P. (2015). *Post-lithium-ion battery chemistries for hybrid electric vehicles and battery electric vehicles*. Advances in Battery Technologies for Electric Vehicles. 7, 127-172.

[48] Reddy, M. V., Julien, C. M., Mauger, A. and Zaghib, K. (2020). *Sulfide and Oxide Inorganic Solid Electrolytes for All-Solid-State Li Batteries: A Review*. Nanomaterials, 10(8), 1606.

[49] Wang, Y., Song, S., Xu, C., Hu. N., Molenda, J. and Lu, L. (2019). *Development of solid-state electrolytes for sodium-ion battery–A short review*. Nano Materials Science. 1(2), 91-100.

[50] Kamaya, N., Homma, K., Yamakawa, Y., Hirayama, M., Kanno, R., Yonemura, M. Kamiyama, T., Kato, Y., Hama, S., Kawamoto, K. and Mitsui, A. (2011). *A lithium superionic conductor*. Nature Materials. 10, 682-686.

[51] Sakuda, A., Hayashi, A. and Tatsumisago, M. (2013). *Sulfide Solid Electrolyte with Favorable Mechanical Property for All-Solid-State Lithium Battery.* Scientific Reports 3, 2261

[52] Y. Kobayashi, T. Takeuchi, M. Tabuchi, K. Ado, and H. Kageyama. (1999). *Densification of $LiTi_2(PO_4)_3$-based solid electrolytes by spark-plasma-sintering*. Solid State Ionics. 309, 22–26.

[53] Murugan, R., Ramakumar, S. and Janani, N. (2011). *High conductive yttrium doped Li7La3Zr2O12 cubic lithium garnet*. Electrochemistry Communications. 13(12), 1373-1375.

[54] Mishra, M., Hsu, C., Rath, P.C., Patra, J., Lai, H., Chang, T., Wang, C., Wu, T., Lee, T. and Chang, J. (2020). *Ga-doped lithium lanthanum zirconium oxide electrolyte for solid-state Li batteries*. Electrochimica Acta. 353, 136536.

[55] Dermenci, K.B., Çekiç, E. and Turan, S. (2016). *Al stabilized $Li_7La_3Zr_2O_{12}$ solid electrolytes for all-solid state Li-ion batteries*. International Journal of Hydrogen Energy. 41(23), 9860-9867.

[56] Zhuang, L., Huang, X., Lu, Y., Tang, J., Zhou, Y., Ao, X., Yang, Y. and Tian, B. (2021). *Phase transformation and grain-boundary segregation in Al-Doped Li7La3Zr2O12 ceramics*. Ceramics International. 47, 22768-22775.

[57] Cao, Y., Li, Y.-Q., and Guo, X.-X. (2013). *Densification and lithium ion conductivity of garnet-type Li7−xLa3Zr2−xTaxO12(x= 0.25) solid electrolytes*. Chinese Physics B, 22(7), 078201.

[58] Dobretsov, E. A., Mateyshina, Y. G., and Uvarov, N. F. (2017). *Influence of lithium oxide excess and alumina on grain boundary resistance of Li6.75La3Zr1.75Nb0.25O12 solid electrolyte*. Solid State Ionics, 299, 55–59.

[59] Wagner, R., Redhammer, G., Rettenwander, D., Tippelt, G., Welzl, A., Taibl, S., Fleig, J., Franz, A., Lottermoser, W., and Amthauer, G. (2016). *Fast Li-Ion-Conducting Garnet-Related Li7–3xFexLa3Zr2O12 with Uncommon $I\bar{4}3d$ Structure*. Chemistry of Materials, 28, 5943- 5951.

[60] Wagner, R., Rettenwander, D., Redhammer, G., Tippelt, G., Sabathi, G., Musso, M., Stanje, B., Wilkening, M., Suard, E., and Amthauer, G. (2016). *Synthesis, Crystal Structure, and Stability of Cubic Li7–xLa3Zr2–xBixO12*. Inorganic Chemistry, 55, 12211- 12219.

[61] Miara, L. J., Richards, W. D., Wang, Y. E., and Ceder, G. (2015). *First-principles studies on cation dopants and electrolyte cathode ınterphases for lithium garnets*. Chemistry of Materials, 27(11), 4040–4047.

[62] Liu, W., Yang, Y. and Xiao, B. (2009*). Review on treatment and utilization of bauxite residues in China*. International Journal of Mineral Processing, vol. 93, 220 231.

[63] Dermenci, K.B. and Turan, S. (2020). *A novel densification model for sintering $Li_7La_3Zr_2O_{12}$-based solid electrolytes for all solid-state Li-ion batteries.* Ionics, 4757–4762.

[64] Buluç, A.F. (2019). *The effect of multi-element doping on cubic phase stabilization of $Li_7La_3Zr_2O_{12}$ by using waste material red mud.* Undergraduate thesis. Eskişehir: Eskişehir Technical University.

[65] Kaya, Ç. (2019). *Ga katkısının nano ölçekli $Li_{5-7}CaLa_2Zr_2O_{12}$ katı elektrolit malzemesinin performans değerlerine etkisinin elektrik, elektronik ve kristal özellikleri bakımından incelenmesi.* Master's Thesis. Mersin: Mersin University, Institute of Science.

[66] Chen, X., Cao, T., Xue, M., Lv, H., Li, B., and Zhang, C. (2018). *Improved room temperature ionic conductivity of Ta and Ca doped $Li_7La_3Zr_2 O_{12}$ via a modified solution method.* Solid State Ionics, 314, 92–97.

[67] Shao, C., Yu, Z., Liu, H., Zheng, Z., Sun, N., and Diao, C. (2017). *Enhanced ionic conductivity of titanium doped $Li_7La_3Zr_2O_{12}$ solid electrolyte.* Electrochimica Acta, 225, 345–349.

[68] Huang, M., Dumon, A., and Nan, C.-W. (2012). *Effect of Si, In and Ge doping on high ionic conductivity of $Li_7La_3Zr_2O_{12}$*. Electrochemistry Communications, 21, 62–64.